Incorporating Relativistic Effects in the Calculation of Core and Valence Excitations in Metal Complexes and Molecular Clusters

Joseph M. Kasper

A dissertation
submitted in partial fulfillment of the
requirements for the degree of

Doctor of Philosophy

University of Washington

2020

Reading Committee:

Xiaosong Li, Chair

Stefan Stoll

Daniel R. Gamelin

Program Authorized to Offer Degree:
Chemistry

University of Washington

Abstract

Incorporating Relativistic Effects in the Calculation of Core and Valence Excitations in Metal Complexes and Molecular Clusters

Joseph M. Kasper

Chair of the Supervisory Committee:
Professor Xiaosong Li
Department of Chemistry

Spectroscopy is one of the most powerful tools humanity has to probe the structure of matter. By seeing how light interacts with the atoms or molecules in a sample, intricate details of the quantum mechanical structure is revealed. Calculations of the quantum mechanical description of the electronic structure allows for both the prediction of observed phenomena, as well as an explanation of the physical processes underlying those observations. Although calculations that ignore corrections from special relativity are often sufficient, the inclusion of relativistic effects can be of great importance. Systems with heavy nuclei are especially well-known for strong corrections from relativity that are essential for even a qualitatively correct prediction. The work here focuses on including relativistic effects from first principles in electronic structure calculations to predict spectra of both core and valence excitations. In the first half, developments using the real-time approach of TDDFT with the X2C method are recounted, including the prediction of L-edge X-ray absorption spectra for transition metal complexes. The second half details developments using the frequency-based approach of TDDFT. This also entailed the development of new eigensolvers to more efficiently converge states in the high-energy region, as well as extensions of natural transition orbitals and visualization techniques for complex, two-component orbitals. Investigation of the Rashba effect in the valence excitations in ZnO semiconducting quantum dots conclude the work.

TABLE OF CONTENTS

LIST OF FIGURES

LIST OF TABLES

GLOSSARY

AO: atomic orbital

DFT: density functional theory

ECP: effective core potential

FWHM: full-width at half-maximum

GHF: generalized Hartree–Fock

GKS: generalized Kohn–Sham

GPLHR: generalized preconditioned locally harmonic residual

HF: Hartree–Fock

KS: Kohn–Sham

LCAO: linear combination of atomic orbitals

MMUT: modified midpoint unitary transformation

MO: molecular orbital

NO: natural orbital

NTO: natural transition orbital

SCF: self-consistent field

SOC: spin–orbit coupling

TDDFT: time-dependent density functional theory

RHF: restricted Hartree–Fock

RKS: restricted Kohn–Sham

RT-TDDFT: real-time time-dependent density functional theory

UHF: unrestricted Hartree–Fock

UKS: unrestricted Kohn–Sham

XAS: X-ray absorption spectroscopy

X2C: exact two-component

ACKNOWLEDGMENTS

Science, like life, is never done in a vacuum and I would not be able to have accomplished this work without the support of many people. I wish to thank Xiaosong Li, my advisor, for his guidance and direction in research. He seems to have an endless supply of enthusiam and is always full of new ideas to try and explore. His willingness to offer his time and speak candidly both when things were going well as well as not so well have contributed immensely to my growth as a scientist. The other members of my committee (Stefan Stoll, Daniel Gamelin, Munira Khalil, and Peter Pauzauskie) have also helped provide valuable insight with their wide-ranging expertise and experimental backgrounds to see problems beyond the theory perspective and ask questions I would not have otherwise considered.

In Xiaosong's research group I have made many friendships as well as good research colleagues. Joshua Goings, Franco Egidi, and David Williams-Young were fantastic to share an office with and help me figure out what I was doing during my first year. Patrick Lestrange, David Lingerfelt, Alessio Petrone, and Hongbin Liu were also greatly encouraging and good to talk to when projects seemed to hit a wall. Many other current members continue to supply plenty of laughter and good conversation, including Torin Stetina, Andrew Wildman, Ryan Beck, Andrew Jenkins, Andrew Valentine, Lauren Koulias, and Chad Hoyer.

I also want to thank Ping Yang and Enrique Batista for allowing me the opportunity to work at Los Alamos for a quarter this past winter. Your kindness and scientific insight made the time there so enjoyable and I look forward to working together in the future.

To my many friends outside my academic work, I also could not have made it through without your support and love, especially those who put up with me as an apartment mate: Kiffin, Junil, Jacob, and David.

To my family, I cannot even begin to thank you enough for the many ways you've supported me my entire life to get me to this point.

DEDICATION

to my grandparents, I know you would be proud

PREFACE

In writing one inevitably has to choose what to include and what to leave out. Most of the work here assumes a working knowledge of quantum mechanics and matrix algebra. Chapter 1 provides an overview to basic electronic structure theory, with particular attention to two-component methods and a treatment of spin. The subsequent chapters detail development and applications of new methods to include relativistic effects and calculate spectra.

Chapter 2 describes work on the development and implementation of a real-time X2C method. The software implementation of X2C in Gaussian [5] was mostly complete when I joined the group and only minor changes were needed to make sure the different parts of the code interfaced properly. Although not used for the calculations in this paper, I added X2C to the ChronusQuantum [6] package so that the same functionality is available there. Additionally, the data were processed using the recently reported Padé transformation instead of a standard Fourier transformation, which allowed the required time propagation to be reduced.

The work in Chapter 3 uses the same code from the previous work to calculate core excitations at the L-edge for seveal metal complexes. I also made additional modifications to the real-time code in Gaussian that allowed for separation of the time-evolving density matrix into orbital pairs for parsing. This has the advantage that the contribution of particular orbitals to the intensity can be resolved and allow an interpretation similar to what would be obtained in a linear-response (TDDFT) calculation. Due to the short time-steps required for X-ray calculations, the use of Padé transformations to reduce the need for long time simulations was also critical.

Chapter 4 describes work on a new hybrid eigensolver that combines the Davidson and

newly introduced generalized preconditioned locally harmonic residual (GPLHR) methods for iterative diagonalization in the interior of the eigenspectrum. For molecular systems with a large number of nearly degenerate states (such as in nanocrystals) the convergence of the excitations in the X-ray region can be very slow using only a Davidson-type eigensolver. By contrast, the GPLHR method is robust in convergence, but can be expensive. By implementing the GPLHR method in Gaussian and allowing on-the-fly switching with the standard Davidson approach, improved computational behavior was observed.

In Chapter 5, small extensions of code in Gaussian allowed for the calculation of natural transition orbitals (NTOs) in two-component calculations. The explicit inclusion of spin in the orbitals also necessitates additional functionality to visualize them. Mapped isosurfaces as well as the spinor magnetization density show the transition between collinear orbitals and non-collinear orbitals when spin-orbit coupling is included.

Chapter 6 details the application of X2C-TDDFT to calculate the fine structure of the excition manifold in ZnO quantum dots of varying sizes. By analyzing the exciton structure, the impact of quantum confinement on the Rashba effect is observed. In particular, the "upper" and "lower" excitons can mix and even overlap in small, highly-confined quantum dots. The *ab initio* approach will also allow future studies of the influence of dopants, surface ligands, or other defects of interest.

Finally, additional discussion of the Dirac equation and the X2C transformation are given in the appendix.

Chapter 1

INTRODUCTION AND PRELIMINARIES

The goal of electronic structure theory is to describe the electrons in a system (such as a molecule) in an accurate way for making predictions of observed properties. Quantum mechanics postulates that this can be done by using appropriate mathematical functions and operators to represent the system of interest. The wavefunction Ψ describes the state of the system, and in general is a function of the coordinates of all the particles in the system. Since the nuclei are much heavier than electrons, their motion is often much slower and it is possible to treat them as fixed. This is the commonly-invoked Born–Oppenheimer approximation, in which the electronic and nuclear degrees of freedom are separated. That is, the total wavefunction is separated so that

$$\Psi(\vec{r_i}, \vec{R_j}) = \Psi_{elec}(\vec{r_i}; \vec{R_j})\Psi_{nuc}(\vec{R_j}) \tag{1.1}$$

where $\vec{r_i}$ and $\vec{R_j}$ are the electronic and nuclear coordinates. In particular, the electronic wavefunction is assumed to depend only *parametrically* on the nuclear coordinates. The electronic wavefunction is then governed by either the non-relativistic time-independent Schrödinger equation or the relativistic Dirac equation and can be written in the form

$$\hat{H}\Psi_{elec} = E\Psi_{elec} \tag{1.2}$$

where $\hat{H}$ is the appropriate Hamiltonian and E is the energy. As the nuclear wavefunction Ψ_{nuc} will not be discussed further, Ψ will be assumed to be the electronic wavefunction.

The Hamiltonian for the non-relativistic Schrödinger equation for N electrons in an M-

nuclei system is

$$\hat{H} = -\frac{1}{2}\sum_{i=1}^{N} \nabla_i^2 - \sum_{i=1}^{N}\sum_{A=1}^{M} \frac{Z_A}{r_{iA}} + \sum_{i=1}^{N-1}\sum_{j>i}^{N} \frac{1}{r_{ij}} + \sum_{A=1}^{M-1}\sum_{B>A}^{M} \frac{Z_A Z_B}{r_{AB}} \tag{1.3}$$

Within the context of the Born–Oppenheimer approximation the last term, nuclear-nuclear repulsion, is constant. The first two terms are often grouped together and known as the *core* Hamiltonian, while the third is the electron–electron repulsion. Although there are relativistic corrections to the electron-electron repulsion, the most common corrections concern the core Hamiltonian. These corrections from the Dirac equation will be discussed later.

For one-electron systems Eq. (1.2) is fairly easily solved and has a closed-form solution for both the Schrödinger and Dirac equations. For many-electron systems, the electron-electron repulsion term prevents this and so the wavefunction Ψ is often expanded in a basis. While it is possible to represent any Ψ with a complete, infinite basis, a finite basis is limited such that exact solution of Eq. (1.2) in that basis may not. The error associated with using an incomplete basis is known as basis set error. The following section outlines the basics of Hartree–Fock theory, while more detailed information can be found in classic references such as Szabo and Ostlund [7].

1.1 Basis Sets and Hartree–Fock Theory

Many different basis functions can be used; however, the most common basis functions to use are atomic orbitals (AOs). These functions are centered on the nuclei of the molecule and are a natural choice since they describe the regions where electrons are likely to be. Within a given basis, how does one construct an appropriate wavefunction? Since electrons are fermions, any valid wavefunction must be antisymmetric to exchange. That is,

$$\Psi(x_1, x_2, ..., x_N) = -\Psi(x_2, x_1, ..., x_N) \tag{1.4}$$

This requirement, also known as the Pauli exclusion principle, implies that the wavefunction vanishes if $x_1 = x_2$. Equivalently, two or more electrons cannot occupy the same quantum

state. To ensure that this requirement is fulfilled, a form of wavefunction known as the Slater determinant is commonly used. The Slater determinant is an antisymmetrized product of single-electron wavefunctions (or orbitals):

$$\Psi = \frac{1}{\sqrt{N!}} \begin{vmatrix} \psi_1(x_1) & \psi_2(x_1) & \cdots & \psi_N(x_1) \\ \psi_1(x_2) & \psi_2(x_2) & \cdots & \psi_N(x_2) \\ \vdots & \vdots & \ddots & \vdots \\ \psi_1(x_N) & \psi_2(x_N) & \cdots & \psi_N(x_N) \end{vmatrix} \tag{1.5}$$

These molecular orbitals (MOs) are formed from the basis functions using the linear combination of atomic orbitals (LCAO) ansatz:

$$\psi_i = \sum_j c_{ij} \chi_j \tag{1.6}$$

In Hartree-Fock theory, the orbitals are optimized according to the variational principle. That is, since any trial wavefunction $\tilde{\Psi}$ has an energy that is greater than or equal to that of the true ground state wavefunction Ψ, a good approximation to the ground state can be obtained by minimizing the energy. In particular, the variation of the Lagrangian is set to zero:

$$0 = \mathcal{L} = \langle \Psi | \hat{H} | \Psi \rangle - \sum_{ij} \epsilon_{ij} (\langle \psi_i | \psi_j \rangle - \delta_{ij}) \tag{1.7}$$

This reduces to solving the generalized eigenvalue problem:

$$\boldsymbol{FC} = \boldsymbol{SC\epsilon} \tag{1.8}$$

where $\boldsymbol{F}$ is the Fock matrix, $\boldsymbol{C}$ are the MO coefficients, and $\boldsymbol{S}$ is the overlap matrix of basis functions ($S_{\mu\nu} = \langle \mu | \nu \rangle$). The Fock operator is the effective Hamiltonian for each of the one particle wavefunctions:

$$\hat{f}(x_i)\psi_i(x_i) = \epsilon_i \psi_i(x_i) \tag{1.9}$$

In relation to the Hamiltonian, the Fock operator is a sum of the core-Hamiltonian and the effective one-electron potential that corresponds to the average (mean-field) effect of the other electrons.

Alhtough originally derived for closed-shell molecules in restricted Hartree–Fock (RHF), generalized Hartree–Fock (GHF) theory puts no constraints on spin. Instead each orbital is expressed as a two-component spinor

$$\psi_k(\boldsymbol{x}) = \begin{pmatrix} \phi_k^{\alpha}(\boldsymbol{r}) \\ \phi_k^{\beta}(\boldsymbol{r}) \end{pmatrix} \tag{1.10}$$

The functions $\{\phi_k^{\alpha}(\boldsymbol{r})\}$ and $\{\phi_k^{\beta}(\boldsymbol{r})\}$ are expanded in the same set of AO basis functions $\{\chi_\mu(\boldsymbol{r})\}$:

$$\phi_k^{\alpha}(\boldsymbol{r}) = \sum_{\mu} C_{\mu k}^{\alpha} \chi_{mu}(\boldsymbol{r}) \tag{1.11}$$

$$\phi_k^{\beta}(\boldsymbol{r}) = \sum_{\mu} C_{\mu k}^{\beta} \chi_{mu}(\boldsymbol{r}) \tag{1.12}$$

Using this spin-blocked structure, the Fock matrix has the form

$$\boldsymbol{F} = \begin{pmatrix} \boldsymbol{F}^{\alpha\alpha} & \boldsymbol{F}^{\alpha\beta} \\ \boldsymbol{F}^{\beta\alpha} & \boldsymbol{F}^{\beta\beta} \end{pmatrix} \tag{1.13}$$

The blocks $\boldsymbol{F}^{\sigma\tau}$ are given by

$$\boldsymbol{F}^{\sigma\tau} = \boldsymbol{h}^{\sigma\tau} + \delta_{\sigma\tau}\left[\boldsymbol{J}^{\alpha\alpha} + \boldsymbol{J}^{\beta\beta}\right] - \boldsymbol{K}^{\sigma\tau} \tag{1.14}$$

where $\boldsymbol{h}^{\sigma\tau}$ is the core-Hamiltonian matrix, $\boldsymbol{J}^{\sigma\tau}$ is the Coulomb matrix, and $\boldsymbol{K}^{\sigma\tau}$ is the exchange matrix.

The Coulomb and exchange matrices are readily calculated from the AO basis functions as

$$J_{\mu\nu}^{\sigma\sigma} = \langle\mu|\,\hat{J}^{\sigma\sigma}\,|\nu\rangle = \sum_{i=1}^{N}\sum_{\lambda\kappa} C_{\lambda i}^{\sigma} C_{\kappa i}^{\sigma *} \int d\boldsymbol{r}_1 d\boldsymbol{r}_2 \chi_\mu^*(\boldsymbol{r}_1)\chi_\kappa^*(\boldsymbol{r}_2)\frac{1}{r_{12}}\chi_\lambda(\boldsymbol{r}_2)\chi_\nu(\boldsymbol{r}_1) \tag{1.15}$$

$$K_{\mu\nu}^{\sigma\tau} = \langle\mu|\,\hat{K}^{\sigma\tau}\,|\nu\rangle = \sum_{i=1}^{N}\sum_{\lambda\kappa} C_{\lambda i}^{\sigma} C_{\kappa i}^{\tau *} \int d\boldsymbol{r}_1 d\boldsymbol{r}_2 \chi_\mu^*(\boldsymbol{r}_1)\chi_\kappa^*(\boldsymbol{r}_2)\frac{1}{r_{12}}\chi_\nu(\boldsymbol{r}_2)\chi_\lambda(\boldsymbol{r}_1) \tag{1.16}$$

The first term is known as the one-particle density operator:

$$P_{\lambda\kappa}^{\sigma\tau} = \sum_{i=1}^{N}\sum_{\lambda\kappa} C_{\lambda i}^{\sigma} C_{\kappa i}^{\tau *} \tag{1.17}$$

It too can be wrriten with the same spin-blocked structure as the Fock matrix.

$$\boldsymbol{P} = \begin{pmatrix} \boldsymbol{P}^{\alpha\alpha} & \boldsymbol{P}^{\alpha\beta} \\ \boldsymbol{P}^{\beta\alpha} & \boldsymbol{P}^{\beta\beta} \end{pmatrix} \tag{1.18}$$

Due to the non-linear nature of the differential equations and the need to calculate the mean-field potential, the solution to the Hatree–Fock eigenvalue equation must be done iteratively until the Fock matrix generated by the current orbitals yields the same orbitals when diagonalized. This procedure is known as the self-consistent field (SCF) method.

1.2 Density Functional Theory

Unfortunately, the independent-particle ansatz of the single Slater determinant neglects significant contributions to the wavefunction and energy due to correlation between electrons. While there are many wavefunction-based approaches to treat correlation, they are often plagued by high computational scaling with the number of electrons N and so are not currently practical for systems with large numbers of electrons. Instead, an alternative approach to treat the missing correlation energy is through the use of density functional theory (DFT). DFT rests upon the proofs of Hohenberg and Kohn that the energy of the ground state is completely determined by the electron density [8]. In theory, it is able to provide an exact solution for significantly less computational cost. However, since the form of the true density functional is unknown, only approximations to the functional can be used.

The most common form of density functional theory is known as Kohn–Sham DFT. Although it is possible to formulate DFT without orbitals, in KS DFT the density is still determined by orbitals from a single Slater determinant. The energy expression, however, now includes an exchange-correlation term, which attempts to account for the errors:

$$E_{DFT}\left[\rho\right] = h\left[\rho\right] + J\left[\rho\right] + E_{xc}\left[\rho\right] \tag{1.19}$$

The core Hamiltonian h and Coulomb J contributions are the same as before in HF theory. However, the exchange term (which is a type of correlation) is replaced by the functional

E_{xc} to account for all the electron correlation and exchange effects. Many approximate functionals have been developed that yield good results for certain types of molecular systems, however the choice of functional has a large impact on the quality of results from DFT. In many cases, a variety of functionals are used to calibrate and benchmark the results of a study, as was done in Chapter 3.

The Kohn–Sham operator has a similar form to the Fock operator:

$$\boldsymbol{F}^{\sigma\tau} = \boldsymbol{h}^{\sigma\tau} + \delta_{\sigma\tau}\left[\boldsymbol{J}^{\alpha\alpha} + \boldsymbol{J}^{\beta\beta}\right] - \boldsymbol{V}_{xc}^{\sigma\tau} \tag{1.20}$$

where the potential of the exchange correlation functional is given as

$$\boldsymbol{V}_{xc}^{\sigma\tau}(\boldsymbol{x}) = \frac{\partial E_{xc}\left[\rho^{\sigma\tau}\right]}{\partial \rho(\boldsymbol{x})} \tag{1.21}$$

DFT in the generalized Kohn–Sham (GKS) framework requires a change of variables and is discussed further in Chapter 3.

1.3 Time-Dependent Theory and Excited States

In order to simulate spectroscopy, not only the ground state wavefunction must be calculated, but also the relevant excited states and the transition matrix elements that connect them. This requires time-dependent quantum mechanics. As the Hamiltonian is the generator of time translations, either the Schrödinger or Dirac equations can be formulated in a similar manner. That is the time-dependent equation has the form

$$i\frac{\partial}{\partial t}\Psi(\boldsymbol{x}, t) = \hat{H}\Psi(\boldsymbol{x}, t) \tag{1.22}$$

Wavefunction-based approaches such as configuration interaction can often directly calculate excited states. However, with DFT the primary approach is to assume the exchange-correlation functional is the same for excited states and use perturbation theory. One rather straightforward approach is to perturb the ground state system with a potential (such as an electric field) and propogate in time by numerical integration. Equation (1.22) can be

rewritten to use the density matrix in an equation known as the Liouville–von Neumann form:

$$i\frac{\partial}{\partial t}\boldsymbol{P}(t) = [\boldsymbol{F}(t), \boldsymbol{P}(t)] \tag{1.23}$$

At each time t, the density matrix $\boldsymbol{P}(t)$ can be used to calculate given properties of interest, such as the electric dipole moment. The nature of the initial perturbation and the properties to monitor under the time evolution must be chosen to match the experiment. This approach is discussed further in Chapters 2 and 3.

On the other hand, it is possible to transform the perturbed equations to the frequency domain to avoid the cost of explicit time propagation. That is, the perturbation λ is expanded in a series for both the density and Fock matrices:

$$\boldsymbol{P}(t,\lambda) = \boldsymbol{P}^{(0)} + \lambda\frac{\partial \boldsymbol{P}}{\partial \lambda}|_{\lambda=0} + \frac{\lambda^2}{2}\frac{\partial \boldsymbol{P}}{\partial^2 \lambda}|_{\lambda=0} + \cdots \tag{1.24}$$

$$\boldsymbol{F}(t,\lambda) = \boldsymbol{F}^{(0)} + \lambda\frac{\partial \boldsymbol{F}}{\partial \lambda}|_{\lambda=0} + \frac{\lambda^2}{2}\frac{\partial \boldsymbol{F}}{\partial^2 \lambda}|_{\lambda=0} + \cdots \tag{1.25}$$

Collecting terms and retaining those to first order leads to the linear-response equations. At zeroth-order is the commutator relation for the ground state SCF solution:

$$0 = [\boldsymbol{F}^{(0)}, \boldsymbol{P}^{(0)}] \tag{1.26}$$

And at first order:

$$\omega_\lambda \boldsymbol{P}^{(\lambda)} = [\boldsymbol{F}^{(0)}, \boldsymbol{P}^{(\lambda)}] + [\boldsymbol{F}^{(\lambda)}, \boldsymbol{P}^{(0)}] \tag{1.27}$$

where ω_λ corresponds to the frequency of the perturbation. These equations are able to be recast as a generalized eigenvalue problem of the form

$$\boldsymbol{H}v = \omega \boldsymbol{M}v \tag{1.28}$$

where $\boldsymbol{H}$ is the orbital Hessian and $\boldsymbol{M}$ is a metric. Iterative diagonalization is then used to obtain transition vectors v and the excitation energies ω. The transition vectors v determine the transition densities T, from which one can then evaluate the related properties such as the transition dipole moment This approach to compute excited states and spectra will be discussed in more detail in Chapters 4, 5, and 6.

Chapter 2

REAL-TIME PROPAGATION OF THE EXACT TWO-COMPONENT TIME-DEPENDENT DENSITY FUNCTIONAL THEORY

We report the development of a real-time propagation method for solving the time-dependent relativistic exact two-component density functional theory equations (RT-X2C-TDDFT). The method is fundamentally non-perturbative and may be employed to study nonlinear responses for heavy elements, which require a relativistic Hamiltonian. We apply the method to several group-12 atoms as well as heavy-element hydrides, comparing with the extensive theoretical and experimental studies on this system, which demonstrates the correctness of our approach. Because the exact two-component Hamiltonian contains spin-orbit operators, the method is able to describe the non-zero transition moment of otherwise spin-forbidden processes in non-relativistic theory. Furthermore, the two-component approach is more cost effective than the full four-component approach, with similar accuracy. The RT-X2C-TDDFT will be useful in future studies of systems containing heavy elements interacting with strong external fields. The work in this section is adapted with permission from Joshua J. Goings, Joseph M. Kasper, Franco Egidi, Shichao Sun, and Xiaosong Li, *J. Chem. Phys*, **2016**, *145 (10)*, 104107. Copyright 2016 American Institute of Physics. For this work I was involved in the development and testing of the two-component real-time code as well as running the calculations for the heavy-element hydrides.

2.1 Introduction

Relativistic effects are known to be important for the description of heavy elements. For example, the yellow color of gold and the fact that mercury is liquid at room temperature

cannot be explained by the Schrödinger equation, but are predicted using the Dirac equation [9, 10, 11]. The proper starting point for the description of molecular relativistic effects is the Dirac–Hartree–Fock/Dirac–Kohn–Sham four-component Hamiltonian. However, because of its four-component nature, the Dirac–Hartree–Fock/Dirac–Kohn–Sham Hamiltonian quickly becomes an expensive Hamiltonian to use in realistic calculations involving heavy elements. Furthermore, there is additional work in the full four-component calculations in that the Dirac equation also contains negative energy solutions corresponding to positronic solutions [9, 10]. These are often of little interest to chemical applications. Therefore, much effort has been spent to decouple the four-component equations into two-component electronic and positronic equations, which retain the physical relativistic effects of the full four-component equations, but at reduced cost [9, 10].

One of the most promising two-component methods in recent times has been the introduction of the exact two-component transformation (X2C) [12, 13, 14, 15, 16, 17, 18, 19, 20, 21]. X2C approximately decouples the parent four-component Hamiltonian into a reduced dimension electronic two-component Hamiltonian. For one-electron systems, X2C will recover the exact four-component eigenspectrum of the underlying four-component Dirac equation. Other two-component methods of note are the normalized elimination of the small component (NESC) [22, 23, 24, 25, 26], the Douglas–Kroll–Hess transformation [27, 28, 29, 30], and the zeroth-order regular approximation (ZORA) [19, 31, 32, 33]. Relations between these methods have been detailed in Ref. 20.

Given the success of such relativistic Hamiltonians for ground state properties, it is natural to consider the effectiveness of their extension to excited state properties, such as optical absorption spectra. In particular, relativistic effects are necessary to qualitatively describe excited states split by spin-orbit and spin-spin interactions. Both four-component and two-component relativistic Hamiltonians have been successfully applied to the description of excited states using the linear-response (LR) formalism [34, 35, 36, 37, 38, 39, 40, 41, 42, 43, 44, 45]. However, the linear-response formalism is fundamentally limited to system response of small, perturbative fields. If one desires to compute nonlinear response properties and the

response of systems containing heavy elements in strong fields, it may be necessary to employ a real-time propagation approach [46, 47, 48] to the time-dependent relativistic equations.

Recently, a real-time (RT) propagation approach for the four-component Dirac-Kohn-Sham equations was presented [49]. The method was able to describe the response of strong fields to systems within a fully relativistic theory, and was able to describe spin-forbidden transitions and other unique relativistic aspects of optical absorption spectra. Unfortunately, because of the underlying four-component Hamiltonian, the solution of the equations is rather expensive. Here, we present a real-time propagation approach utilizing the time-dependent two-component X2C Hamiltonian. The solution of these equations provides an economical approach to describing the response of systems containing heavy elements. We briefly describe the two component transformation and our real-time propagation scheme for two component Hamiltonians, based off our previous work propagating non-relativistic two-component equations [48, 50]. We demonstrate the correctness of our approach by comparing these calculations with linear response two-component time-dependent density functional theory (TDDFT), as well as the four-component RT-TDDFT results. Finally, we look forward to the potential of real-time time-dependent X2C for strong fields and spin-dependent dynamics.

2.2 Theory

Here we briefly outline the exact two-component transformation, using atomic units. We follow the notation of Peng, *et al.*, as our implementation closely follows the X2C implementation outlined in their paper [17]. Bold formatting $\boldsymbol{M}$ indicates matrices in two-component (2c) space and for matrix representation of four-component operators we use the split notation for large (L) and small (S) components. In some cases, four-component (4c) matrices will be indicated by blackboard bold $\mathbb{M}$. Finally, sans-serif matrices M correspond to complex matrices in a basis set of spin-free functions. We refer interested readers to Ref. 17 for more details. The goal of X2C, as with most two-component methods, is to exactly decouple the large and small components of the four-component one-electron modified Dirac

equation. X2C accomplishes this goal by exactly decoupling the one-electron Dirac equation represented in a restricted kinetically balanced basis, given as

$$\begin{pmatrix} \boldsymbol{V} & \boldsymbol{T} \\ \boldsymbol{T} & (\frac{1}{4c^2}\boldsymbol{W} - \boldsymbol{T}) \end{pmatrix} \begin{pmatrix} \boldsymbol{C}_L^+ & \boldsymbol{C}_L^- \\ \boldsymbol{C}_S^+ & \boldsymbol{C}_S^- \end{pmatrix} = \begin{pmatrix} \boldsymbol{S} & \mathbf{0} \\ \mathbf{0} & \frac{1}{2c^2}\boldsymbol{T} \end{pmatrix} \begin{pmatrix} \boldsymbol{C}_L^+ & \boldsymbol{C}_L^- \\ \boldsymbol{C}_S^+ & \boldsymbol{C}_S^- \end{pmatrix} \begin{pmatrix} \boldsymbol{\epsilon}^+ & \mathbf{0} \\ \mathbf{0} & \boldsymbol{\epsilon}^- \end{pmatrix} \tag{2.1}$$

Here $\boldsymbol{V}$, $\boldsymbol{T}$, and $\boldsymbol{S}$ are the non-relativistic matrix representations of the one-electron potential energy operator ($\mathcal{V}$), the kinetic energy operator, and the overlap, respectively. $\boldsymbol{W}$, however, is the relativistic potential energy operator, represented as

$$W_{ij} = \langle \chi_i | \ \vec{\sigma} \cdot \vec{p} \ \mathcal{V} \ \vec{\sigma} \cdot \vec{p} \ | \chi_j \rangle \tag{2.2}$$

where $\vec{p}$ is the linear momentum vector and $\vec{\sigma}$ is the vector containing the Pauli spin operators. All the matrices are represented over two-component spinor functions, $\{\chi_i\}$. Finally, c is the speed of light and $\mathbf{C}$ and ϵ collect the wavefunction coefficients and orbital energies, respectively.

To decouple Eq. (2.1), we seek a unitary transformation $\mathbb{U}$ that block diagonalizes the 4c Dirac Hamiltonian into two, two-component equations. The decoupled equations will correspond to positive and negative energy states, and we seek solutions only to the positive energy solutions, which correspond to electronic solutions. Mathematically, we seek to find $\mathbb{U}$ such that

$$\begin{pmatrix} \tilde{\boldsymbol{H}}^+ & \mathbf{0}_2 \\ \mathbf{0}_2 & \tilde{\boldsymbol{H}}^- \end{pmatrix} = \tilde{\mathbb{H}} = \mathbb{U}^\dagger \mathbb{H} \mathbb{U} \tag{2.3}$$

In the X2C method, the matrix representation of $\mathbb{U}$ is given by

$$\mathbb{U} = \begin{pmatrix} \boldsymbol{U}^{LL} & \boldsymbol{U}^{LS} \\ \boldsymbol{U}^{SL} & \boldsymbol{U}^{SS} \end{pmatrix} = \begin{pmatrix} \frac{\boldsymbol{I}}{\sqrt{\boldsymbol{I}+\boldsymbol{X}'^\dagger \boldsymbol{X}'}} & -\boldsymbol{X}'^\dagger \frac{\boldsymbol{I}}{\sqrt{\boldsymbol{I}+\boldsymbol{X}'\boldsymbol{X}'^\dagger}} \\ \boldsymbol{X}' \frac{\boldsymbol{I}}{\sqrt{\boldsymbol{I}+\boldsymbol{X}'^\dagger \boldsymbol{X}'}} & \frac{\boldsymbol{I}}{\boldsymbol{I}+\boldsymbol{X}'\boldsymbol{X}'^\dagger} \end{pmatrix} \tag{2.4}$$

which only holds in an orthonormal basis, denoted by the primes. The X2C method extracts a matrix representation of $\boldsymbol{X}'$ by diagonalizing the one-electron modified Dirac Hamiltonian in an orthonormal basis.

$$\mathbb{H}' \begin{pmatrix} \boldsymbol{C}_{L'}^+ \\ \boldsymbol{C}_{S'}^+ \end{pmatrix} = \begin{pmatrix} \boldsymbol{C}_{L'}^+ \\ \boldsymbol{C}_{S'}^+ \end{pmatrix} \boldsymbol{\epsilon}^+ \tag{2.5}$$

From the solution of Eq. (2.5), the explicit matrix expression for $\boldsymbol{X}'$ can be obtained from the wavefunction coefficients

$$\boldsymbol{X}' = \boldsymbol{C}^{+}_{S'} \cdot \left(\boldsymbol{C}^{+}_{L'}\right)^{-1} \tag{2.6}$$

Plugging Eq. (2.6) into Eq. (2.4) the X2C Hamiltonian is then given by

$$\tilde{\boldsymbol{H}}^{+} = \begin{pmatrix} \boldsymbol{U}^{LL,\dagger} & \boldsymbol{U}^{SL,\dagger} \end{pmatrix} \begin{pmatrix} \boldsymbol{V} & \boldsymbol{T} \\ \boldsymbol{T} & (\frac{1}{4c^2}\boldsymbol{W} - \boldsymbol{T}) \end{pmatrix} \begin{pmatrix} \boldsymbol{U}^{LL} \\ \boldsymbol{U}^{SL} \end{pmatrix} \tag{2.7}$$

The extension to many-electron systems corresponds to the same transformation in Eq. (2.7) but for the modified four-component Dirac–Hartree–Fock equation. In our implementation, we do not transform the matrix representation of the two-electron operator. This is equivalent to the Dirac–Coulomb approximation for the two-electron operator. We do however, include an empirical correction in the one-electron terms to account for the screening due to the two-electron terms [51]. Furthermore, the two-electron interactions depend on the X2C density, which generates some relativistic dependence to the two electron interaction.

$$\mathsf{F}^{\sigma\sigma'} = \mathsf{h}^{\sigma\sigma'} + \delta_{\sigma\sigma'}\mathsf{J}\left(\mathsf{P}^{\alpha\alpha} + \mathsf{P}^{\beta\beta}\right) - \theta\mathsf{K}\left(\mathsf{P}^{\sigma\sigma'}\right) - (1-\theta)\mathsf{V}_x^{\mathrm{DFT}}\left(\mathsf{P}^{\sigma\sigma'}\right) + \mathsf{V}_c^{\mathrm{DFT}}\left(\mathsf{P}^{\sigma\sigma'}\right) \tag{2.8}$$

Here h contains the transformed one-electron integrals, J contains the Coulomb integrals, and K contains the exchange integrals. σ denotes a spin-projection component, spin-up (α) or spin-down (β). $\mathsf{V}_x^{\mathrm{DFT}}$ and $\mathsf{V}_c^{\mathrm{DFT}}$ are the DFT exchange and correlation functionals, respectively. θ denotes a mixing parameter that mixes in a certain amount of Hartree-Fock exchange. For pure DFT θ is zero and for pure Hartree-Fock $\theta = 1$. (For pure Hartree-Fock we omit $\mathsf{V}_c^{\mathrm{DFT}}$ as well.)

Density functionals commonly developed for quantum chemical calculations are only formulated for systems with a collinear density for which the spin magnetization is oriented along the z axis at every point in space. Common exchange-correlation kernels only depend on $\mathsf{P}^{\alpha\alpha}$ and $\mathsf{P}^{\beta\beta}$ therefore, in order to use such functionals to describe systems with a non-collinear spin magnetization, the functional dependence must be reformulated to account for

the presence of a non-zero magnetization oriented along the x and y directions, as well as their gradients (in the case of GGA functionals) in Eq. (2.8). The non-collinear XC kernel for 4c methods has been explored by Liu, *et al.* [34, 40, 41, 52] We employ a recently reported formalism [53, 54, 55, 56] that defines a set of auxiliary variables, detailed in Ref. 55, that take all magnetization components into account. This form has the advantage of exerting a non-zero local torque acting on the magnetization, while yielding a vanishing total torque, as expected from the exact functional [57].

To propagate the X2C equations in time, we must consider the time-dependent version of the X2C Hamiltonian.

$$i\frac{\partial}{\partial t}\begin{pmatrix} \mathsf{P}^{\alpha\alpha}(t) & \mathsf{P}^{\alpha\beta}(t) \\ \mathsf{P}^{\beta\alpha}(t) & \mathsf{P}^{\beta\beta}(t) \end{pmatrix} = \left[\begin{pmatrix} \mathsf{F}^{\alpha\alpha}(t) & \mathsf{F}^{\alpha\beta}(t) \\ \mathsf{F}^{\beta\alpha}(t) & \mathsf{F}^{\beta\beta}(t) \end{pmatrix}, \begin{pmatrix} \mathsf{P}^{\alpha\alpha}(t) & \mathsf{P}^{\alpha\beta}(t) \\ \mathsf{P}^{\beta\alpha}(t) & \mathsf{P}^{\beta\beta}(t) \end{pmatrix}\right] \tag{2.9}$$

We integrate Eq. (2.9) with a modified midpoint and unitary transformation (MMUT) algorithm[46, 58, 59]. In the MMUT method, the time-evolution operator is a unitary transformation matrix $\mathbf{Q}(t_n)$ that is constructed from the eigenvectors $\mathbf{C}(t_n)$ and eigenvalues $\boldsymbol{\epsilon}(t_n)$ of the X2C Hamiltonian matrix at time t_n:

$$\boldsymbol{C}^{\dagger}(t_n)\cdot\boldsymbol{F}(t_n)\cdot\boldsymbol{C}(t_n) = \boldsymbol{\epsilon}(t_n) \tag{2.10}$$

and

$$\begin{aligned}\boldsymbol{Q}(t_n) &= \exp\left[-i\cdot 2\Delta t\cdot\boldsymbol{F}(t_n)\right] \\ &= \boldsymbol{C}(t_n)\cdot\exp\left[-i\cdot 2\Delta t\cdot\boldsymbol{\epsilon}(t_n)\right]\cdot\boldsymbol{C}^{\dagger}(t_n)\end{aligned} \tag{2.11}$$

where Δt is the time step. Then, the density matrix is propagated from time t_{n-1} to t_{n+1} using the time-evolution operator $\mathbf{Q}(t_n)$:

$$\boldsymbol{P}(t_{n+1}) = \boldsymbol{Q}(t_n)\cdot\boldsymbol{P}(t_{n-1})\cdot\boldsymbol{Q}^{\dagger}(t_n) \tag{2.12}$$

The MMUT method accounts for linear changes in the density matrix during the time step because it computes the X2C Hamiltonian matrix at the midpoint. MMUT is a symplectic

integration scheme which allows for a large step size, while simultaneously controlling for numerical noise and integration errors [46].

To excite all dipole-allowed electronic transitions, it is necessary to perturb Eq. (2.8) with an electric field along each real-space coordinate (e.g. x, y, z). This modifies the X2C Hamiltonian matrix such that

$$\boldsymbol{F}_{\mathrm{E}}(t) = \boldsymbol{F}(t) + \sum_{q=x,y,z} \kappa_q(t)\langle r_q \rangle \tag{2.13}$$

where $\boldsymbol{F}_{\mathrm{E}}(t)$ is the time-dependent X2C Hamiltonian matrix containing the external electric field, $\kappa_q(t)$ is the field strength at time t along direction q, and $\langle r_q \rangle$ are the atomic-orbital based length-gauge dipole integrals along component q. The electric dipole operator matrix $\langle r_q \rangle$ used in the propagation is subject to the X2C picture-change transformation. In the electric-dipole approximation in the length gauge, the electric field does not couple different spin components [60, 48]. As a result, the X2C transformation matrix is invariant with respect to an external electric field perturbation. Therefore, the same X2C transformation matrix is used to transform the electric dipole operator matrix that goes into Eq. (2.13).

Because time is discretized, the perturbation corresponds to a step function lineshape lasting for only the initial time-step of width Δt, e.g.

$$\kappa_q(t) = \begin{cases} \kappa_{\max}, & 0 \leq t < \Delta t, \\ 0, & \text{else} \end{cases} \tag{2.14}$$

where $\kappa_{\max}$ is the field strength. One important caveat for including the electric dipole field in the X2C equations is that the atomic orbital electric dipole integrals must also be transformed using the transformation matrix in Eq. (2.4). This corrects for the so-called "picture-change" error in two-component methods that originates from transforming the four-component picture to the two-component picture [61].

2.3 Results and Discussion

The real-time propagation of the X2C Hamiltonian was implemented in a locally modified copy of the developer's version of the Gaussian electronic structure program [5]. All calcula-

tions were performed using the SVWN5 [62, 63] density functional with the Sapporo-DKH3-DZP-2012 gaussian basis set including diffuse-*sp* functions [64]. The density functional and basis set were chosen in order to be able to compare with existing relativistic response theory implementations, which will be discussed below. After a ground state density optimization, each system was perturbed with an electric dipole delta pulse corresponding to a $\kappa_{\max}$ of 0.0001 atomic units along each unique Cartesian axis. Each real-time calculation was propagated using a maximum time step of 0.0012 fs for at least 50 fs. Energy was conserved to at least 10^{-8} Hartree. To accelerate the convergence of the Fourier transform, a Padé transformation scheme was utilized [65]. The electric dipole response was exponentially damped so as to give each peak a Lorentzian line shape with full-width half-maximum of 0.01 eV.

To obtain the optical absorption spectra, we take the Fourier transform of the time-dependent electric dipole moment $\mu(\omega)$ parallel to the polarization of the electric field perturbation κ. This corresponds to the frequency-dependent polarizability. The isotropic dipole strength function $S(\omega)$ is proportional to the imaginary component of the trace of the frequency dependent polarizability. That is to say,

$$S(\omega) \propto \sum_{\alpha=x,y,z} \mathrm{Tr}\left[\omega \cdot \mathrm{Im}\frac{\mu_\alpha(\omega)}{\kappa_\alpha}\right] \tag{2.15}$$

In order to test our implementation, we follow the pioneering four-component RT-TDDFT work of Repisky, *et al.* [49] and choose to study the excitation energies of three group-12 atoms and two heavy-element hydrides. This allows us to compare not only with a four-component RT-TDDFT implementation, but also to compare with several four-component and two-component relativistic LR-TDDFT implementations [34, 35, 36, 37, 38]. Furthermore, there exist robust experimental data for these systems, which allows us to compare directly with experiment. For the heavy-element hydrides, TlH and AuH, experimental equilibrium geometries were used ($r_{Tl-H} = 1.8702$ Å, $r_{Au-H} = 1.52385$ Å) in accordance with previous investigations [66, 67].

We begin by investigating the group-12 atoms, which have been throughly investigated both experimentally and theoretically. The states that we investigate correspond to s to

p type transitions. Because our RT-TDDFT method can only detect electronically allowed transitions, the only reason we are able to detect the singlet-to-triplet transitions (the $^3P_1$ states) is because the two-component X2C Hamiltonian includes spin-orbit couplings which allow the otherwise spin-forbidden transitions to become weakly allowed by mixing with the $^1P_1$ state. The spectra are given in Fig. 2.1. For Zn (and to some extent Cd), the spin-forbidden transition appears almost non-existent. Despite this, the two-component X2C RT-TDDFT method can still predict a slight optical transition, which is observed experimentally. By the time we get to Hg, the singlet to triplet transition is relatively bright. A comparison of our results with both four-component RT-TDDFT and four- and two-component LR-TDDFT is given in Tab. 2.1. In general we find excellent agreement with both four- and two-component methods for RT-TDDFT and LR-TDDFT, as well as the experimental values obtained from Ref. 66. The relatively slight differences between methods likely corresponds to differences in the choice of basis set.

Finally, we compare our results for two diatomic heavy-element hydrides, TlH and AuH. These too have been the subject of much experimental and theoretical studies. Plots of the computed absorption spectrum are given in Figs. 2.2 and 2.3 and comparison of selected low energy states with existing theoretical methods are given in Tab. 2.2. For TlH, we examine the two lowest-energy states, corresponding to $^3\Pi$ and $^1\Pi$ states. Our results for TlH agree very closely with the two-component ZORA with Slater-type functions obtained by Wang, *et al.*. We observe a non-zero transition moment to the $^3\Pi$ state, which is possible only because our two-component X2C Hamiltonian contains spin-orbit interactions to allow this otherwise spin-forbidden transition. We observe a similar behavior with AuH, and our results are only a few hundredths of an eV different from both four- and two- component results. We also note that our results, along with the other literature results, agree strongly with the experimental data, taken from Ref. 67.

2.4 Conclusion

Here we have implemented a real-time propagation method for solving the relativistic two-component time-dependent X2C equations within the context of density functional theory. We have compared our results for a variety of simple benchmark systems that have been thoroughly investigated by four- and two-component relativistic methods based on both real-time and linear-response approaches. Our results show very good agreement with previous studies. We show that the accuracy of our method is comparable to the full four-component relativistic equations, yet with reduced cost because we work within the two-component space. This is the clearest advantage over the previously reported real-time four-component TDDFT method. Because the real-time approach is fundamentally non-perturbative, this method is easily extended to study non-linear responses and molecules in strong fields, which is not possible within the linear-response formalism. Additionally, because the two component X2C includes spin-orbit operators, this method will be suitable for the description of otherwise spin-forbidden transitions as well as for the description of spin-orbit corrections to high-energy excited states, such as those found in X-ray spectroscopy.

Table 2.1: Calculated $ns^2 \rightarrow ns^1np^1$ Excitation Energies of group-12 Atoms ($n = 4 - 6$ for Zn, Cd, Hg)

		Excitation Energy (eV)							
		RT-TDDFT		LR-TDDFT					
atom	state	this work	Repisky[49]	Gao[34]	Bast[35]	Wang[36]	Nakata[38]	Kühn[37]	exp[66]
Zn	$^1P_1$	5.90	5.84	6.07	5.76	5.76	6.20	—	5.80
	$^3P_1$	4.30	4.30	4.40	4.35	4.35	4.41	—	4.03
Cd	$^1P_1$	5.31	5.44	5.50	5.34	5.35	5.74	5.47	5.42
	$^3P_1$	3.82	4.02	4.04	4.02	4.02	4.11	4.12	3.80
Hg	$^1P_1$	6.99	6.56	6.66	6.53	6.53	6.85	6.57	6.70
	$^3P_1$	5.24	5.06	5.12	5.08	5.09	5.26	5.12	4.89

Table 2.2: Vertical Excitation Energies of Low-Lying Electronic States of TlH and AuH

		Excitation Energy (eV)					
		RT-TDDFT		LR-TDDFT			
molecule	state	this work	Repisky[49]	Wang[36]	Gao[34]	Kühn[37]	exp[67]
TlH	$^3\Pi$	2.10	2.07	2.08	—	2.09	2.20
	$^1\Pi$	2.88	2.96	2.88	—	2.64	3.00
AuH	$^1\Sigma^+$	3.48	3.31	3.42	3.39	—	3.43
	$^3\Pi$	4.65	4.52	4.70	4.66	—	4.78
	$^1\Pi$	4.98	5.21	5.01	4.96	—	5.32

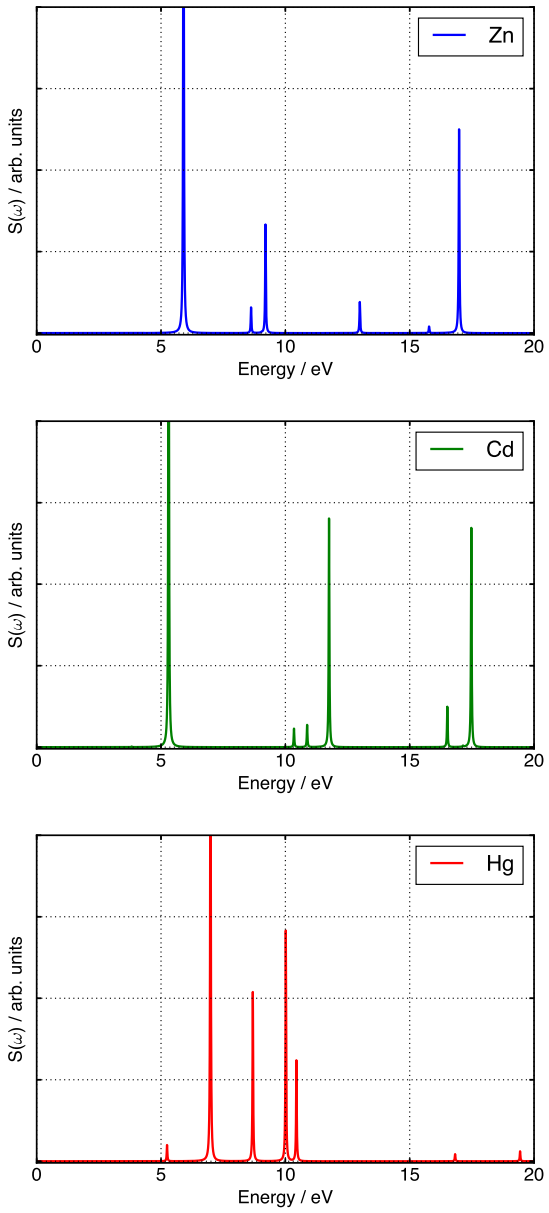

Figure 2.1: Computed optical absorption spectra of (a) Zn, (b) Cd, and (c) Hg using RT-X2C-TDDFT within the SVWN5/Sapporo-DKH3-2012 level of theory with diffuse-*sp* functions.

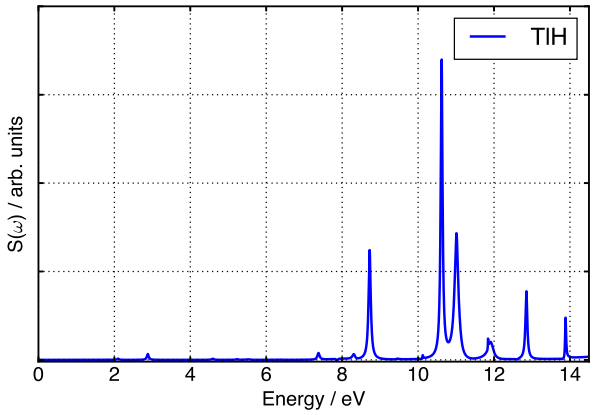

Figure 2.2: Computed optical absorption spectra of TlH using RT-X2C-TDDFT within the SVWN5/Sapporo-DKH3-2012 level of theory with diffuse-*sp* functions. The TlH bond length corresponds to an experimental equilibrium length of 1.8702 Å.

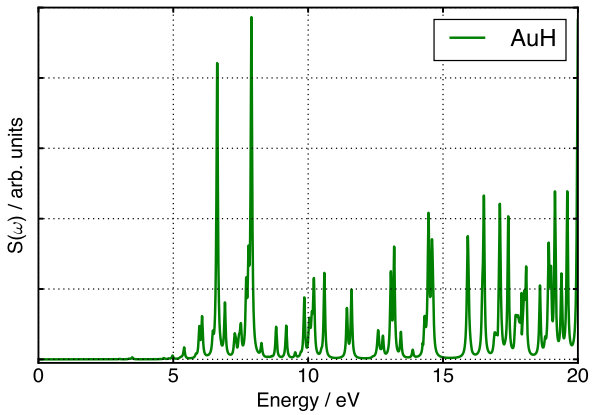

Figure 2.3: Computed optical absorption spectra of AuH using RT-X2C-TDDFT within the SVWN5/Sapporo-DKH3-2012 level of theory with diffuse-*sp* functions. The AuH bond length corresponds to an experimental equilibrium length of 1.52385 Å.

Chapter 3

MODELING $L_{2,3}$-EDGE XAS WITH REAL-TIME EXACT TWO-COMPONENT RELATIVISTIC TIME-DEPENDENT DENSITY FUNCTIONAL THEORY

X-ray absorption spectroscopy is a powerful technique to probe local electronic and nuclear structure. There has been extensive theoretical work modeling K-edge spectra from first principles. However, modeling L-edge spectra directly with density functional theory poses a unique challenge requiring further study. Spin-orbit coupling must be included in the model and a non-collinear density functional theory is required. Using the real-time exact two-component method, we are able to variationally include one-electron spin-orbit coupling terms when calculating the absorption spectrum. The abilities of different basis sets and density functionals to model spectra for both closed- and open-shell systems are investigated using $SiCl_4$ and three transition metal complexes: $TiCl_4$, CrO_2Cl_2, and $[FeCl_6]^{3-}$. Although we are working in the real-time framework, individual molecular orbital transitions can still be recovered by projecting the density onto the ground state molecular orbital space and separating contributions to the time-evolving dipole moment. The work in this section is adapted with permission from Joseph M. Kasper, Patrick J. Lestrange, Torin F. Stetina, and Xiaosong Li. *J. Chem. Theor. Comput.*,**2018**,*14 (4)*,1998–2006. Copyright 2018 American Chemical Society.

3.1 Introduction

X-ray absorption spectroscopy (XAS) is an element-specific probe that has been used to understand the local electronic and binding environment around metal centers. It has been useful in describing the oxidation states of metal complexes [68], differential orbital covalency

[4], and local site symmetry [69]. In recent years, it has become a more routine experimental technique as advanced synchrotron and benchtop radiation sources are now able to provide highly tuned beams in the soft and hard X-ray regimes [70, 71, 72, 73, 74]. Electronic structure theory is often an important aid in interpreting and characterizing X-ray absorption spectra. The abilities of many non-relativistic techniques have been thoroughly characterized, but more recently developed relativistic methods have not yet been analyzed in great detail.

Relativistic effects are important considerations when picking a method to describe XAS. K-edge spectra are generated from excitations out of $1s$ orbitals, and L-edge spectra from excitations out of orbitals with principal quantum number 2. These core electrons move at an appreciable percentage of the speed of light, so non-relativistic approximations are not able to describe them accurately. For K-edge spectra, including relativistic effects lead to a contraction of the $1s$ orbital, which shifts it to lower energy and causes the entire XAS spectrum to be blue shifted relative to a spectrum calculated with a non-relativistic Hamiltonian. Since the valence orbitals are not strongly effected by relativistic effects, K-edge spectra modeled with a non-relativistic Hamiltonian are often uniformly shifted to higher energies to match experimental spectra [75, 76, 77, 78, 79]. Accurate L-edge spectra, on the other hand, cannot be obtained from non-relativistic Hamiltonians so easily.

In addition to contraction of the $2s$ and $2p$ orbitals, spin-orbit coupling splits the degenerate $2p$ orbitals into two sets, $2p_{1/2}$ and $2p_{3/2}$ from which to generate a core-hole state. Excitations out of these orbitals are therefore separated into two absorption edges, L_2 and L_3. An approach that includes spin-orbit coupling is necessary to accurately describe these spectra correctly. L-edge spectra are of great interest because like K-edge spectra they are element specific probes, but they have a much finer intrinsic linewidth than K-edge spectra due to longer core-hole lifetimes [80]. The spectral features are also much more intense than many K-edge features, which are often only quadrupole-allowed. This means that transition probabilities are significantly easier to model for L-edge spectra because they are dipole-allowed, so issues with origin-dependence need not be considered [76, 81, 82, 83, 84].

There have been many *ab initio* approaches to model core excitation spectra in the

past. K-edge spectra have been obtained with linear response time-dependent density functional theory (LR-TDDFT)[77, 79, 85, 86, 87, 88, 89], real-time TDDFT (RT-TDDFT)[90], algebraic-diagramatic construction [91, 92, 93] and coupled cluster theory using the complex polarization propagator [94, 95] and the equation-of-motion formalisms [79]. Multiconfigurational methods like the restricted active space (RAS) approach have been applied to model both K- and L-edge spectra by including the relevant core orbitals in the active space. In this approach spin-orbit coupling is included in a perturbative scheme coupling non-relativistic wave functions of varying spin [96, 97]. This perturbative scheme has also been used to model L-edge spectra with an approach combining restricted open-shell configuration interaction singles (ROCIS) and density functional theory (DFT) [98, 99]. Recently, a real-time four-component relativistic TDDFT method has been developed to model the L-edge spectra including spin-orbit coupling variationally [100].

Two-component variational relativistic TDDFT methods are an attractive alternative to its four-component equivalent due to its excellent balance between the computational cost and theoretical accuracy (see the Theory section for references and detailed discussion on the two-component DFT and TDDFT methods). In addition, existing eigensolvers and propagation methods developed for single-component TDDFT for modeling XAS can be easily modified and applied to two-component variational relativistic TDDFT methods provided with a non-collinear extension of the DFT kernels. In this work, we investigate the ability and characteristics of two-component relativistic TDDFT using a non-collinear implementation of standard density functionals to model L-edge spectra of first-row transition metals. One-electron spin-coupling is variationally included in the non-collinear formalism of relativistic DFT and real-time exact two-component time-dependent density functional theory (RT-X2C-TDDFT)[101, 102] that is used to model the $L_{2,3}$-edge spectra. Although both linear response and the real-time method used here should produce identical results, as has been noted elsewhere[103], the number of states required to build a spectrum in the X-ray region is quite high, while real-time affords the entire spectrum at once.

3.2 Theory

3.2.1 Exact Two-component Transformation

The four-component (4c) relativistic Dirac Hamiltonian is expressed as

$$\hat{H}^{4c} = \begin{pmatrix} V\mathbf{I} & c\boldsymbol{\sigma}\cdot\mathbf{p} \\ c\boldsymbol{\sigma}\cdot\mathbf{p} & (V-2mc^2)\mathbf{I} \end{pmatrix} \tag{3.1}$$

where V is the scalar potential, $\boldsymbol{\sigma}$ is the vector of Pauli matrices, $\mathbf{p}$ is the linear momentum operator, and $\mathbf{I}$ is the rank-two identity matrix. The speed of light and mass of the electron are c and m. Eigenstates of this Hamiltonian can be separated into large (L) and small (S) components

$$\Psi^{4c} = \begin{pmatrix} \Psi_L \\ \Psi_S \end{pmatrix} \tag{3.2}$$

which are themselves separated into spin-up and spin-down components. Both positive- and negative-energy solutions to the 4c Dirac equation can be obtained, pertaining to electron and positron states respectively. Positron solutions have little relevance to chemical problems, so methods that decouple them from the electronic solutions via a unitary transformation have been developed

$$\boldsymbol{\mathcal{U}}^{\dagger}\hat{H}^{4c}\boldsymbol{\mathcal{U}} = \begin{pmatrix} \hat{H}^{+} & \mathbf{0}_2 \\ \mathbf{0}_2 & \hat{H}^{-} \end{pmatrix} ; \boldsymbol{\mathcal{U}}\begin{pmatrix} \Psi_L \\ \Psi_S \end{pmatrix} = \begin{pmatrix} \Psi^{2c} \\ \mathbf{0} \end{pmatrix} \tag{3.3}$$

The Hamiltonians $\hat{H}^{+}$ and $\hat{H}^{-}$ have two-component (2c) eigenstates Ψ^{2c} and describe positive- and negative-energy states respectively. In practice, the transformation matrix $\boldsymbol{\mathcal{U}}$ cannot be formed exactly, so approximate transformations must be used. There are many different techniques to form the transformation matrix $\boldsymbol{\mathcal{U}}$, such as the normalized elimination of the small component [22, 23, 24, 25, 26], the Douglas-Kroll-Hess transformation [27, 28, 29, 30], and the zeroth-order regular approximation [19, 31, 32, 33]. The exact two-component (X2C) method is a popular method that exactly separates the one-electron 4c Hamiltonian, but

only approximately decouples the large and small components in the many-electron case [12, 13, 14, 15, 16, 17, 39, 42, 43, 44, 101, 104, 105]. In practice, the two-electron operator is not transformed as this can become very computationally expensive. An empirical correction to the one-electron terms is instead included to account for this [51]. In this work, we use a direct atomic-orbital based X2C transformation as described in Refs. 39, 105. The following discussion assumes that an appropriate 4c→2c transformation has been achieved and all matrix quantities are in the transformed two-component framework.

3.2.2 Two-component Relativistic Non-collinear Density Functional Theory

For two-component methods, the density can be represented in spin-blocked form or as a sum of the total density n and the vector magnetization density $\mathbf{m}$

$$\mathbf{P} = \begin{pmatrix} \mathbf{P}^{\alpha\alpha} & \mathbf{P}^{\alpha\beta} \\ \mathbf{P}^{\beta\alpha} & \mathbf{P}^{\beta\beta} \end{pmatrix} \tag{3.4}$$

$$= \frac{1}{2} n(\mathbf{r}) \sigma_0 + \frac{1}{2} \mathbf{m}(\mathbf{r}) \circ \boldsymbol{\sigma} \tag{3.5}$$

where the circle '$\circ$' is used to denote a scalar product over the magnetization spin labels of any two quantities ($\mathbf{a} \circ \mathbf{b} = \sum_{k=x,y,z} a_k b_k$). The diagonal blocks in Eq. (3.4) are the collinear densities oriented along the z axis and the off-diagonal blocks represent the non-collinear parts of the density in the x and y directions. Commonly used density functional approximations that only depend on the collinear densities must be modified to be compatible with 2c Hamiltonians. This is a nontrivial extension of existing DFT functionals and has led to many unique formalisms [12, 13, 34, 35, 36, 37, 40, 45, 52, 53, 54, 55, 56, 57, 105, 106, 107, 108, 109, 110, 111, 112].

The non-collinear DFT framework used in this work redefines the functionals (in the similar spirit of spin-polarized DFT) to depend on a set of auxiliary generalized variables which take the full magnetization vector density into account,[54, 55, 56, 105]

$$E_{\mathrm{xc}} = \int f(n_+, n_-, \gamma_{++}, \gamma_{--}, \gamma_{+-}, \tau_+, \tau_-) d\mathbf{r} \tag{3.6}$$

where the generalized variables are defined as follows

$$
\begin{aligned}
n^{\pm} &= \frac{1}{2}n \pm \frac{1}{2}\sqrt{\mathbf{m}\circ\mathbf{m}} \\
\gamma^{\pm\pm} &= \frac{1}{4}\boldsymbol{\nabla}n\cdot\boldsymbol{\nabla}n + \frac{1}{4}\boldsymbol{\nabla}\mathbf{m}\cdot\circ\boldsymbol{\nabla}\mathbf{m} \pm \frac{f_{\nabla}}{2}\sqrt{\boldsymbol{\nabla}n\cdot\boldsymbol{\nabla}\mathbf{m}\circ\boldsymbol{\nabla}\mathbf{m}\cdot\boldsymbol{\nabla}n} \\
\gamma^{+-} &= \frac{1}{4}\boldsymbol{\nabla}n\cdot\boldsymbol{\nabla}n - \frac{1}{4}\boldsymbol{\nabla}\mathbf{m}\cdot\circ\boldsymbol{\nabla}\mathbf{m} \\
\tau^{\pm} &= \frac{1}{2}\tau \pm \frac{f_{\mathbf{u}}}{2}\sqrt{\mathbf{u}\circ\mathbf{u}} \\
f_{\nabla} &= \mathrm{sgn}(\boldsymbol{\nabla}n\cdot\boldsymbol{\nabla}\mathbf{m}\circ\mathbf{m}) \\
f_{\mathbf{u}} &= \mathrm{sgn}(\mathbf{u}\circ\mathbf{m})
\end{aligned}
\tag{3.7}
$$

In the expression above, τ and $\mathbf{u}$ are the total and magnetization vector kinetic energy densities, while 'sgn' indicates the sign function. The dot '$\cdot$' and circle '$\circ$' operators are defined so that the former only contracts indices of the gradient operator $\boldsymbol{\nabla}$, while the latter contracts indices of $\mathbf{m}$ and $\mathbf{u}$. In the terms $\frac{1}{4}\boldsymbol{\nabla}\mathbf{m}\cdot\circ\boldsymbol{\nabla}\mathbf{m}$, both contractions are performed. For meta-GGA, additional Laplacians of the densities are needed. This approach achieves an expected property of the exact functional, namely producing a vanishing global torque while allowing for non-zero local torque. We do not expect computational results to depend strongly on the formalism of non-collinear DFT, but we do note that without proper treatment of the magnetization $\mathbf{m}$ it would be impossible to treat open-shell systems. As this approach has been developed and calibrated, we refer readers to Ref. 105 for mathematical derivations and implementations and Ref.113 for a recent review of non-collinear DFT methods.

The X2C Hamiltonian including non-collinear DFT is expressed as

$$
\begin{aligned}
\mathbf{F}^{\sigma\sigma'} = \mathbf{h}^{\sigma\sigma'} &+ \delta_{\sigma\sigma'}\mathbf{J}(\mathbf{P}^{\alpha\alpha} + \mathbf{P}^{\beta\beta}) - \theta\mathbf{K}(\mathbf{P}^{\sigma\sigma'}) \\
&- (1-\theta)\mathbf{V}_x(\mathbf{P}^{\sigma\sigma'}) + \mathbf{V}_c(\mathbf{P}^{\sigma\sigma'})
\end{aligned}
\tag{3.8}
$$

where σ represents a spin-projection component. The transformed one-electron integrals are contained in $\mathbf{h}$, $\mathbf{J}$ and $\mathbf{K}$ are the Coulomb and exchange integrals, and $\mathbf{V}_x$ and $\mathbf{V}_c$ are the DFT exchange and correlation functionals respectively. The parameter θ is zero for pure DFT and is one for pure HF, with hybrid functionals falling in-between.

3.2.3 Real-time Time-dependent Density Functional Theory

Equation (3.8) gives rise to a spin-blocked Kohn-Sham matrix that enters the Liouville-von Neumann form of the time-dependent Schrödinger equation with a spin-blocked density matrix in an orthonormal basis (the tilde notation refers to quantities in the orthonormal basis) and X2C transformed "picture frame".

$$i\frac{\partial}{\partial t}\begin{pmatrix} \tilde{\mathbf{P}}^{\alpha\alpha}(t) & \tilde{\mathbf{P}}^{\alpha\beta}(t) \\ \tilde{\mathbf{P}}^{\beta\alpha}(t) & \tilde{\mathbf{P}}^{\beta\beta}(t) \end{pmatrix} = \left[\begin{pmatrix} \tilde{\mathbf{F}}^{\alpha\alpha}(t) & \tilde{\mathbf{F}}^{\alpha\beta}(t) \\ \tilde{\mathbf{F}}^{\beta\alpha}(t) & \tilde{\mathbf{F}}^{\beta\beta}(t) \end{pmatrix}, \begin{pmatrix} \tilde{\mathbf{P}}^{\alpha\alpha}(t) & \tilde{\mathbf{P}}^{\alpha\beta}(t) \\ \tilde{\mathbf{P}}^{\beta\alpha}(t) & \tilde{\mathbf{P}}^{\beta\beta}(t) \end{pmatrix}\right] \tag{3.9}$$

In this work, Eq. (3.9) is directly integrated in the time domain and resolve the spectrum of $L_{2,3}$-edges of XAS by tracking the oscillatory behavior of physical properties.[101, 102] This is the real-time relativistic electronic dynamics approach and it is advantageous for many systems (see Ref. 114 for a recent review).

Equation (3.9) can be integrated using the modified mid-point and unitary transformation (MMUT) method.[46, 58, 59, 115] This propagates the density matrix from time t_{n-1} to t_{n+1} by the time evolution operator $\tilde{\mathbf{U}}$ at time t_n:

$$\tilde{\mathbf{P}}(t_{n+1}) = \tilde{\mathbf{U}}(t_n) \cdot \tilde{\mathbf{P}}(t_{n-1}) \cdot \tilde{\mathbf{U}}^{\dagger}(t_n) \tag{3.10}$$

The time evolution operator $\tilde{\mathbf{U}}(t)$ is given by

$$\tilde{\mathbf{U}}(t_n) = \exp[-i \cdot 2\Delta t \cdot \tilde{\mathbf{F}}(t_n)] \tag{3.11}$$

Using the eigenvalues $\epsilon(t_n)$ and eigenvectors $\tilde{\mathbf{C}}(t_n)$ of the Hamiltonian at a specified time t_n, the matrix $\tilde{\mathbf{U}}$ is formed using Eq. (3.12) and Eq. (3.13)

$$\tilde{\mathbf{C}}^{\dagger}(t_n) \cdot \tilde{\mathbf{F}}(t_n) \cdot \tilde{\mathbf{C}}(t_n) = \epsilon(t_n) \tag{3.12}$$

$$\tilde{\mathbf{U}}(t_n) = \tilde{\mathbf{C}}(t_n) \cdot \exp[-i \cdot 2\Delta t \cdot \epsilon] \cdot \tilde{\mathbf{C}}^{\dagger}(t_n) \tag{3.13}$$

The real-time approach can be used to obtain an absorption spectrum by exciting all dipole-allowed electronic transitions with a delta pulse along some direction q. The X2C

Hamiltonian in the AO basis is modified to be

$$\mathbf{F}(t) = \mathbf{F}_0(t) + \sum_{q=x,y,z} \kappa_q(t)\langle r_q \rangle \tag{3.14}$$

where $\mathbf{F}_0$ is the field-free Hamiltonian, $\kappa_q(t)$ is the field strength and $\langle r_q \rangle$ denotes the dipole integrals along direction q.

Because time is discretized, the perturbation corresponds to a step function lineshape lasting for only the initial time-step of width Δt, e.g.

$$\kappa_q(t) = \begin{cases} \kappa_{\max}, & 0 \leq t < \Delta t, \\ 0, & \text{else} \end{cases} \tag{3.15}$$

where $\kappa_{\max}$ is the field strength. The electric dipole field in the X2C equations also requires that the atomic orbital electric dipole integrals be transformed from the four-component framework using the transformation matrix in Eq. (3.3). Failure to do so results in the so-called "picture-change" error [61].

Following this external perturbation, the molecular dipole will evolve in time. The absorption spectrum can then be determined by a Fourier transform of the time-evolving dipole moment. Padé approximants can also be used and have been shown to produce comparable spectra with far shorter simulation time [65]. The transformed dipole moments can then be used to construct the isotropic dipole strength function

$$S(\omega) \propto \sum_{q=x,y,z} \mathrm{Tr}\left[\omega \cdot \mathrm{Im}\frac{\mu_q(\omega)}{\kappa_q}\right] \tag{3.16}$$

to form the absorption spectrum.

Using a technique developed by Bruner et al. [65], we can project the time-evolving density onto the ground state MOs, $\mathbf{C}(0)$. The contributions of different MO pairs can be separated from the time-evolving dipole moment.

$$\mu_{ia}(t) = \sum_{\mu\nu} C^*_{i\mu}(0) d_{\mu\nu} P_{\mu\nu}(t) C_{a\nu} + \sum_{\mu\nu} C^*_{a\mu}(0) d_{\mu\nu} P_{\mu\nu}(t) C_{i\nu} \tag{3.17}$$

where **d** is the dipole matrix in AO basis. With these different quantities, we can determine which orbitals are involved in transitions at a particular frequency. The information is similar to what is contained in the transition vectors obtained from linear response, although the contributions are weighted by the dipole strength for that MO pair, so relative intensities will differ slightly from response theory.

3.3 Computational Details

All molecules used in this study were optimized with unrestricted B3LYP [116, 117] and the cc-pVDZ basis set [118, 119, 120, 121]. Several common functionals and basis sets were then used to resolve L-edge spectra. The B3LYP, BHandHLYP [122], and PBE0 [123, 124] functionals and the aug-cc-pVTZ, def2-TZVPD [125, 126, 127, 128], and Sapporo double-ζ [64] basis sets were used. All real-time simulations were performed in a locally modified copy of the development version of Gaussian [5] and used a time-step of 0.48 as and an initial kick κ_{max} of 0.0001 atomic units. Each propagation was run for at least 10 fs or until the spectrum converged. The dipole signal was transformed with Padé approximants using exponential damping to give a Lorenztian lineshape with a FWHM of 0.75 eV. Inhomogeneous broadenings [129, 50, 130] were not included in this work. The time-evolving dipole was broken down into contributions from the ground-state $2p$ orbitals to simplify the analysis.

There are a number of sources of error in the calculated L-edge spectra. First, the absolute positions of core transition energies are often offset from experimental values. This is commonly attributed to self-interaction errors in DFT [131] and is corrected by shifting the entire core excitation spectrum to match the experimental one. Additionally, there is possible error in using empirical factors for treating two-electron spin-orbit coupling [51]. While the uniform shift will correct the position of one of the edges, if the $2p$ splitting induced by spin-orbit coupling is not correct, then the other edge will still be offset from the experiment. Another approach would be to further shift the L_2 edge to correct for the error in spin-orbit splitting so that each matches with its experimental counterpart. In order to separate errors in relative peak positions from those due to incorrect spin-orbit coupling,

both approaches will be used to analyze the ability of different model chemistries to describe L-edge spectra.

3.4 Results and Discussion

By separating the time-evolving dipole into different MO pairs, contributions from $2p_{1/2}$ and $2p_{3/2}$ orbital sets can be identified. Taking the example of $TiCl_4$, there are two strong features in the spectrum corresponding to the L_3 and L_2 edges (Fig. 3.1). The canonical MOs show a doubly and a quadruply degenerate set of $2p$ orbitals, which we identify as the $2p_{1/2}$ and $2p_{3/2}$ sets. Both $p_{1/2}$- and $p_{3/2}$-dominant orbitals contribute to both L_2 and L_3 peaks due to mixing through ligands. Separating excitations from those two sets shows their respective contributions to the L-edge features. The lower-energy L_3 transitions are dominated by the $2p_{3/2}$ orbitals as expected, but there is also some negative intensity from the $2p_{1/2}$ orbitals as well. Note that this decomposition into MO pairs is a mathematical approach to extract dominant MO contributions to L-edge peaks. In other words, it is a partial trace of the transition dipole moment. Therefore, negative intensities resulted from MO pair transitions that do not correspond to spectroscopic observables. The sum of all MO paired dipoles from the $2p$ orbitals is consistently positive as expected from a genuine observable obtained by using the full density matrix.

The different model chemistries produce very similar results for $TiCl_4$. Figure 3.2 shows that there are two L_3 features around 457 eV and two L_2 features around 462 eV. The splitting between the L_3 and L_2 features is comparable to that of the experiment, which shows that the two-electron spin-orbit coupling correction is performing as intended. In the experiment, the L_3 edge appears more intense than the L_2 edge, but in these calculations the reverse is true. However, the integrated peak areas in both experimental and computed spectra show that the L_2 edge is indeed slightly more intense than L_3, with an L_3:L_2 ratio close to 1:1 [132, 133, 134]. Comparison with other calculations [103, 135] suggesta that there are additional higher-energy quasi-continuum electronic levels that are not fully described. Little variation is seen between the different basis sets for each density functional, except in

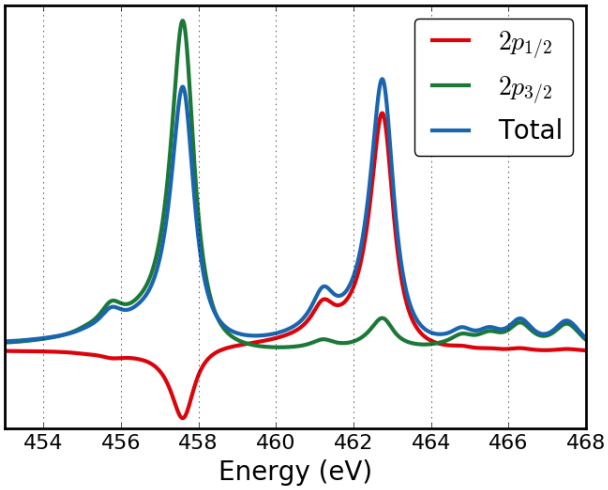

Figure 3.1: $L_{2,3}$ absorption edges for $TiCl_4$ modeled with B3LYP and the aug-cc-pVTZ basis set. The time-evolving dipole was split into different MO pairs and only contributions from the $2p$ orbitals are included.

the higher-energy region of the spectrum. The high-energy peaks correspond to transitions to quasi-continuum states, which are not well described by Gaussian basis sets.

The two features seen for each edge are transitions to the e and t_2 d-orbital sets. The t_2 set is further split due to spin-orbit coupling, but this effect is rather small for such a light transition metal ($< 3 \times 10^{-3}$ eV for $TiCl_4$) [136]. The standard point group labels will be used for simplicity. The relative contributions of transitions to these sets of orbitals are shown in Fig. 3.3. The e set contributes to the lower-energy feature of the L_2 and L_3 edges making up 80.9% and 76.0% of the d-orbital contribution, respectively. Likewise, the higher energy feature is primarily composed of transitions to the t_2 set, with 70.3% and 76.4% of the d-orbital contribution to L_2 and L_3, respectively. Crystal field splitting is highly dependent on the amount of HF exchange in the hybrid functional with larger amounts tending to overestimate d-orbital splitting [137]. B3LYP has 20%, PBE0 has 25%, and BHandHLYP has 50% HF exchange. Consistently in this study, BHandHLYP overestimates the d-orbital

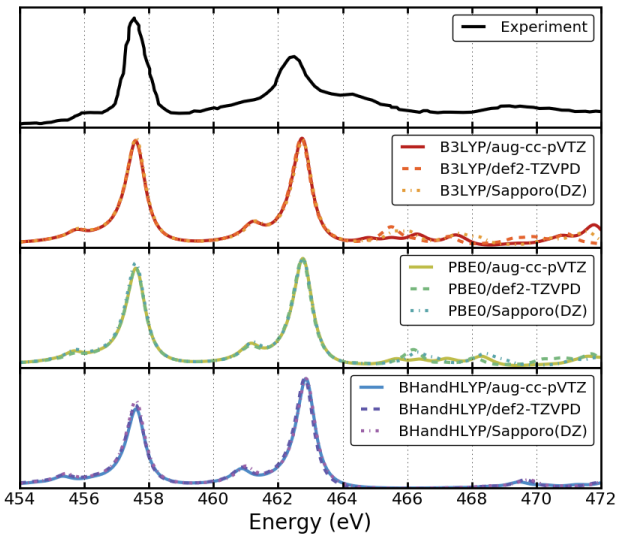

Figure 3.2: Experimental [1] and modeled $L_{2,3}$ absorption edges for $TiCl_4$.

splitting, while the other functionals describe this splitting more accurately.

Despite being a similar molecule with tetrahedral symmetry, the spectrum of $SiCl_4$ contains many more features than $TiCl_4$, as shown in Fig. 3.4. One reason for this is that the core $2p$ orbitals of Si are considerably less localized than Ti in the chloride complex, but instead experience more mixing with the ligand environment. The $L_{2,3}$ spectrum of $SiCl_4$ is complicated by the very small $p_{3/2}$ and $p_{1/2}$ splitting of about 0.5 eV, which leads to both sets of features lying on top of each other, as noted by Bozek et al. [2]. Again we see that the high amount of HF exchange in BHandHLYP leads to a worse overall prediction by overestimating d orbital splitting that pushes the second broad feature too high in energy. Additionally, it is clear that the def2-TZVPD basis set performs qualitatively and quantitatively worse than cc-pVTZ and Sapporo (DZ). The contamination from quasi-continuum excitations is much worse for this basis since it contains fewer total functions.

The L-edge absorption spectrum of CrO_2Cl_2 is similar to that of $TiCl_4$ (Fig. 3.5) but also more complex. There are still two separated L_3 and L_2 segments and the B3LYP and PBE0

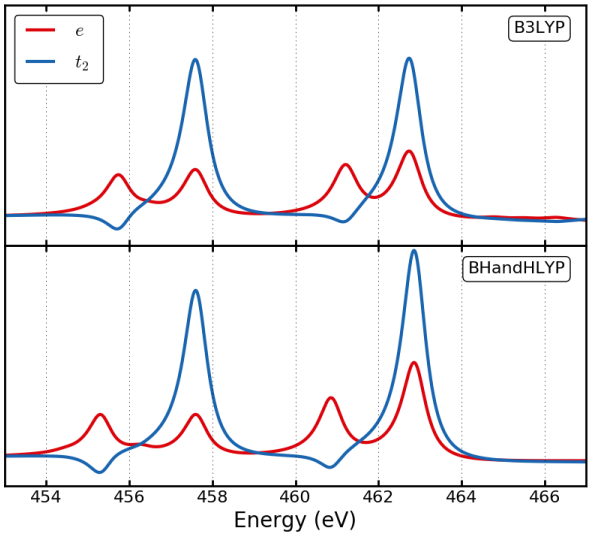

Figure 3.3: Modeled absorption spectrum of $TiCl_4$ split into transitions to the e and t_2 sets of d-orbitals. Modeled with the B3LYP and BHandHLYP functionals using aug-cc-pVTZ basis set.

spectra again look similar except in the very-high-energy region of the spectrum. The $2p_{3/2}$ ionization limit sits right at the end of the L_2 segment, so excitations to quasi-continuum states overlap with the high L_2 transitions and cause the variation seen between the different basis sets. The BHandHLYP spectra are significantly different than the other functions again due to the greater d-orbital splitting caused by the large percentage of HF exchange. This can be confirmed by again separating the contributions from transitions to different sets of d-orbitals. The lower-symmetry C_{2v} environment produces five distinct sets of orbitals responsible for the peaks and shoulders seen in the aggregate spectrum.

The B3LYP and PBE0 spectra of $[FeCl_6]^{3-}$ are very similar as is seen with the other systems and there is also little variation between each basis set. For BHandHLYP, the L_3 feature is split into two peaks unlike the other functionals. It also seems that the relative intensity of these two peaks is reversed for BHandHLYP, with the lower-energy peak having

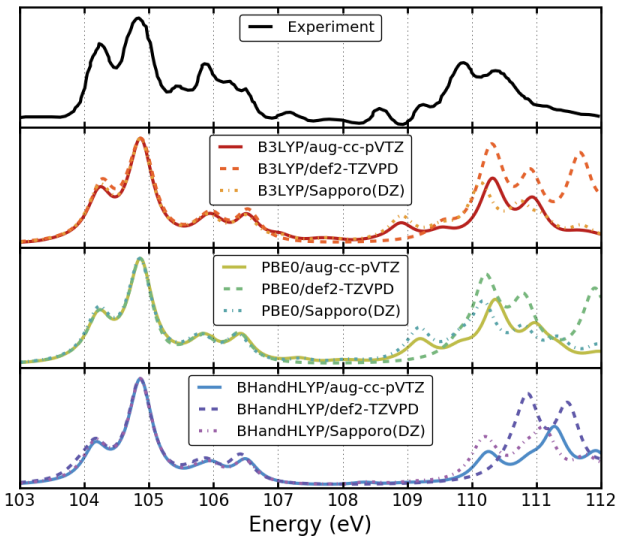

Figure 3.4: Experimental [2] and modeled $L_{2,3}$ absorption edges for $SiCl_4$.

greater intensity than the higher-energy one. This is due to a combination of increased splitting in both the *d* and *p* orbitals from the larger percentage of Hartree-Fock exchange in this high spin, open-shell system. The splitting of L_3 makes it difficult to assign an appropriate shift value based on this feature. We have instead assigned the shifts based on the first L_3 peak instead of the dominant feature as was done with the other molecules.

Again the splitting between many of the features is greater for BHandHLYP than for the other functionals. Uniquely, there are additional features in the experimental spectrum between L_3 and L_2 that are not reproduced in the modeled spectra. These have been attributed to shake-up transitions [4] not well described by single-determinant or single-reference methods [99]. Multiconfigurational approaches have been able to describe them in the past [97].

Spin-orbit coupling splitting is slightly overestimated for $TiCl_4$ and is underestimated for CrO_2Cl_2 and $[FeCl_6]^{3-}$. The error is fairly small (5.7–7.1% for these systems) and is in line with the expected ∼6% error using Boettger's empirical correction [51]. The error in predicted spin-orbit splitting for $SiCl_4$ is much smaller, with less than 2% relative error. For

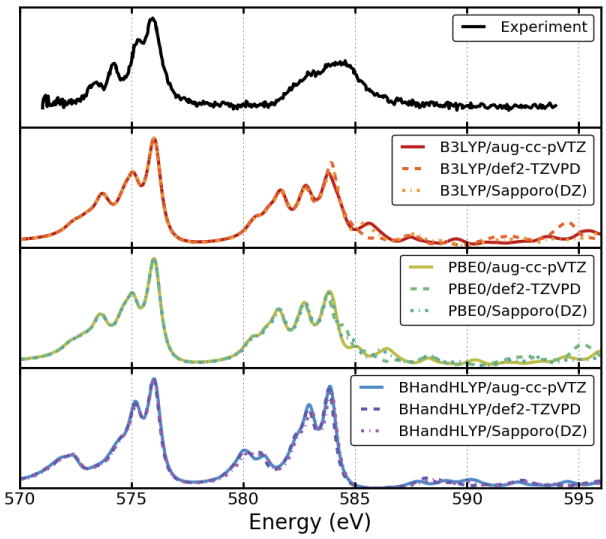

Figure 3.5: Experimental [3] and modeled $L_{2,3}$ absorption edges for CrO_2Cl_2.

heavier elements, the spin-orbit coupling splittings should be much larger, so that 6% error will be several eV. To correct for this error arising from the empirical Boettger's factor, one can apply an additional shift to the L_2-L_3 splitting to match experimental values. Errors using both of these scenarios (with and without spin-orbit-corrected shift) are presented in Tab. 3.1. The mean absolute errors (MAE) for different features for the four molecules presented herein and the overall spread of the errors are reported.

The errors seen for the different model chemistries are most strongly dependent upon the choice of density functional as evident in the spectra above. Using the additional spin-orbit-corrected shift results in lower mean absolute error for the model chemistries using B3LYP and PBE0. The range of the errors is also significantly reduced for B3LYP and PBE0. This is not true for BHandHLYP, indicating that it does a poorer job describing the orbitals involved in these L-edge transitions. We also note that there is a large dependence on the basis set with the BHandHLYP functional, while B3LYP and PBE0 are much less sensitive. For these reasons, BHandHLYP is not an appropriate functional to use for any of

		Self-interaction-corrected Shift		Self-interaction-corrected and spin-orbit-corrected Shift	
		MAE	Range	MAE	Range
B3LYP	aug-cc-pVTZ	0.38	0.98	0.26	0.56
	def2-TZVPD	0.38	0.94	0.23	0.56
	Sapporo(DZ)	0.35	0.96	0.21	0.46
BHandHLYP	aug-cc-pVTZ	0.47	1.88	0.51	1.88
	def2-TZVPD	0.42	1.12	0.44	1.08
	Sapporo(DZ)	0.32	0.76	0.32	0.76
PBE0	aug-cc-pVTZ	0.39	0.82	0.25	0.57
	def2-TZVPD	0.37	0.89	0.24	0.40
	Sapporo(DZ)	0.36	0.87	0.24	0.45

Table 3.1: Mean absolute errors (MAE) and the range of errors in eV for several different functional and basis set combinations. Errors for the L_3 and L_2 edges shifted with and without the additional spin-orbit-corrected shift are reported.

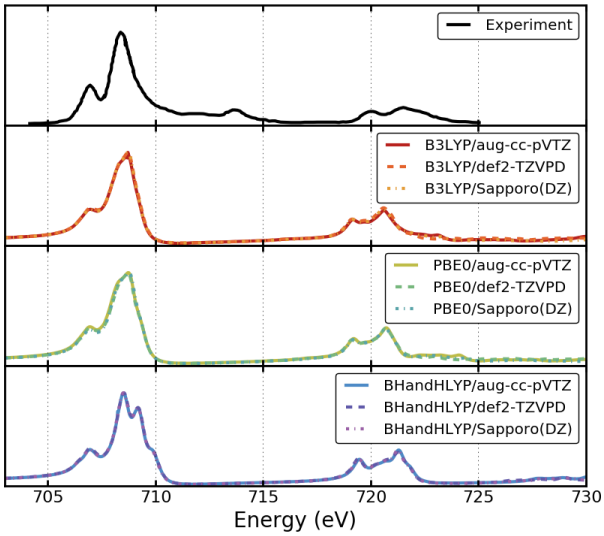

Figure 3.6: Experimental [4] and modeled $L_{2,3}$ absorption edges for $[FeCl_6]^{3-}$.

these systems, but both PBE0 and B3LYP performed equally well.

3.5 Conclusions

In this work we have demonstrated calculations of $L_{2,3}$-edge absorption spectra using the two-component RT-X2C-TDDFT method. The method is general for both closed- and open-shell systems and allows the entire absorption spectrum to be computed at once. One-electron spin-orbit coupling is variationally included in the Hamiltonian along with a correction term to account for the neglect of two-electron spin-orbit terms. This leads to ∼6% error in the splitting of the $2p_{1/2}$ and $2p_{3/2}$ orbitals and an error in the spacing between the L_2 and L_3 edges. Core excitation spectra are typically shifted to match with the experimental spectrum and an additional shift can be applied to account for the error arising from the the empirical Boettger's treatment of one-electron spin-orbit coupling.

Spectra modeled with B3LYP and PBE0 agree well with experiment, but spectra from BHandHLYP tend to overestimate *d*-orbital splitting. This is due to the comparable amounts

of HF exchange in B3LYP and PBE0 and the large amount in BHandHLYP. Results from a particular functional are relatively insensitive to the choice of basis set, except in the quasi-continuum regime, although we note that smaller basis sets such as def2-TZVPD may not be sufficient. Using the time-dependent MO pair contributions to the density, an analysis of the molecular orbitals involved in the transitions can also be obtained, yielding valuable theoretical information that can be used to connect the local electronic structure with the experimental observables.

Chapter 4

A WELL-TEMPERED HYBRID METHOD OF DAVIDSON AND GPLHR FOR SOLVING CHALLENGING TDDFT SYSTEMS

The time-dependent Hartree-Fock (TDHF) and time-dependent density functional theory (TDDFT) equations allow one to probe electronic resonances of a system quickly and cheaply. However, the iterative solution of the eigenvalue problem can be challenging or impossible to converge with standard methods such as the Davidson algorithm for spectrally dense regions in the interior of the spectrum as are common in X-ray absorption spectroscopy (XAS). More robust solvers such as the generalized preconditioned locally harmonic residual (GPLHR) [138] method can alleviate this problem, but at the expense of higher average computational cost. A hybrid method is proposed which adapts to the problem in order to maximize computational performance while providing the superior convergence of GPLHR. Additionally, a modification to the GPLHR algorithm is proposed to adaptively choose the shift parameter to enforce convergence of states above a predefined energy threshold. The work in this section is adapted with permission from Joseph M. Kasper, David B. Williams-Young, Eugene Vecharynski, Chao Yang, and Xiaosong Li, *J. Chem. Theory Comput.*, (**2018**), *14 (4)*, 2034-2041. Copyright 2018 American Chemical Society.

4.1 Introduction

The computation of electronic excited states plays a very important role in understanding the response of molecular and material systems to external electromagnetic perturbations. The linear-response time-dependent density functional theory (LR-TDDFT) [139, 140, 141] is one of the most popular methods for this purpose due to its excellent balance between accuracy

and computational cost. Although LR-TDDFT is among the most tractable methods for excited-state calculations, it still leverages a large computational demand for large molecular systems such as those of photochemical interest. The computational cost of solving the TDDFT equations using iterative techniques, such as the Davidson algorithm [142, 143, 144], formally scales as $\mathcal{O}(MN^4)$, where N is the total number of basis functions and M is the number of excited states sought. With the development of efficient linear-scaling methods for direct formation of Fock/Kohn-Sham-like operators, the scaling of conventional implementations of LR-TDDFT may be reduced to $\mathcal{O}(MN^2) - \mathcal{O}(MN^3)$ in complexity [145]. While efficient implementations of LR-TDDFT [146, 147, 148] are routinely used to to obtain characteristics of lowest-lying molecular excited states, modifications to the Davidson algorithm such as restricted excitation windowing [86, 88, 149] or energy-specific windowing [79, 87] have also been used to resolve the spectral interior of the LR-TDDFT equation, which is crucial to modeling K-edge X-ray absorption spectroscopy (XAS).

However, for systems that exhibit a dense manifold of excited states in the spectral region of interest, e.g. carbon K-edge XAS of a nano-graphene or a nano-diamond, solving the LR-TDDFT equations by iterative diagonalization is still very expensive and subject to nontrivial convergence problems. While alternatives to diagonalization have also been explored, including frequency-dependent response [94, 95, 150, 151, 152, 153, 154, 155] and model order reduction [89, 156], the eigenvector approach provides easy interpretation in the context of electronic adiabats [157] Recently, more robust methods have been proposed for non-Hermitian eigenvalue problems such as the generalized preconditioned locally harmonic residual (GPLHR) algorithm [138]. This solver can reliably converge the closest N roots to a specified spectral shift for arbitrary complex matrices. Its use in chemistry has proven to be effective for EOM-CCSD calculations, although an increased average computational cost over the Davidson algorithm is traded for improved convergence characteristics [158].

In this work, we introduce a modified energy-specific GPLHR method and a well-tempered hybrid method of Davidson and GPLHR methods for solving challenging TDDFT systems. This method takes advantage of the benefits of different iterative diagonalizers, using a

hybrid scheme incorporating an adaptive switching between both energy-specific Davidson and GPLHR. We report the results on a variety of test systems in the very challenging high-energy X-ray region with dense manifolds of excited states. In addition to providing additional robustness of convergence for systems for which Davidson fails, we find that there are systems where a hybrid approach is able to computationally beat either method alone.

4.2 Theory

As the formalism of the linear-response TDHF/TDDFT is a well-established method, we only present a brief review herein. For a detailed discussion, we refer the interested reader to Ref. 148. The linear response of a molecular system subject to perturbation by an external electromagnetic field is given by the TDHF or TDDFT equations

$$\begin{pmatrix} \mathbf{A} & \mathbf{B} \\ \mathbf{B}^* & \mathbf{A}^* \end{pmatrix} \begin{pmatrix} \mathbf{X} \\ \mathbf{Y} \end{pmatrix} = E \begin{pmatrix} 1 & 0 \\ 0 & -1 \end{pmatrix} \begin{pmatrix} \mathbf{X} \\ \mathbf{Y} \end{pmatrix} \tag{4.1}$$

where the matrices $\mathbf{A}$ and $\mathbf{B}$ for TDHF are defined as

$$A_{ai,bj} = \delta_{ab}\delta_{ij}(\epsilon_a - \epsilon_i) + (ia|jb) - (ib|ja) \tag{4.2}$$

$$B_{ai,bj} = (ia|bj) - (ij|ba) \tag{4.3}$$

and for TDDFT as

$$A_{ai,bj} = \delta_{ab}\delta_{ij}(\epsilon_a - \epsilon_i) + (ia|jb) - \alpha(ib|ja) + (ia|f_{xc}|jb) \tag{4.4}$$

$$B_{ai,bj} = (ia|bj) - \alpha(ij|ba) + (ia|f_{xc}|bj) \tag{4.5}$$

The two-electron integrals have been expressed in the canonical molecular orbital (MO) basis in Mulliken notation where i and j indices are used for occupied MOs and a and b indices for virtual MOs, ϵ_p is the orbital energy of the Kohn–Sham operator for MO p, and α is a real scaling parameter such that, for pure DFT kernels $\alpha = 0$, while for hybrid DFT the scaling factor α determines the fraction of Hartree-Fock exchange to be included. The eigensystem of Eq. (4.1) describes the electronic adiabatic states of the molecular system

with the eigenvalues corresponding to the electronic resonances (excitation energies) of the system, while the corresponding eigenvectors describe the orbital excitation and de-excitation amplitudes for the adiabat. In the case of real-valued matrices, $\mathbf{A}^* = \mathbf{A}$ and $\mathbf{B}^* = \mathbf{B}$, so one can also solve the equivalent problem of half the dimension [143, 146, 159]:

$$(\mathbf{A} - \mathbf{B})(\mathbf{A} + \mathbf{B})|\mathbf{X} + \mathbf{Y}\rangle = \omega^2|\mathbf{X} + \mathbf{Y}\rangle \tag{4.6}$$

4.2.1 Davidson-like methods

For many systems of chemical interest, the dimension of the matrices is far too large to store in memory for full diagonalization and must be partially diagonalized by iterative methods. One of the most well-known methods for iterative diagonalization of the CIS equations was proposed by Davidson in 1975 [142]. Modifications have allowed it to be extended to the RPA equations [143, 144, 146, 160], as well as providing restricted excitation [86, 88, 149] or energy specific windowing [79, 87] to obtain higher-energy roots. The following is a basic overview of the energy-specific algorithm used here, but for a detailed implementation of the Davidson algorithm for solving the RPA equations, we invite the reader to see Refs. 87 or 161.

The basic idea of the Davidson algorithm is to work in a much smaller reduced dimensional search space and find the best approximate (right) eigenvectors for Eq. (4.6) as a linear combination of basis vectors $|\mathbf{b}_i\rangle$:

$$|\mathbf{X}_j + \mathbf{Y}_j\rangle = \sum_{i=1}^{m} c_{ij}|\mathbf{b}_i\rangle \tag{4.7}$$

where the coefficients c_{ij} are found by diagonalization of the subspace problem. To do this the action of the $(\mathbf{A} + \mathbf{B})$ and $(\mathbf{A} - \mathbf{B})$ matrices on the $\mathbf{b}_i$ vectors is calculated directly. Stratmann *et al.* [146] then noted that in the limit of convergence $\langle\mathbf{b}_i|(\mathbf{A} - \mathbf{B})(\mathbf{A} + \mathbf{B})|\mathbf{b}_j\rangle$ will have the same solutions as

$$\tilde{M}_{ij} = \sum_k \langle\mathbf{b}_i|\mathbf{A} - \mathbf{B}|\mathbf{b}_k\rangle\langle\mathbf{b}_k|\mathbf{A} + \mathbf{B}|\mathbf{b}_j\rangle \tag{4.8}$$

This non-Hermitian matrix product is diagonalized to determine the best approximate right and left eigenvectors $|\tilde{\mathbf{R}}\rangle$, $|\tilde{\mathbf{L}}\rangle$, and the corresponding eigenvalues $\tilde{\boldsymbol{\omega}}$ in the subspace. The eigenvectors contain the coefficients to transform $|\tilde{\mathbf{R}}\rangle$ and $|\tilde{\mathbf{L}}\rangle$ from the reduced space to the full MO space ($|\mathbf{R}\rangle$, $|\mathbf{L}\rangle$). In the energy-specific case, we choose to transform the first n eigenvectors with $\tilde{\omega}_i \geq \omega_0$, where ω_0 is the energy threshold. Otherwise, one can take $\omega_0 = 0$ and transform the n lowest-energy roots.

To determine if the approximation is good enough, the left and right components of the residual vectors $|\mathbf{W}_n\rangle$ are given by

$$|\mathbf{W}_n^L\rangle = (\mathbf{A} + \mathbf{B})|\mathbf{R}_n\rangle - \tilde{\omega}_n|\mathbf{L}_n\rangle \tag{4.9}$$

and

$$|\mathbf{W}_n^R\rangle = (\mathbf{A} - \mathbf{B})|\mathbf{L}_n\rangle - \tilde{\omega}_n|\mathbf{R}_n\rangle \tag{4.10}$$

If the residuals are non-zero, new vectors are constructed and added to the subspace. While the residual vectors could be added to the set of $|\mathbf{b}_i\rangle$ without further modification, it is more efficient to use a preconditioner to achieve quasi second-order information. Since the left-hand side of Eq. (4.1) is diagonally dominant with the orbital energy differences, the preconditioned residual vectors are given by

$$Q_{in} = (\tilde{\omega}_n - \Delta\epsilon)^{-1} W_{in} \tag{4.11}$$

Here, the $\Delta\epsilon$ are the orbital energy differences along the diagonal of $\mathbf{A}$. These $\mathbf{Q}$ vectors are added to the set of existing $\mathbf{b}$ and the entire process is repeated until the norm of the residuals falls below a specified threshold (or equivalently that $\tilde{\omega}_i$ stop changing) and convergence is achieved. As the number of basis vectors $\mathbf{b}_i$ approaches the full dimension of the matrix, the approximation much approach the exact solution. However, it is also possible that the number of $\mathbf{b}_i$ grows very large before convergence, in which case the algorithm can be restarted by collapsing the subspace down to a small number of vectors using the best $|\mathbf{R}\rangle$ and $|\mathbf{L}\rangle$.

4.2.2 The GPLHR Method for Obtaining High-Energy Excited States

The GPLHR algorithm is a recently proposed method [138] to iteratively solve the generalized eigenvalue problem for arbitrary non-Hermitian square matrices $\boldsymbol{\mathcal{H}}$ and $\boldsymbol{\mathcal{M}}$:

$$\boldsymbol{\mathcal{H}}|\mathbf{x}\rangle = \omega\boldsymbol{\mathcal{M}}|\mathbf{x}\rangle \tag{4.12}$$

Note that in the context of Eq. (4.1), $\boldsymbol{\mathcal{H}}$ and $\boldsymbol{\mathcal{M}}$ are represented here in the full-dimension and not the half-dimension problem in Eq. (4.6), as are all other quantities in calligraphic script.

In particular, GPLHR aims to improve the convergence and performance of iterative diagonalization for a targeted region in the interior of the spectrum. That is, given some target shift σ, GPLHR attempts to find the n eigenvalues ω_i closest to σ along with the associated eigenvectors $|\mathbf{x}_i\rangle$. We also note here that, unlike the strict lower-bound ω_0 used in energy-specific Davidson, we obtain the closest values to σ both above *and* below.

An excellent technical report of the GPLHR algorithm is published elsewhere [138], to which we refer interested readers. Here we provide an overview of the salient points to facilitate comparison with the Davidson and the Lanczos family of algorithms as well as how these two methods can complement each other in an adaptive hybrid scheme for the TDHF/TDDFT problem.

First, given some set of orthonormalized initial guess (right) vectors $\boldsymbol{\mathcal{V}}$, we form the set of vectors $\boldsymbol{\mathcal{Q}}$ in the σ-shifted space according to

$$\boldsymbol{\mathcal{Q}} = (\boldsymbol{\mathcal{H}} - \sigma\boldsymbol{\mathcal{M}})\boldsymbol{\mathcal{V}} \tag{4.13}$$

followed by orthonormalization. The generalized eigenproblem for the pair

$$(\boldsymbol{\mathcal{Q}}^\dagger\boldsymbol{\mathcal{H}}\boldsymbol{\mathcal{V}}, \boldsymbol{\mathcal{Q}}^\dagger\boldsymbol{\mathcal{M}}\boldsymbol{\mathcal{V}}) \tag{4.14}$$

is given by

$$\boldsymbol{\mathcal{Q}}^\dagger\boldsymbol{\mathcal{H}}\boldsymbol{\mathcal{V}}\,|x_i\rangle = \tilde{\omega}_i\boldsymbol{\mathcal{Q}}^\dagger\boldsymbol{\mathcal{M}}\boldsymbol{\mathcal{V}}\,|x_i\rangle \tag{4.15}$$

and can then be solved to obtain initial approximations for $\tilde{\omega}_i$. Since $\boldsymbol{\mathcal{Q}}$ is in the σ-shifted space we obtain better approximate $\tilde{\omega}_i$ near σ through the harmonic Rayleigh-Ritz procedure.

Although Eq. (4.14) can be solved by diagonalization based methods, we instead use generalized Schur decomposition (also known as QZ factorization), which has the advantage of being well-defined for any two matrices. From the Schur decomposition of Eq. (4.14) we obtain the triangular factors $\boldsymbol{\mathcal{R}}_1$, $\boldsymbol{\mathcal{R}}_2$, as well as Schur bases $\boldsymbol{\mathcal{Y}}_L$, $\boldsymbol{\mathcal{Y}}_R$ such that

$$\boldsymbol{\mathcal{Q}}^\dagger \boldsymbol{\mathcal{H}} \boldsymbol{\mathcal{V}} = \boldsymbol{\mathcal{Y}}_L \boldsymbol{\mathcal{R}}_1 \boldsymbol{\mathcal{Y}}_R \tag{4.16}$$

and

$$\boldsymbol{\mathcal{Q}}^\dagger \boldsymbol{\mathcal{M}} \boldsymbol{\mathcal{V}} = \boldsymbol{\mathcal{Y}}_L \boldsymbol{\mathcal{R}}_2 \boldsymbol{\mathcal{Y}}_R \tag{4.17}$$

The eigenvalues are given by the ratio of the diagonal elements of the triangular factors:

$$\omega_j = \boldsymbol{\mathcal{R}}_1(j,j)/\boldsymbol{\mathcal{R}}_2(j,j) \tag{4.18}$$

The Schur vectors $\boldsymbol{\mathcal{Y}}_L$ and $\boldsymbol{\mathcal{Y}}_R$ can be used to update $\boldsymbol{\mathcal{V}}$ and $\boldsymbol{\mathcal{Q}}$, with $\boldsymbol{\mathcal{V}} \rightarrow \boldsymbol{\mathcal{V}}\boldsymbol{\mathcal{Y}}_R$ and $\boldsymbol{\mathcal{Q}} \rightarrow \boldsymbol{\mathcal{Q}}\boldsymbol{\mathcal{Y}}_L$. More importantly, we can use the information in the triangular factors in the process of generating new vectors to form a new test subspace and generalized eigenproblem.

In contrast to the Davidson algorithm, in which the subspace grows at each iteration, GPLHR generates a subspace of fixed size based on an integer parameter m. This is used to update the current solution $\boldsymbol{\mathcal{V}}$, but is discarded and not reused on subsequent iterations. This trial subspace $\boldsymbol{\mathcal{Z}} = [\boldsymbol{\mathcal{V}}, \boldsymbol{\mathcal{W}}, \boldsymbol{\mathcal{S}}_1, ..., \boldsymbol{\mathcal{S}}_m, \boldsymbol{\mathcal{P}}]$ corresponds to the Krylov-Arnoldi sequence generated by the preconditioned residuals and is constructed as shown in Algorithm 1.

$\boldsymbol{\mathcal{P}}$ is an additional block of saved vectors and is not used on the first iteration. The matrices $\boldsymbol{\mathcal{G}}_1$ and $\boldsymbol{\mathcal{G}}_2$ are diagonal and constructed from the triangular factors $\boldsymbol{\mathcal{R}}_1$ and $\boldsymbol{\mathcal{R}}_2$ as follows:

$$\boldsymbol{\mathcal{G}}_1(j,j) = \begin{cases} 0, & |\boldsymbol{\mathcal{R}}_1(j,j)| < |\boldsymbol{\mathcal{R}}_2(j,j)| \\ \frac{1-\boldsymbol{\mathcal{R}}_2(j,j)}{\boldsymbol{\mathcal{R}}_1(j,j)}, & \text{otherwise} \end{cases} \tag{4.19}$$

Algorithm 1: Generation of Trial Subspace

Input : Vectors $\mathcal{V}$, Schur factors $\mathcal{R}_1$, $\mathcal{R}_2$, preconditioner $\mathcal{T}$, and approximate eigenvalues $\tilde{\omega}$

Output: Krylov-Arnoldi sequence $[\mathcal{W}, \mathcal{S}_1, ..., \mathcal{S}_m]$

Form diagonal matrices $\mathcal{G}_1$ and $\mathcal{G}_2$ by Eq. (4.19) and Eq. (4.20)

$\mathcal{G} \leftarrow \mathcal{R}_1\mathcal{G}_1 + \mathcal{R}_2\mathcal{G}_2$

$\mathcal{B}_1 \leftarrow \mathcal{G}_2\mathcal{G}^{-1}\mathcal{R}_1; \mathcal{B}_2 \leftarrow \mathcal{I} - \mathcal{G}_1\mathcal{G}^{-1}\mathcal{R}_1$

$\mathcal{W} \leftarrow (\mathcal{I} - \mathcal{V}\mathcal{V}^\dagger)\mathcal{T}(\mathcal{I} - \mathcal{Q}\mathcal{Q}^\dagger)(\mathcal{H}\mathcal{V}\mathcal{B}_2 - \mathcal{M}\mathcal{V}\mathcal{B}_1)$

Set $\mathcal{S}_0 \leftarrow \mathcal{W}$

for $l =, 1, \ldots, m$ **do**

  $\mathcal{S}_l \leftarrow (\mathcal{I} - \mathcal{V}\mathcal{V}^\dagger)\mathcal{T}(\mathcal{I} - \mathcal{Q}\mathcal{Q}^\dagger)(\mathcal{H}\mathcal{S}_{l-1}\mathcal{B}_2 - \mathcal{M}\mathcal{S}_{l-1}\mathcal{B}_1)$

end

$$\boldsymbol{\mathcal{G}}_2(j,j) = \begin{cases} \frac{1}{\boldsymbol{\mathcal{R}}_2(j,j)}, & |\boldsymbol{\mathcal{R}}_1(j,j)| < |\boldsymbol{\mathcal{R}}_2(j,j)| \\ 1, & \text{otherwise} \end{cases} \tag{4.20}$$

For the preconditioner $\mathcal{T}$ we use the inverse of the difference between the approximate eigenvalue $\tilde{\omega}$ and the diagonal elements of $\boldsymbol{\mathcal{H}}$, which are given by the orbital energy differences.

From the trial space $\boldsymbol{\mathcal{Z}}$ the analogous set of vectors in the σ-shifted test space is formed:

$$\boldsymbol{\mathcal{U}} = (\boldsymbol{\mathcal{H}} - \sigma\boldsymbol{\mathcal{M}})\boldsymbol{\mathcal{Z}} \tag{4.21}$$

Again we can solve the reduced-dimensional generalized eigenvalue problem of the pair ($\boldsymbol{\mathcal{U}}^\dagger\boldsymbol{\mathcal{H}}\boldsymbol{\mathcal{Z}}$,$\boldsymbol{\mathcal{U}}^\dagger\boldsymbol{\mathcal{M}}\boldsymbol{\mathcal{Z}}$),

$$\boldsymbol{\mathcal{U}}^\dagger\boldsymbol{\mathcal{H}}\boldsymbol{\mathcal{Z}}\,|x_i\rangle = \tilde{\omega}_i\boldsymbol{\mathcal{U}}^\dagger\boldsymbol{\mathcal{M}}\boldsymbol{\mathcal{Z}}\,|x_i\rangle \tag{4.22}$$

by generalized Schur decomposition, noting that the obtained $\tilde{\omega}_i$ are significantly improved in the region of the eigenspectrum near σ. This yields new factors $\tilde{\boldsymbol{\mathcal{R}}}_1$, $\tilde{\boldsymbol{\mathcal{R}}}_2$, as well as Schur bases $\tilde{\boldsymbol{\mathcal{Y}}}_L$, $\tilde{\boldsymbol{\mathcal{Y}}}_R$. Since the dimension of the eigenproblem in Eq. (4.21) is larger than the

number of roots we seek, the eigenvalue-eigenvector pairs are ordered by closeness to the shift value σ using the standard norm of a complex number given by

$$|(a+bi)| = a^2 + b^2 \tag{4.23}$$

At this step it is important to note that the sorting procedure also requires recomputing the factors $\tilde{\boldsymbol{\mathcal{R}}}_1$, $\tilde{\boldsymbol{\mathcal{R}}}_2$, $\tilde{\boldsymbol{\mathcal{Y}}}_L$, and $\tilde{\boldsymbol{\mathcal{Y}}}_R$. The matrices $\tilde{\boldsymbol{\mathcal{R}}}_1$ and $\tilde{\boldsymbol{\mathcal{R}}}_2$ are then truncated to the first n columns and n rows to form a new $\boldsymbol{\mathcal{R}}_1$ and $\boldsymbol{\mathcal{R}}_2$. Now we can construct new $\boldsymbol{\mathcal{V}}$, $\boldsymbol{\mathcal{Q}}$ from the left and right Schur bases as

$$\boldsymbol{\mathcal{V}} = \boldsymbol{\mathcal{Z}}\tilde{\boldsymbol{\mathcal{Y}}}_R \qquad \text{with } \tilde{\boldsymbol{\mathcal{Y}}}_R \text{ truncated to the first } n \text{ vectors} \tag{4.24}$$

$$\boldsymbol{\mathcal{Q}} = \boldsymbol{\mathcal{U}}\tilde{\boldsymbol{\mathcal{Y}}}_L \qquad \text{with } \tilde{\boldsymbol{\mathcal{Y}}}_L \text{ truncated to the first } n \text{ vectors} \tag{4.25}$$

Additionally we can store the second set of n vectors Eq. (4.24) in $\boldsymbol{\mathcal{P}}$, to be used on subsequent iterations:

$$\boldsymbol{\mathcal{P}} = \boldsymbol{\mathcal{Z}}\tilde{\boldsymbol{\mathcal{Y}}}_R \qquad \text{with } \tilde{\boldsymbol{\mathcal{Y}}}_R \text{ truncated to vectors } n+1 \text{ to } 2n \tag{4.26}$$

We evaluate convergence of eigenvectors and continue iterations if necessary. Note that the residual of a trial eigenvector $\mathcal{V}_i$ is given by

$$\boldsymbol{\mathcal{H}}\mathcal{V}_i - \tilde{\omega}_i \boldsymbol{\mathcal{M}}\mathcal{V}_i \tag{4.27}$$

These residuals are exactly the vectors calculated in the $\boldsymbol{\mathcal{W}}$ block before preconditioning. In addition to evaluating the norm of the residual vector, we also consider a root converged if the change in the eigenvalue is below some (generally lower) threshold.

One interesting property of the Davidson algorithm with energy-specific windowing that is not present in GPLHR, however, is the ability to set a hard energy-cutoff for converged roots. This is often useful to build up a spectrum from multiple calculations on smaller numbers of roots. While basis deflation can also be used to augment the number of vectors[138], instead of obtaining solutions with energy *greater* than the specified value σ, the solutions could, in principle, all be *less* than σ. Instead one can also adaptively choose σ such that the n closest vectors are all above the cutoff.

More concretely, if the hard threshold is d, then suppose we start with $\sigma = d$ and let $\omega_1, ..., \omega_n$ be the first n Ritz values with $\omega_i > d$ and ω_0 be the Ritz value closest to σ such that $\omega_0 < d$. Ideally one should keep σ as close to d as possible to prevent missing any roots. Intuitively we move σ just far enough to exclude the first Ritz value that is below our chosen threshold as depicted in Fig. 4.1. That is, calculate the midpoint m of ω_n and ω_0 and use this m as the new σ' if $m > d$, otherwise let $\sigma' = d$. Note that σ is never less than d.

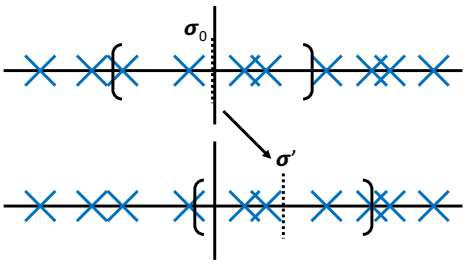

Figure 4.1: Scheme for adaptive choice of shift value σ. Given some set of Ritz values, we may choose a new σ' to maximize convergence for the first n vectors above a threshold d.

4.2.3 An Adaptive Davidson/GPLHR Hybrid Algorithm

The motivation for an adaptive diagonalization algorithm may be best described in analogy to similar techniques used for the SCF procedure and geometry optimization. Quadratically convergent SCF is often too expensive to be used as a method of first choice, but may be employed as a complement to first-order SCF methods on an as–needed basis. Likewise, previous work has found that using a combination of methods for molecular geometry optimization can lead to superior performance [162]. In this work, the development of a hybrid Davidson/GPLHR algorithm is motivated by two considerations: performance and robustness. As mentioned previously, on average the computational cost of Davidson-like algorithms are less than GPLHR [158]. While the Davidson method provides symmetrized

trial vectors that lead to optimal performance in in exploring the selected subspace, in the non-Hermitian case it is possible for the generalized eigenvalue problem to have complex eigenvalues which leads to a loss of monotonic convergence [161]. Poor approximations in the $\tilde{\omega}_i$ also leads to the generation of new vectors that have little overlap with the true solutions. Without reasonable approximations to the correct eigenvalues, the new vectors generated to augment the subspace are of little value. This is especially common for dense manifolds of states, such as those appear in the higher energy X-ray of condensed matter.

On the other hand, GPLHR uses a harmonic Rayleigh-Ritz procedure to locate the eigenvectors with eigenvalues closest to a specified value σ. More stable convergence is also achieved by transferring additional information about subspace search directions from a block of extra Schur vectors, in contrast to the search direction employed by other methods such as LOBPCG [163]. Despite the algorithmic similarities, GPLHR changes the subspace vectors at each iteration and evaluates their quality systematically by solving the problem in the σ-shifted space. This is in contrast to the Davidson-like procedure where poor information is not discarded.

In order to switch between the half-dimensional space of Eq. (4.6) being used for Davidson and the full space in Eq. (4.1) one can take linear combinations of the left $|\mathbf{L}\rangle = |\mathbf{X}-\mathbf{Y}\rangle$ and right $|\mathbf{R}\rangle = |\mathbf{X}+\mathbf{Y}\rangle$ eigenvectors to obtain the $\mathbf{X}$ and the $\mathbf{Y}$ components for some vector $\mathcal{V}$. These vectors are used as the initial "guess" for the GPLHR method. From Eq. (4.1) we compute the matrix-vector product for a given trial vector $\begin{pmatrix}\mathbf{X}_i\\ \mathbf{Y}_i\end{pmatrix}$ as

$$\begin{pmatrix}\mathbf{A}\mathbf{X}_i + \mathbf{B}\mathbf{Y}_i\\ \mathbf{B}\mathbf{X}_i + \mathbf{A}\mathbf{Y}_i\end{pmatrix} \tag{4.28}$$

where we have assumed real orbitals so that $\mathbf{A}^* = \mathbf{A}$ and $\mathbf{B}^* = \mathbf{B}$. It is easy to show that

$$\mathbf{A}\mathbf{X}_i + \mathbf{B}\mathbf{Y}_i = 1/2[(\mathbf{A}+\mathbf{B})(\mathbf{X}_i+\mathbf{Y}_i) + (\mathbf{A}-\mathbf{B})(\mathbf{X}_i-\mathbf{Y}_i)] \tag{4.29}$$

and

$$\mathbf{B}\mathbf{X}_i + \mathbf{A}\mathbf{Y}_i = 1/2[(\mathbf{A}+\mathbf{B})(\mathbf{X}_i+\mathbf{Y}_i) - (\mathbf{A}-\mathbf{B})(\mathbf{X}_i-\mathbf{Y}_i)] \tag{4.30}$$

Construction of the matrix-vector products $(\mathbf{A}+\mathbf{B})(\mathbf{X}+\mathbf{Y})$ and $(\mathbf{A}-\mathbf{B})(\mathbf{X}-\mathbf{Y})$ is accomplished by direct contraction using the same algorithms as have been used for the Davidson method.

The key question for the adaptive scheme is deciding when to switch from Davidson to GPLHR. One option is to let Davidson run for a set number of iterations and switch if not converged. Similarly, we could switch when the subspace becomes too large and Davidson is forced to restart. These are simple to implement and account for at least some situations where convergence was hard. A more systematic option is to analyze the convergence behavior itself to decide when subsequent iterations and generated vectors are unlikely to be useful. To do this we can consider several error metrics. For eigenvalues, we expect the difference in consecutive iterations to go to zero and calculate the norm of the difference vector at iteration i:

$$\delta_i = \left\| \begin{pmatrix} \Delta\omega_1 \\ \vdots \\ \Delta\omega_n \end{pmatrix} \right\| \tag{4.31}$$

The sequence of $\{\delta_i\}$ should be decreasing as we get closer to convergence and provides an overall measure of how close all n roots are to convergence. Note that this also depends on the quality of the mapping of roots from one iteration to the next. Likewise, for eigenvectors, we expect the residuals under the action of the RPA matrix to go to zero.

$$r_i = \|(\mathbf{H} - \mathbf{\Omega}\mathbf{M})\boldsymbol{\mathcal{V}}\| \tag{4.32}$$

This sequence of $\{r_i\}$ should also approach zero at convergence. In order to decide when to switch, we can examine the sequences of the δ_i and the r_i. If the difference in eigenvalues in consecutive iterations is not decreasing, or equivalently, that enlarging the subspace is not useful, it could be indicative of oscillation or other problems in convergence. While it would be tempting to switch immediately if either δ_i or r_i increase, we have found that even in the case of rather well-behaved systems the convergence of $\{\delta_i\}$ and $\{r_i\}$ to zero might not be monotonic. To allow for this, we recommend counting the number of iterations in which δ_i or r_i increase and only switch after a set limit is reached.

4.3 Results and Discussion

The GPLHR and associated hybrid methods were implemented in a locally modified version of the development version of the Gaussian software package [5], which includes the energy-specific Davidson method [78, 79, 87, 146]. All calculations were run using spin-unrestricted Hartree-Fock with the B3LYP density functional unless stated otherwise and molecular geometries were optimized at the same level of theory [116, 117]. Convergence was determined when either (1) the norm of all the residuals was below a set threshold, $||r|| < 10^{-5}$, or (2) the change in eigenvalues is less than 10^{-7} Hartrees. All calculations were run on a single compute node with dual Intel Xeon E5-2680 v4 processors for a total of 28 cores and 256 GB DDR3 RAM.

In this first test we show the agreement of the eigenvalues and associated eigenvectors found by our GPLHR-based approaches match those given by energy-specific Davidson. In Tab. 4.1 the first 3 states of the nitrogen K-edge above 380 eV in NO were computed with the 6-311+G(d) basis set [164, 165]. The GPLHR calculation used a subspace expansion parameter of $m = 1$. Note also that since each GPLHR iteration is roughly 4 times more expensive than a single Davidson iteration, it is performing almost twice as much work in this test case. Although there are very slight differences in excitation energies and oscillator strengths due to numerical differences in convergence, the results of Davidson and GPLHR algorithms are considered essentially identical. Interestingly, at the standard threshold used here, we find GPLHR gives a better solution than obtained in the Davidson algorithm, as it matches the solution obtained at stricter convergence criteria.

In general, for well-behaved RPA problems, such as those for small- to moderately-sized molecular systems, we found that Davidson consistently outperforms GPLHR. This itself is not surprising as GPLHR is designed for much more challenging problems, so that it often does more work than necessary. However, for systems that exhibit a dense manifold of excited states we find that using GPLHR for some or all iterations is preferred. Two illustrative examples of this, a graphene sheet and a nanodiamond, are explored here.

Table 4.1: Nitrogen K-edge of NO (σ = 380 eV)

ES-Davidson (13 iterations)			GPLHR (7 iterations)		
Excitation Energy (eV)	Oscillator Strength (a.u.)	$\langle S^2 \rangle$	Excitation Energy (eV)	Oscillator Strength (a.u.)	$\langle S^2 \rangle$
385.5845	0.0000	2.752	385.5844	0.0000	2.752
386.8976	0.0697	0.753	386.8974	0.0701	0.753
387.3633	0.0341	0.760	387.3632	0.0342	0.760

For a small cluster of graphene sheet, the first 8 states of the carbon K-edge were calculated at the unrestricted B3LYP/6-31G(d) [116, 117, 166, 167] level of theory using a combination of Davidson and GPLHR iterations. For each calculation at set number of Davidson iterations were performed first, followed by GPLHR iterations until convergence. In Fig. 4.2 we plot the cumulative number of matrix-vector products, since this is the computational bottleneck. The hybrid(n) methods denote a calculation which started using the Davidson algorithm and switched to GPLHR after n iterations. Despite all algorithms converging to the correct roots, the computational cost was least for the hybrid methods. This indicates that there was little benefit of GPLHR over Davidson in the first few iterations, and resulted in extra work being done. From an algorithmic perspective this is not too surprising, as the beginning iterations have relatively little information and so do not need to be very accurate in extrapolation to provide usable information. Conversely, one of the key reasons why the Davidson type of algorithm struggles here is that it will often include approximate eigenvectors with energies largely dominated by the residual term. This results in new trial vectors being generated that do not aid in capturing the desired region of the spectrum and leads to stagnation. The question that remains is what is a sensible strategy for switching to GPLHR from a Davidson calculation when we don't know *a priori* how the Davidson algorithm will perform.

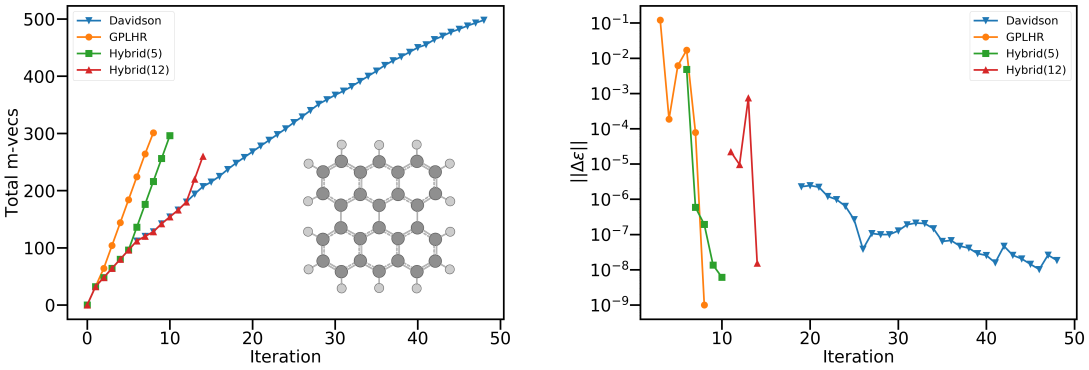

Figure 4.2: (Left) Cumulative number of matrix vector products performed at each iteration for the energy-specific Davidson, GPLHR, and hybrid methods. Here Hybrid(n) indicates that n Davidson iterations are performed before switching to GPLHR. The steeper slope of GPLHR indicates a single iteration is more expensive than a Davidson iteration. (Right) Eigenvalue convergence profiles for the 5th root above the threshold, with a vertical excitation energy of 273.468 eV. Iterations before the states could be mapped between iterations are not shown.

The determination of the K-edge spectrum of carbon in a nanodiamond cluster was used to test the power of the algorithm on an even larger system. The C_{121} structure is H-capped with 104 H and has C_{3v} symmetry as shown in Fig. 4.3 [168]. The 6-31G(d) basis set [166, 167] and B3LYP [116, 117] density functional were used for optimization and TDDFT calculations. With 2023 contracted basis functions and 830 total electrons, the dimension of the full RPA matrix is 2,669,280. The computational bottleneck is, of course, the direct formation of the matrix-vector products. The energy-specific Davidson used with a threshold of 260 eV was unable to converge the first 10 roots after almost 70 iterations, as shown in Fig. 4.3. However, all GPLHR-based hybrid algorithms with $\sigma = 260$ eV were able to converge with relative ease. Although the Davidson algorithm is unable to converge this system, forcing the switch to GPLHR on-the-fly also allowed the calculation to successfully

complete. It is worth noting that using GPLHR from the beginning would have been optimal for this case, however the sequences of the error in both the eigenvalues and the residuals show clear signs of problems converging by around iteration 5 or 6 using the Davidson method (see Tab. 4.2). While it would be impossible to make an optimal general switching rule for all systems, the sequences of error seem to indicate two or three poor iterations is a reasonable, albeit crude decision metric for detecting breakdown or stagnation. At the heart of this problem is the failure to identify the best approximate eigenvectors. Despite the inability of the hybrid method to outperform the GPLHR algorithm alone on this system, the adaptive hybrid method was nevertheless successful in minimizing the wasted computational effort in the Davidson iterations.

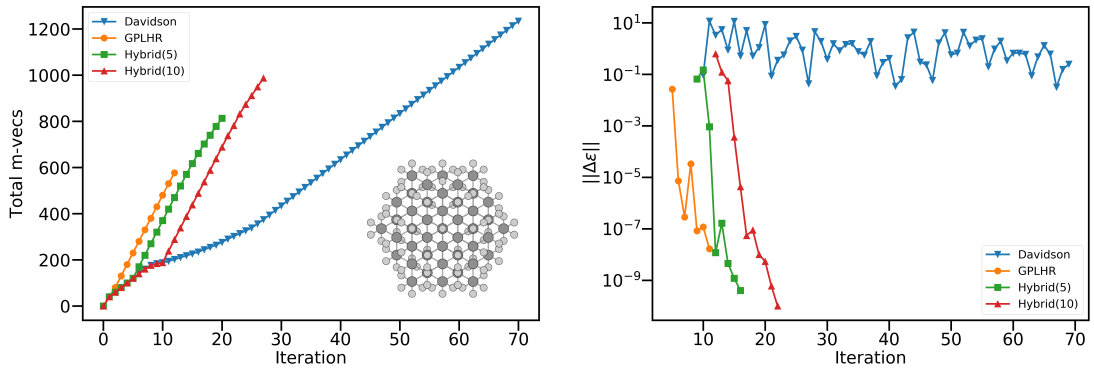

Figure 4.3: (Left) Cumulative number of matrix-vector products for the $C_{121}H_{104}$ nanodiamond at the 6-31G(d)/UB3LYP level of theory. Hybrid(n) indicates that n Davidson iterations are performed before switching to GPLHR. (Right) Eigenvalue convergence profile for the 1st root above the 260 eV threshold, with a vertical excitation energy of 276.681 eV. Iterations before the states could be mapped between iterations are not shown. Note that the Davidson calculation did not converge within the 70 iterations.

Table 4.2: Norms of errors in eigenvalues and residuals at each Davidson iteration for the $C_{121}H_{104}$ nanodiamond at the 6-31G(d)/UB3LYP level of theory. The two sequences of $\{\delta_i\}$ and $\{r_i\}$ can be used to determine failure of the Davidson algorithm.

Iteration	Eigenvalue Error (a.u.) $\{\delta_i\}$	Residual Error (a.u.) $\{r_i\}$
1	64.4953	0.00625
2	0.01464	0.00616
3	0.00608	0.00516
4	0.00139	0.00523
5	0.00823	0.11783
6	0.52223	0.08276
7	0.30772	0.27291
8	0.21657	0.00600
9	0.04076	0.08877
10	0.00648	0.09303

4.4 Conclusion

This paper presents an implementation of a hybrid Davidson–GPLHR algorithm for the solution of the non-Hermitian TDHF/TDDFT equations and explores several modifications. First, since the standard energy-specific Davidson algorithm often performs well, we include the ability to switch to the GPLHR solver on the fly. The additional cost GPLHR suffers by doing more work than is often necessary for the RPA problem makes it less desirable to use on its own, but can provide additional robustness for hard to converge problems with dense sets of states in the interior of the spectrum. Second, we also include the ability to have the shift value σ adaptively change so that only the first n states above a predefined energy threshold. This feature is crucial to avoid reconvergence of states when predicting the absorption spectrum over a broader energy range.

It should be noted that if the matrix can be stored in memory, standard diagonalization routines should always be used. However this is often not practical for many systems of interest and one must resort to using iterative direct methods where the matrix-vector products are performed on the fly. Adaptive switching between diagonalization methods has the potential to provide superior performance in hard-to-converge eigenvalue problems, including those that are common in X-ray spectroscopy of molecular systems. However, even in cases where using either algorithm alone would be optimal, the adaptive hybrid method provides a reasonable compromise without knowing which one is best *a priori*.

Chapter 5

NATURAL TRANSITION ORBITALS FOR COMPLEX TWO-COMPONENT EXCITED STATE CALCULATIONS

The time-dependent Hartree–Fock (TDHF) and time-dependent density functional theory (TDDFT) equations are widely used as a first approximation to understanding electronic excited states. While the natural transition orbital method has allowed electronic excitations from time-dependent Hartree–Fock (TDHF) and density functional theory (TDDFT) to be viewed in a traditional orbital picture, the extension to multicomponent molecular orbitals such as those used in relativistic two-component methods or generalized Hartree–Fock (GHF) or generalized Kohn–Sham (GKS) is less straightforward due to mixing of spin-components and the inherent inclusion of spin-flip transitions in TDGHF/TDGKS. An extension of single-component natural transition orbitals to the two-component framework is presented, in addition to a brief discussion of the practical aspects of visualizing two-component complex orbitals. Unlike the single-component analog, the method explicitly describes the spin and frequently obtains solutions with several significant orbital pairs. The method is presented using calculations on a mercury atom and a CrO_2Cl_2 complex. The work in this section is adapted with permission from Joseph M. Kasper and Xiaosong Li. *J. Comp. Chem.*, **2020**, *41 (16)*, 1557-1563.

5.1 Introduction

Complex, multicomponent electronic structure methods are the natural framework for calculations that explicitly include relativistic effects from an *ab initio* approach based on the four-component Dirac Hamiltonian [9, 10, 169]. Phenomena such as spin-orbit coupling can then be included variationally. Although one can work directly with the four-component

Dirac Hamiltonian, much effort has gone into the development of a large variety of methods that transform the four-component Dirac Hamiltonian into a two-component form to reduce computational cost [12, 13, 15, 14, 16, 17, 26, 27, 28, 29, 39, 42, 43, 44, 61, 101, 102, 104, 105, 170, 171, 172, 173]. For excited state calculations, linear response time-dependent density functional theory (LR-TDDFT) [139, 140, 141] has become the method of choice for molecules that are too large to be studied by more accurate wavefunction-based methods due its balance of reasonable accuracy and much decreased cost. While efficient implementations of LR-TDDFT [87, 146, 147, 148] have been consistently employed for both the restricted and unrestricted Kohn–Sham frameworks, more recently the development of linear response methods for two-component references have been used to study spectroscopic properties of small molecules and clusters [105, 174, 175, 176].

Beyond the goal of obtaining reasonable quantitative agreement to experimental spectra, the ability to gain a qualitative understanding of the underlying physics in excited state processes is of central importance to improved design and control of molecular structure and function. On their own, the linear response methods of TDHF and TDDFT provide an efficient way to calculate electronic excited states, but can be hard to interpret since transitions will in general involve many occupied and virtual canonical orbitals. Schemes such as natural transition orbitals (NTOs) [177] or natural ionization orbitals [178] that localize transitions to a small number of single particle-hole pairs have been developed to aid in physical insight. Despite the success of this work for single-component methods, there has been little work done to apply this method to two-component theories within the generalized Hartree–Fock (GHF) or Kohn–Sham (GKS) frameworks. Krause and Klopper plotted difference densities for two-component RI-CC2 calculations [179], and recent work using two-component Green's functions (GW) and Bethe-Salpeter have used similar techniques to visualize excitations [180]. In Martin's original paper on NTOs, the extension to spin-unrestricted theory is suggested to transform the spin indices separately, so that the $\alpha\alpha$ and $\beta\beta$ blocks are individually diagonal. For two-component TDHF/TDDFT, however, the orbitals explicitly contain information about spin, in addition to having complex coefficients.

In this paper we explore the extension of NTOs to two-component GHF/GKS linear response theory and some of the ways they differ from those of standard single-component calculations. A discussion of how to effectively visualize the resulting two-component orbitals is also included.

5.2 Complex Two-Component Natural Transition Orbitals

The two-component ℂ-TDHF and ℂ-TDDFT equations are based on the spinor molecular orbital ansatz,

$$\psi_k(\mathbf{r},t) = \begin{pmatrix} \phi_k^\alpha(\mathbf{r},t) \\ \phi_k^\beta(\mathbf{r},t) \end{pmatrix} \tag{5.1}$$

where the spatial functions $\{\phi_k^\alpha(\mathbf{r},t)\}$, $\{\phi_k^\beta(\mathbf{r},t)\}$ are expanded in terms of a common set of basis functions $\{\chi_\mu(\mathbf{r})\}$

$$\phi_k^\alpha(\mathbf{r},t) = \sum_\mu c_{\mu k}^\alpha(t)\chi_\mu(\mathbf{r}) \tag{5.2}$$

$$\phi_k^\beta(\mathbf{r},t) = \sum_\mu c_{\mu k}^\beta(t)\chi_\mu(\mathbf{r}) \tag{5.3}$$

Note that expansion coefficients $\{c_\mu\}$ are complex valued. Methods that use such spinor orbitals can be further modified to include relativistic effects, such as spin-orbit coupling, which mixes spin states internally on account of the spin-orbit operators.

The linear response formalism of the two-component TDHF or TDDFT equations can be written as,

$$\begin{pmatrix} \mathbf{A} & \mathbf{B} \\ \mathbf{B}^* & \mathbf{A}^* \end{pmatrix} \begin{pmatrix} \mathbf{X} \\ \mathbf{Y} \end{pmatrix} = \omega \begin{pmatrix} 1 & 0 \\ 0 & -1 \end{pmatrix} \begin{pmatrix} \mathbf{X} \\ \mathbf{Y} \end{pmatrix} \tag{5.4}$$

where the matrix elements are defined as

$$A_{ai,bj} = \delta_{ab}\delta_{ij}(\epsilon_a - \epsilon_i) + (ia|jb) - \alpha(ib|ja) + (1-\alpha)(ia|f_{xc}|jb) \tag{5.5}$$

$$B_{ai,bj} = (ia|bj) - \alpha(ij|ba) + (1-\alpha)(ia|f_{xc}|bj) \tag{5.6}$$

Here the two-electron repulsion integrals (ERIs) are expressed in the spinor molecular orbital basis in Mulliken notation, with the usual i and j indices used for occupied MOs and a and b indices for virtual MOs. The orbital energy of MO p is given by ϵ_p, and α is a real scaling factor that determines the fraction of Hartree–Fock exchange to be included with the density exchange-correlation functional f_{xc}. In the case of TDHF, $\alpha = 1$. The coefficients contained in the eigenvector $|\mathbf{X}\,\mathbf{Y}\rangle$ describe the amplitudes of orbital transitions. In practice, instead of forming and diagonalizing the entire response matrix on the left-hand side of Eq. (5.4), the matrix is iteratively diagonalized for a subset of states through Davidson-like algorithms [79, 87, 142, 181]. Trial vectors $|\mathbf{X}_i\,\mathbf{Y}_i\rangle$ are used to compute a transition density that is transformed to the AO basis for direct contraction with the ERIs and/or DFT kernel second derivatives. The transition density matrix for a vector $|\mathbf{X}_i\,\mathbf{Y}_i\rangle$ in the MO basis has the form

$$\mathbf{T}_i = \begin{pmatrix} 0 & -\mathbf{Y}_i \\ \mathbf{X}_i & 0 \end{pmatrix} \tag{5.7}$$

However, as there is no clear physical meaning of the "deexcitation" amplitudes in the $\mathbf{Y}$ block [148], analysis has usually centered on the excitation amplitudes in the $\mathbf{X}$ block. From the configuration interaction point of view, these coefficients correspond to the weights of the singly excited determinants. That is, the excited-state wavefunction Ψ can be approximated by

$$\Psi = \sum_{i,a} C_{ia} \Phi_{ia} \tag{5.8}$$

where Φ_{ia} is the singly excited configuration generated by creating a hole in orbital i and an electron in orbital a. In second quantization this is

$$\Phi_{ia} = \hat{a}_a^\dagger \hat{a}_i \,|\Phi_0\rangle \tag{5.9}$$

In the following analysis the transition density corresponding to the excitation from the ground state $\Psi_0 = \Phi_0$ to an excited state Ψ_n is then given by

$$T_{ia} = \langle \Psi_n |\, C_i^\dagger C_a \,|\Psi_0\rangle \tag{5.10}$$

Note that this is the **X** block in Eq. (5.7) only. Also, in contrast to conventional one-component method where α and β spin components are treated separately, transition densities in the complex two-component framework include all possible spin contributions. As a result, the summation over spin coordinates is no longer needed, in contrast to the definition presented in the work of Martin [177].

While it is possible to work directly with densities, the NTO analysis still tries to preserve the single particle orbital picture through which many chemists have an intuitive understanding of chemical activity. The NTO analysis relies on an orbital transformation of Amos and Hall[182] in which the orbitals are rotated so that the transition amplitudes of the particle and hole are localized in as few orbitals as possible. Essentially both the hole and electron parts of the transition vector, **T**, are biorthogonalized via the singular value decomposition (SVD) to maximize the single particle character of the transition. More specifically, let $\{\phi_i\}$ and $\{\psi_a\}$ be the sets of occupied and virtual canonical orbitals, respectively, and we determine two transformation matrices **U** and **V** to obtain rotated sets of natural orbitals $\{\phi_i^{'}\}$ and $\{\psi_a^{'}\}$ for a given electronic transition. These can be determined by diagonalizing the matrices $\mathbf{T}\mathbf{T}^\dagger$ and $\mathbf{T}^\dagger\mathbf{T}$, respectively, in the following eigenvalue equations:

$$\mathbf{T}\mathbf{T}^\dagger u_i = \lambda_i u_i \tag{5.11}$$

$$\mathbf{T}^\dagger\mathbf{T} v_i = \lambda_i v_i \tag{5.12}$$

The eigenvalues (or singular values) determine the relative importance of each orbital to the description of the transition. Neglect of the **Y** block in Eq. (5.10) results in transition vectors that are no longer perfectly normalized to one, so the sum of the λ_i of all NTOs may differ from exactly one. We make note that the natural orbitals here contain multiple spin components, and thus also implicitly include any transitions that have "spin-flip" character.

5.3 Visualizing Excitation Properties in Complex, Two-Component Framework

The two-component generalized natural transition orbitals was implemented in a locally-modified version of the development version of Gaussian [5] and applied to some small molecular clusters using the X2C-TDDFT method [105, 183, 184]. Once orbitals are obtained, a further complication associated with the two-component, complex orbitals encountered in both relativistic and non-relativistic two-component theories is the need to reduce the dimensionality for visualization since the orbitals may include both α and β spin components. Several options for this include (1) rotating the quantization axis if possible, (2) plotting the total magnitude and spin mixing angle, and (3) plotting the spinor magnetization density.

Before considering the general case, it is instructive to consider how to plot a single-component complex orbital. Then at any point $\mathbf{r}$ in space the wavefunction Ψ is given by a complex amplitude $\Psi(\mathbf{r}) = z = a + ib$. This can be transformed to the polar form $|z|e^{i\theta}$, according to

$$|z| = \sqrt{a^2 + b^2} \tag{5.13}$$

$$\theta = \text{atan2}(b, a) \tag{5.14}$$

where atan2 is the two-argument arctangent function. In contrast to the real-valued case in which it is customary to plot magnitude and sign, the complex orbital has magnitude $|z|$ and phase θ. The sign or phase is most useful to allow one to quickly see the nodal structure. Since the phase is a continuous degree of freedom, it can be plotted as a color map on an isosurface defined by the magnitude.

To demonstrate this, we use the lowest-energy singlet state of the O_2 molecule, which has a real to complex instability at the RHF level of theory [185]. This instability is the result of a degenerate set of π^* antibonding orbitals, which span the Π_g irreducible representation in $D_{\infty h}$. A qualitative energy diagram of the frontier orbitals is given in Fig. 5.1. The lowest-energy singlet is doubly-degenerate and given by the term $^1\Delta_g$. This corresponds to a linear combination of the two possible real RHF configurations, which result in an artificial

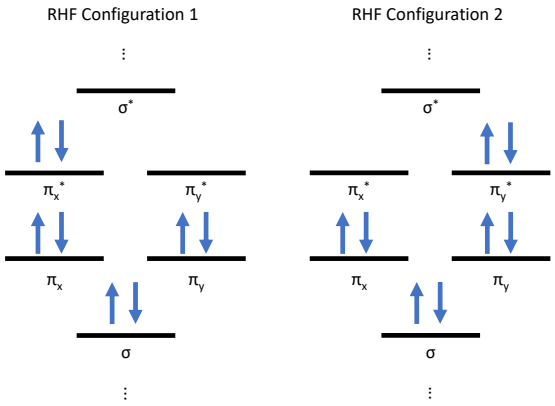

Figure 5.1: A qualitative orbital energy diagram for $^1\Delta$ O_2. The two possible singlet configurations that result from $\mathbb{R}$-RHF are given.

symmetry breaking. In particular, we obtain the linear combination $(\pi_x^*\pi_x^* - \pi_y^*\pi_y^*) + i(\pi_x^*\pi_y^* + \pi_y^*\pi_x^*)$.

These different configurations can be seen in Fig. 5.2, which plots the HOMO for both the $\mathbb{R}$-RHF and $\mathbb{C}$-RHF wavefunctions. Note that there is a modification of the nodal structure due to the continuous change of the phase with rotation about the bond for the complex case. The reduction in nodal planes in the complex orbital is consistent with the lowered energy of the $\mathbb{C}$-RHF solution. We will not further discuss the O_2 system or the utility of $\mathbb{C}$-RHF, but instead refer the interested reader to the work in Ref. 185.

The mapped isosurface technique works reasonably well for the complex single-component case where there are only two continuous degrees of freedom. For complex two-component wavefunctions with four continuous degrees of freedom there is no easy way to convey all the information at once. Typically molecular orbitals are plotted without any spin information, since in one-component calculations the α and β spin manifolds are separated. However, for two-component calculations the molecular orbitals contain additional information about the spin. In this case, several techniques may be used to emphasize either the spin or phase information.

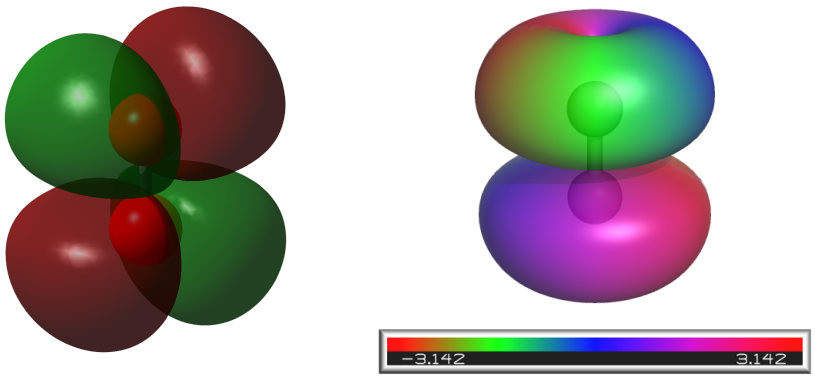

Figure 5.2: The HOMO for the real RHF (left) and complex RHF (right) wavefunctions of $^1\Delta$ O_2. An isovalue of 0.02 $a_0^{-3/2}$ for the magnitude was used.

5.3.1 Visualizing Complex, Two-Component Natural Transition Orbitals

Recent work by Al-Saadon and coworkers has explored some aspects of plotting complex-valued orbitals [186]. To illustrate how to plot complex, two-component orbitals we first show the natural transition orbitals for excitations in an atomic system using a relativistic X2C-TDHF calculation on a mercury atom using the SARC-DKH2 basis [187, 188]. The results here obtain the correct degeneracies of the $6s \rightarrow 6p$ transitions, where the lowest lying excited states correspond to the $^3P_0$, $^3P_1$, and $^3P_2$ levels. Table 5.1 lists the computed energies and oscillator strengths associated with these excitations with only $^1S_0 \rightarrow {}^3P_1$ being weakly allowed. Although the energies are too low due to a lack of correlation, the spacing between the different J levels compares well with experiment [189]. The two largest eigenvalues from the NTO analysis are given as λ_1 and λ_2. The $^1P_1$ term also arising from an $s \rightarrow p$ transition is higher in energy and not shown. As the calculation is over spin-orbitals, due to the presence of a degenerate hole state the transitions are split into two main components, λ_1 and λ_2. For the J-conserving excitation ($^1S_0 \rightarrow {}^3P_0$), equal weights of the two NTO transitions are observed, while states of higher multiplicity may have varying

Table 5.1: X2C-TDHF results for the low-lying excited states of Hg atom.

Excited State	Experiment [189]	ΔE (eV)	f	λ_1	λ_2
$^3P_0$	4.667	2.523	0.000	0.559	0.559
$^3P_1$	4.886	2.881	0.003	0.588	0.497
$^3P_1$	4.886	2.881	0.003	0.588	0.497
$^3P_1$	4.886	2.881	0.003	0.562	0.524
$^3P_2$	5.461	3.685	0.000	0.866	0.161
$^3P_2$	5.461	3.685	0.000	0.641	0.385
$^3P_2$	5.461	3.685	0.000	0.626	0.402
$^3P_2$	5.461	3.685	0.000	0.738	0.289
$^3P_2$	5.461	3.685	0.000	0.857	0.171

components as the degenerate eigenvectors are free to mix.

Although splitting up spin components and treating them separately can be a useful approach, it can also obscure some features as spin is no longer a good quantum number. Instead, one can compute the total magnitude and plot the angle of spin mixing. This allows one to easily see the total shape, but still retain some information about the phase and spin character. That is, at a given point $\mathbf{r}$, the wavefunction Ψ is given as a vector in $\mathbb{C}^2$ with

$$\Psi(\mathbf{r}) = \begin{pmatrix} a+bi \\ c+di \end{pmatrix} \tag{5.15}$$

Then we can compute the magnitude $|\Psi| = \sqrt{a^2+b^2+c^2+d^2}$ and a spin mixing angle $\theta = \text{atan2}\left(\sqrt{a^2+b^2}, \sqrt{c^2+d^2}\right)$ that correspond to the total amplitude and the relative spin direction, respectively. A mixing angle of zero, corresponds to a completely α-aligned spinor, while an angle of $\pi/2$ corresponds to a completely β-aligned spinor. We plot the α and β components separately as well as the total magnitude for the Hg excited states in Fig. 5.3.

Only the most significant NTO pair is shown, however we remark that in this atomic system the second NTO pair are the Kramers'-paired orbitals of the first, so no information is lost. The overall wavefunction magnitude is spherically symmetric for the electron NTO in the ${}^1S_0 \rightarrow {}^3P_0$ excitation. However for the ${}^1S_0 \rightarrow {}^3P_1$ excitations, the electron NTO forms torus-like rings, consistent with a state that has non-zero expectation value for $\hat{L}^2$.

5.3.2 Visualizing Magnetization Vectors

For molecular complexes with non-zero magnetic momentum, it is often advantageous to visualize the spin structure. Since an individual electron in an orbital has some nonzero spin angular momenta this is always an option, and techniques for visualizing the magnetization density can obviously be employed for individual spinor orbitals. Although two-component density matrices can be written in a spin-block form, it is more physically intuitive to write them in the Pauli matrix representation by defining the scalar density $n(\mathbf{r})$ and magnetization density $\mathbf{m}(\mathbf{r})$:[105, 183]

$$\mathbf{P} = \begin{pmatrix} \mathbf{P}^{\alpha\alpha} & \mathbf{P}^{\alpha\beta} \\ \mathbf{P}^{\beta\alpha} & \mathbf{P}^{\beta\beta} \end{pmatrix} = \frac{1}{2} n(\mathbf{r}) \boldsymbol{\sigma}_0 + \frac{1}{2} \mathbf{m}(\mathbf{r}) \circ \boldsymbol{\sigma} \tag{5.16}$$

where $\boldsymbol{\sigma}_0$ is the identity in spin coordinates and $\boldsymbol{\sigma}$ is the vector of the Pauli spin matrices. We use an open circle to emphasize that the summation is over spin and not spatial components. The spinor formalism accomplishes this same task, and provides a convenient way to determine the local spin vector. At a given point $\mathbf{r}$, the wavefunction is given as a vector in $\mathbb{C}^2$ as in Eq. (5.15). This vector $\mathbf{s}$ can be re-expressed as

$$\mathbf{s} = s e^{-i\alpha/2} \begin{pmatrix} \cos(\theta/2) e^{-i\phi/2} \\ \sin(\theta/2) e^{i\phi/2} \end{pmatrix} \tag{5.17}$$

where the four real parameters are the magnitude s, two angles θ and ϕ corresponding to the polar and azimuthal angles that determine the spin axis, and a phase α. These spherical coordinates can be directly converted to cartesian coordinates, or equivalently the Cartesian

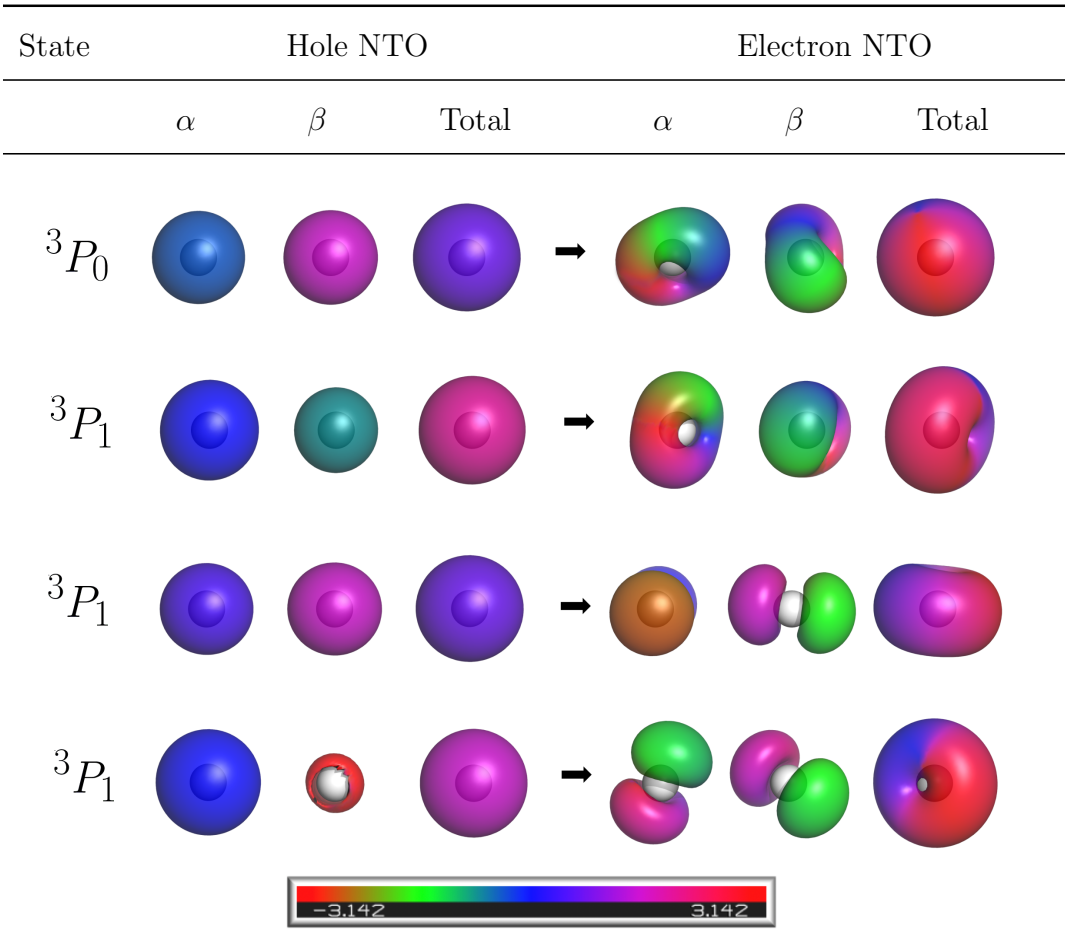

Figure 5.3: Mapped isosurfaces showing the hole and electron wavefunctions for the most significant NTO pair of the first four excited states in Hg. An isovalue of 0.02 $a_0^{-3/2}$ is used for the magnitude.

components of the spinor $\mathbf{s}$ are given by taking expectation values with the corresponding Pauli matrices:

$$s_k = \langle \mathbf{s} | \, \sigma_k \, | \mathbf{s} \rangle \ , \ k \in \{x, y, z\} \tag{5.18}$$

In cases where s is still a good quantum number, there is a global quantization axis for a given orbital. That is, the expectation value of the spin is constant for all points in space, and we could easily choose to align our spin quantization axis with this (not necessarily z-aligned) axis. However, in cases where s is not a good quantum number, such as when there is significant spin-orbit coupling, then it is no longer possible to find such unique axis. Instead, the spinor direction rotates between points in space, since it is collinear with j and not with s. An example of these cases are shown in Fig. 5.4 where the first four excitations of the Hg atom are shown. The hole state is of essentially s character and has no angular momentum to couple with, resulting in a collinear spin. Thus the magnetization vectors are aligned at all points in space. By contrast, the electron in the excited state is in the p manifold and forms states that are collinear with respect to j rather than s. As a result, magnetization densities of the electron NTO clearly exhibit vortical structures, showing non-collinear spin and non-zero magnetic moment in the excited states.

5.3.3 CrO_2Cl_2 $L_{2,3}$-edge X-ray Absorption

The construction and visualization of NTOs is most useful in molecular species, where more complicated combinations of orbitals are present. One practical example of the use of two-component relativistic TDDFT is in the calculation of L-edge X-ray spectra [184, 190]. Due to the presence of spin-orbit coupling in the $2p$ manifold, the main features in the X-ray absorption near-edge structure (XANES) region are split into two groups known as L_2 and L_3. These correspond to the $2p_{1/2}$ and $2p_{3/2}$ core-levels. In Fig. 5.5 we plot the NTOs associated with one of the bright transitions from each of the L_2 and L_3 regions in the XANES spectrum of a CrO_2Cl_2 complex calculated using X2C-TDDFT [39] at the B3LYP [116, 191]/aug-cc-pVTZ [118, 119, 120, 121] level of theory. The total magnitude is used to

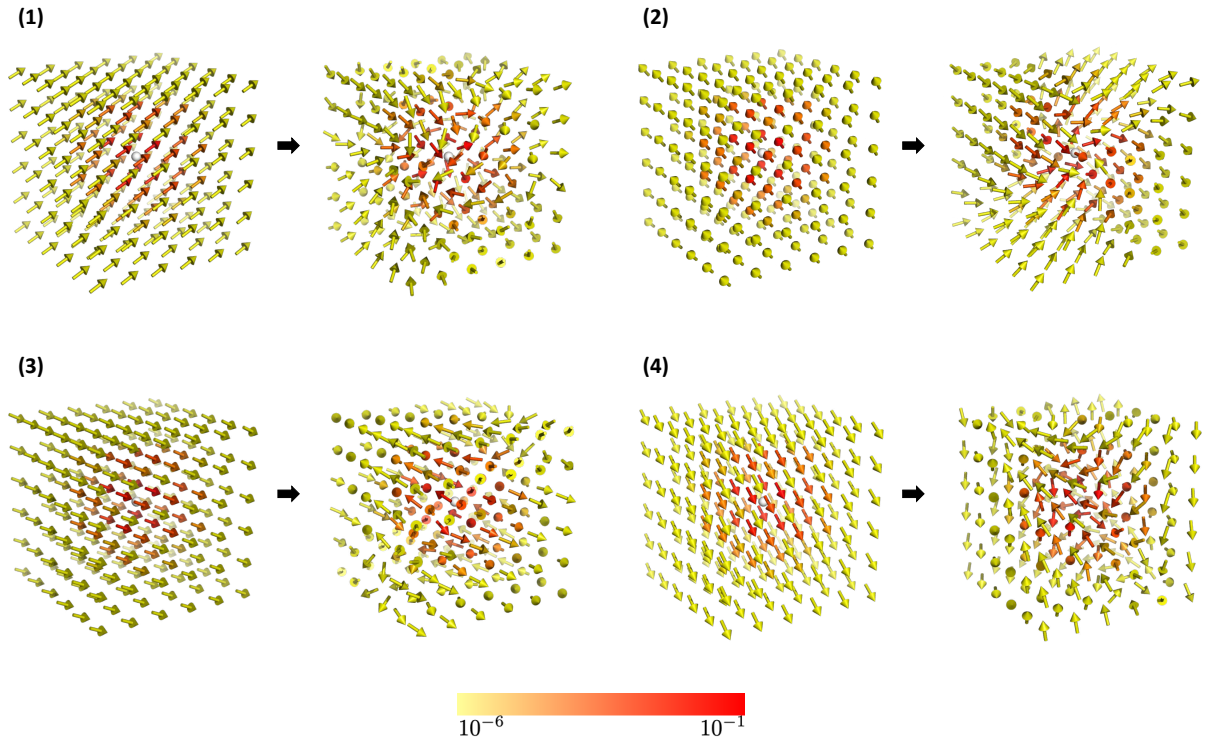

Figure 5.4: The spinor representations of the transition orbitals for the first four excitation in Hg. (1) $^1S_0 \rightarrow {}^3P_0$; (2), (3), and (4) comprising the $^3P_1$ manifold. The colors of the arrows indicate the magnitude of the wavefunction in $a_0^{-3/2}$.

generate an isosurface and the phase angle of the mixing between the α and β components is mapped onto it, as described previously. For both pairs of NTOs the core hole is clearly composed of the Cr $2p$ orbitals due to the presence of a radial nodal plane between spin angles of 0 and π, while the electron orbitals show that the excitation includes not only Cr d orbitals, but is also significantly delocalized into the p orbitals of the O and Cl atoms. One can also see that these dipole-allowed transitions between the L_2 and L_3-edges involve different d-orbitals on the Cr center, in order to fulfill the dipole selection rule due to the difference in angular momenta between the $p_{1/2}$ and $p_{3/2}$ manifolds.

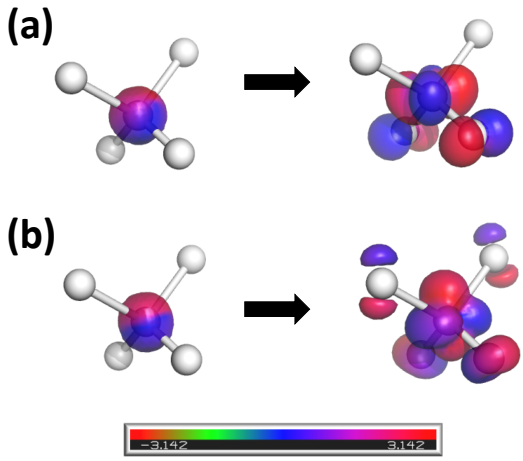

Figure 5.5: Mapped isosurfaces showing the most significant NTOs for two excited states in the $L_{2,3}$ XANES of a CrO_2Cl_2 complex computed with X2C-TDDFT. (a) is a transition at 575.373 eV from the L_2 region and (b) is a transition at 566.369 eV from the L_3 region. The surfaces are plotted with isovalues of 0.002 $a_0^{-3/2}$ and 0.06 $a_0^{-3/2}$ for the total magnitude of the hole and electron NTOs, respectively, while the phase shows the angle between the α and β components.

5.4 Conclusion

This paper presents a generalization and implementation of natural transition orbitals for the complex two-component time-dependent generalized Hartree–Fock and generalized Kohn–Sham theories. Unlike one-component theories that separate spin components, there is no rigorous separation available in a two-component framework. A straightforward use of the singular value decomposition procedure tends to produce multiple important orbitals due to the spin orthogonality of the basis functions. These orbitals can sometimes be well described by a single (non z-aligned) spin component, however this is not true in general, such as when spin-orbit coupling is included. The orbitals can still be plotted using techniques such as mapped isosurfaces, though for cases in which spin is non-collinear other techniques

such as plotting expectation value of the spinor at each point may be more appropriate to see the magnetization structure. The use of two-component TDDFT, including all-electron relativistic methods, will be enhanced by the use of the NTO orbital analysis as well as improved visualization of complex orbitals. A qualitative picture of how both charge and spin change under excitation is important to elucidate chemical and physical insight into the properties of molecules.

Chapter 6

THEORETICAL INVESTIGATION OF QUANTUM CONFINEMENT ON THE RASHBA EFFECT IN ZnO SEMICONDUCTOR NANOCRYSTALS

Semiconducting nanocrystals have been the subject of intense research due to the ability to modulate the electronic and magnetic properties by controlling the size of the crystal, introducing dopants, and surface modification. While relatively simple models such as a particle in a sphere can work well to describe moderately sized quantum dots, this approximation becomes less accurate for very small nanocrystals that are strongly confined. In this work, we report all-electron, relativistic ab initio electronic structure calculations for a series of ZnO quantum dots in order to study the modulation of the Rashba effect. The impact and magnitude of spin-orbit coupling and crystalline anisotropy on the fine structure of the band-edge excitonic manifold are discussed. The work in this section is adapted with permission from Joseph M. Kasper, Daniel R. Gamelin, and Xiaosong Li, *J. Chem. Phys.* (**2020**), *152 (1)*, 014308.

6.1 Introduction

The fine control of electronic and magnetic phenomena in nanomaterials is integral to new technologies in computing and data storage. Small colloidal nanocrystals, or quantum dots, have shown great promise in this regard, by allowing properties to be easily tuned through size, dopants, and surface ligands [192, 193]. One of the most important adjustable properties of nanocrystals is the band structure, including the relative ordering of bright and dark excitonic states [194]. The precise arrangement of states and their thermal population determines properties such as photoluminescence lifetimes.

Studying quantum dots from the viewpoint of molecular electronic structure theory is extremely powerful to understand the role of localized defects, and size-dependent quantum confinement effects [195, 196, 197, 198]. The electronic structure of several types of nanocrystals has been shown to mimic that of a large atom [197] so that it can be reasonably well-described and understood by a simple particle is in a sphere model [199]. In this case, excitonic structure is determined by a combination of spin-orbit and symmetry effects that split 'P'- and 'D'-like superorbitals. In fact, the superatom concept has previously been applied to study nanoclusters of gold thiolate [174, 200, 201] and show that in these systems spin-orbit coupling was essential to their theoretical treatment and understanding of visible absorption spectra [174].

Much work has been done to understand the role of spin-orbit coupling in bulk-like structures using $\mathbf{k}\cdot\mathbf{p}$ band theory and perturbative spin-orbit corrections [202, 203, 204]. For example, in a recent work by Sercel and Efros[204] a general model for exciton fine structure of II-VI and III-V spherical semiconductor nanocrystals was presented. While these models provide a useful starting point to study band features of moderately-sized nanocrystals, they are less amenable to smaller nanocrystals and the impact of localized structural features such as dopants. To our knowledge there has been no study into how the spin-orbit interaction is manifested in small quantum dots using relativistic *ab initio* molecular electronic structure methods.

Additionally, we note that for studies that have been carried out using band theory, the spin-orbit interaction is usually incorporated perturbatively by a model Hamiltonian (*e.g.*, Pauli) rather than variationally from first principles. In this work, we calculate the electronic structure of semiconducting quantum dots using two-component Kohn-Sham density functional theory that variationally incorporates relativistic effects and spin-orbit coupling. Using excited-state calculations, the fine structure of the exciton manifold and the impact of Rashba spin-orbit coupling under strong quantum confinement is uncovered.

6.2 Relativistic Treatment of the Rashba Effect

For crystals without inversion symmetry, it is well-known that the electronic structure is modified by spin-orbit coupling to split low-energy excitons as shown in Fig. 6.1 for a wurtzite lattice that has hexagonal C_{3v} symmetry. The lowest-energy exciton manifold is known in the literature as the $1S_{3/2}1S_e$ state. This results from treating the electron and hole particles using the particle in a sphere model and dressing the solutions with appropriate angular momentum functions. That is, the $1S_{3/2}$ valence band hole level corresponds to the product of a 1S Bessel function with the $J = 3/2$ Bloch functions and the $1S_e$ conduction band electron level corresponds to the product of a 1S Bessel function with the $J = 1/2$ Bloch functions [204].

The breaking of degeneracy of low-energy excitons is described within $\mathbf{k} \cdot \mathbf{p}$ theory as a momentum-dependent perturbation. Rashba spin-orbit coupling in the bulk is given by [205]

$$\hat{H}_R = (\alpha_R/\hbar)(\mathbf{z} \times \mathbf{p}) \cdot \boldsymbol{\sigma} \tag{6.1}$$

where α_R is the Rashba coefficient, and $\mathbf{z}$ is the direction of crystal anisotropy. From a molecular orbital point of view, the Rashba effect arises from *both* spin-orbit coupling and crystal field or symmetry-lowering effects. In principle these could be viewed as two successive perturbations, as is given schematically in Fig. 6.1. However, since spin-orbit coupling is known to be quenched by reduced symmetry [206], one of the two effects may dominate depending on their relative strengths, being either closer to the right or left of the diagram in Fig. 6.1. Quantum confinement affects both $\mathbf{z}$ and $\mathbf{p}$ in Eq. (6.1) depending on the nanocrystal size $\mathbf{R}$. In large nanocrsytals that can be well-described by the particle in a sphere model [207, 208, 199], because $\langle p^2 \rangle \sim E \sim R^{-2}$ so that $\mathbf{p}$ scales as $\mathbf{R}^{-1}$ and $\mathbf{z} \propto \mathbf{R}$, the overall effect of spin-orbit coupling is independent of the nanocrystal size. For much smaller nanocrystals however, as the particle in a sphere model breaks down with increasing Coulomb and exchange interaction, there can be larger values of $\mathbf{p}$ for a given confinement $\mathbf{R}$. As a result, the overall strength of the Rashba spin-orbit coupling can thus be expected to increase for small nanocrystals that are heavily quantum confined, compared with larger nanocrystals

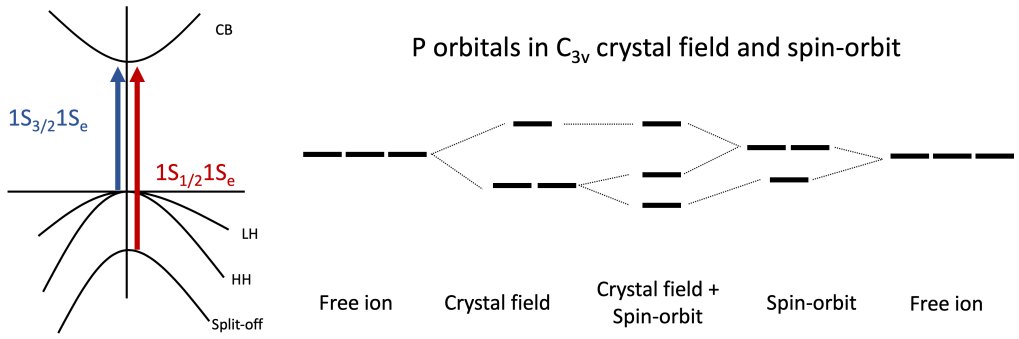

Figure 6.1: Schematic diagrams of the valence band structure (left) and valence orbitals (right) for systems with both symmetry-lowering and spin-orbit coupling. Excitations from these orbitals or bands to the lowest unoccupied levels give rise to the lowest energy excitons, known as the $1S_{3/2}1S_e$ and $1S_{1/2}1S_e$.

or those in the bulk. In particular, the exchange interaction has been implicated in providing enhancement of spin-orbit coupling in quantum confined systems.[209] Theoretical work on quantum wires has suggested that there exists an optimal value of the potential barrier to the confinement well where the spin-orbit coupling will be maximized [210].

While the Schrödinger equation is commonly employed to solve the electronic structure of molecular systems, the natural starting point for including a full description of spin, including spin-orbit coupling and other relativistic effects, is to start with the Dirac equation for an electron. Within the kinetic-balance condition, the Dirac Hamiltonian for a single electron can be written as [9, 10]

$$\mathbf{H} = \begin{pmatrix} V & \hat{T} \\ \hat{T} & \frac{\mathbf{p}V\cdot\mathbf{p}}{4m^2c^2} - \hat{T} \end{pmatrix} + \begin{pmatrix} \mathbf{0}_2 & \mathbf{0}_2 \\ \mathbf{0}_2 & \frac{i\boldsymbol{\sigma}\cdot\mathbf{p}V\times\mathbf{p}}{4m^2c^2} \end{pmatrix} \tag{6.2}$$

where V is the scalar potential, c the speed of light, and m the electron mass. Spin and orbital angular momenta are coupled through the $\boldsymbol{\sigma}\cdot\mathbf{p}V\times\mathbf{p}$ term: the vector $\boldsymbol{\sigma}$ contains the Pauli spin matrices, and $\mathbf{p}$ is the linear momentum operator. Variational solutions to this Hamiltonian will no longer have a well-defined spin multiplicity, and the eigenstates

will have four components. The first term in Eq. (6.2) is the spin-free portion of the Dirac Hamiltonian, which contains all scalar relativistic effects, while the second term gives rise to spin-couplings. To isolate the effect of spin-orbit coupling, we can compare the results using the full Dirac Hamiltonian with those using only the spin-free part.

Relativistic electronic structure methods based on the Dirac equation employ a four-component wavefunction ansatz [9, 10]. For most chemically relevant studies, approximate two-component methods are usually of sufficient accuracy. In this work we utilize the exact two-component (X2C) method [12, 13, 14, 15, 16, 17, 18, 19, 39, 101, 102, 105, 211] that decouples the four-component Hamiltonian and yields a reduced-dimension electronic two-component Hamiltonian. It is of particular note that, unlike effective spin-orbit operators such as Breit–Pauli, the X2C transformed Hamiltonian is bounded from below and does not suffer from variational collapse [9, 10]. Consequently, this two-component method allows for the variational inclusion of relativistic effects at each stage of the calculation.

In this work, we use a direct atomic-orbital based X2C transformation with the torque-free density functional theory (DFT) approach [54, 55, 56, 39, 105, 183]. Although X2C can be made formally exact to the 4-component solution, in practice, the two-electron operator is not transformed as this is very computationally expensive. Instead, in this work we use an empirical correction to the one-electron spin-orbit terms to account for the neglected two-electron contribution [51].

6.3 Computational Details

Cluster models of ZnO quantum dots ranging in size from a diameter of 0.62 to 1.87 nm were prepared in accordance with previous studies [196, 197, 212, 213, 214, 215, 216] and are shown in Fig. 6.2. A pseudo-hydrogen capping scheme is used to passivate the dangling bonds on the surface [212]. The clusters use the experimental lattice parameters of $a = 3.249$ Å and $c = 5.204$ Å for ZnO. All are approximately spherical, but formally have reduced symmetry in the C_{3v} point group. All-electron calculations were performed in a locally modified version of the development version of the Gaussian suite of programs [5] using the X2C method as

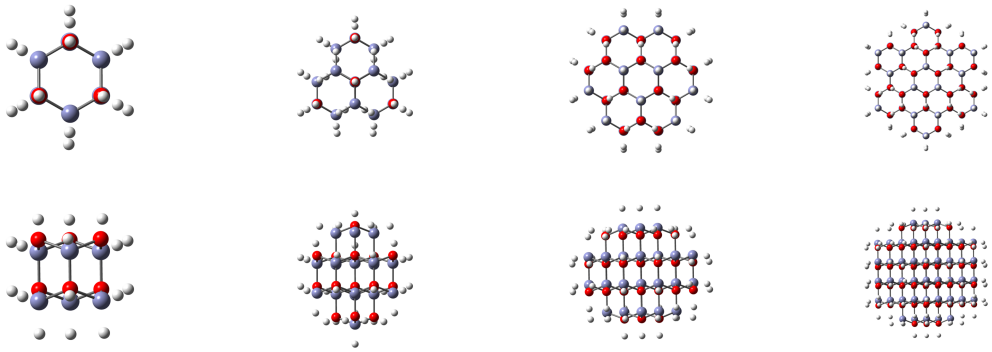

Figure 6.2: The ZnO cluster models used: $(ZnO)_6$, $(ZnO)_{17}$, $(ZnO)_{33}$, $(ZnO)_{84}$.

Table 6.1: The anisotropy ratio between the length of nanocrystals along the C_3 (z) axis and the (x, y) axes.

Size	6	17	33	84
ZnO	0.845	1.301	0.913	0.916

described previously, and PBE0 exchange-correlation functional [124]. The 6-31G(d) basis set [164, 165] was used for all atoms.

To quantify the degree of anisotropy in these model quantum dot systems, the ratio between the length of the nanocrystal along the C_3 axis and perpendicular to it are given in Tab. 6.1. In all nanocrystals except those of size $(ZnO)_{17}$, the hexagonal C_3 axis is shorter than those perpendicular to it. For the nanocrystals of size $(ZnO)_{17}$, the C_3 axis is longer.

6.4 Results and Discussion

6.4.1 Rashba Effects on Frontier Orbitals

The computed densities of states using molecular orbitals are plotted in Fig. 6.3, and show the smoothing out of discrete states of orbitals into bands as the nanocrystal size is increased.

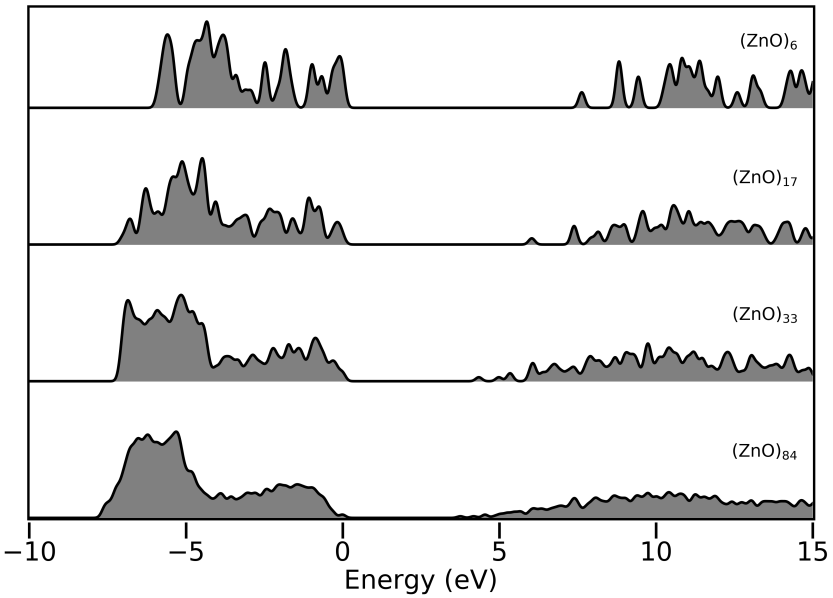

Figure 6.3: Computed total densities of states for ZnO quantum dots of increasing size, shifted so the HOMO lies at 0 eV.

The bandgap decreases with increasing nanocrystal size, as expected. The molecular orbitals at the band edges are shown in Fig. 6.4. In the absence of spin-orbit coupling (Rashba effect), both the HOMO and HOMO-1 spinor orbitals are degenerate with an E symmetry in the C_{3v} point group, while the HOMO-2 having the A_1 symmetry. The orbitals at the conduction band edge appear to be large atomic-like super-orbitals arising from the spherical potential model [197]. The LUMO at the conduction band edge is S-type and LUMO+1 to LUMO+3 are P-type orbitals. If the QDs were perfectly centrosymmetric, we would observe three-fold degenerate P-type orbitals. However, these QDs have a non-centrosymmetric C_{3v} symmetry. A a result, we see a low-symmetry splitting of the P-band into two sublevels, where the higher-energy feature consists of two degenerate (P_x, P_y) orbitals and the lower-energy feature corresponds to P_z orbital.

With the inclusion of spin-orbit coupling we see the symmetry is further reduced because of mixing between frontier spinor orbitals, which now include both α and β spin-components

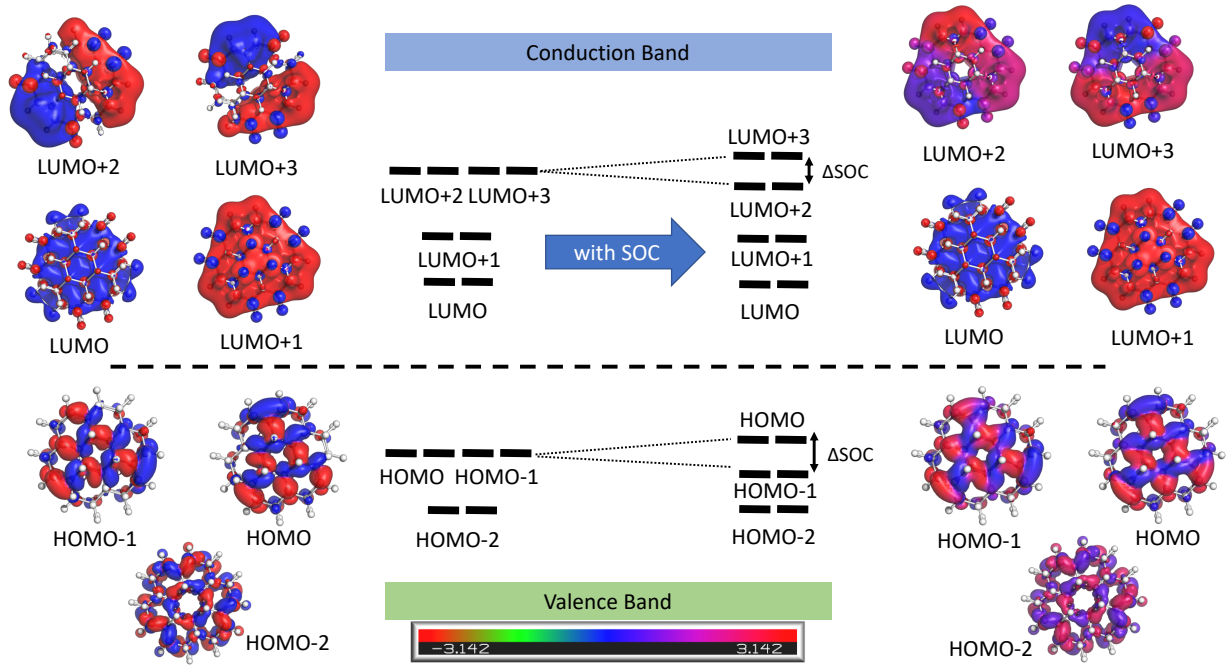

Figure 6.4: The molecular orbital diagram of the valence and conduction band edge levels. Due to Kramers degeneracy, all levels are doubly degenerate so only one of the pair of orbitals is shown. MOs from the $(ZnO)_{33}$ are plotted at an isovalue of 0.007 $a_0^{-3/2}$ for the magnitude and mapped with the angle between α and β spin-components as shown in the color bar. Values of 0 and π are pure α, while values of $\pm\pi/2$ are pure β.

as s is no longer a good quantum number. HOMO and HOMO-1 spinors now belong to the $1S_{3/2}$ manifold with $J = 3/2$, where as HOMO-2 spinors are in the $1S_{1/2}$ level with $J = 1/2$. These variational relativistic calculations show that the inclusion of spin-orbit coupling along with the crystal field and quantum dot anisotropy splits the degenerate E orbitals into two subgroups of $1S_{3/2}$ with different magnetic projections, $M_J = \pm 3/2$ and $M_J = \pm 1/2$, respectively. These correspond to the "heavy" and "light" hole levels in band theory, due to their different effective masses.

A quantitative energy level diagram for the ZnO nanocrystals is given in Fig. 6.5. Of

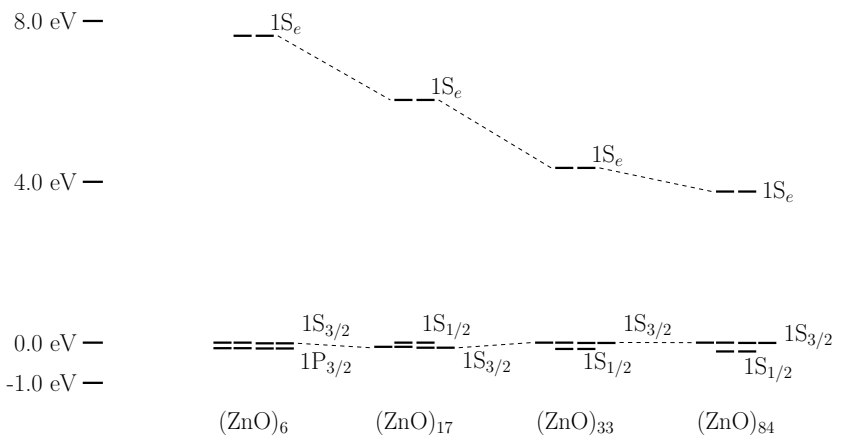

Figure 6.5: Energy level diagram for the main states involved in the band-edge excitons of ZnO nanocrystals. Dashed lines connect the $1S_{3/2}$ levels in the valence band as well as the $1S_e$ levels in the conduction band. In the smallest cluster the $1S_{1/2}$ manifold is deeper in the valence band edge so the level below the $1S_{3/2}$ is the $1P_{3/2}$.

particular note is the different orderings between levels comprising the $J = 3/2$ and $J = 1/2$ manifolds. It is well-known that the energetic ordering of different J manifolds is very sensitive to the shape of the confining potential [217]. For the ZnO quantum dots, spin-orbit coupling is relatively small, so crystal field effects and crystal anisotropy play an outsized role compared to other types of II-VI nanocrystals where spin-orbit effects would be larger. In the bulk-like systems, the highest-lying valence band levels are the $1S_{3/2}$ and $1S_{1/2}$ manifolds, respectively. This is the structure seen in the larger $(ZnO)_{33}$ and $(ZnO)_{84}$ nanocrystals, in which the $1S_{3/2}$ is above the $1S_{1/2}$. For the smaller dots, deviations from this usual pattern are observed. In the $(ZnO)_{17}$ cluster, a reversed level structure is seen in which the $1S_{1/2}$ level actually moves above the $1S_{3/2}$ because the crystal field acts with the opposite sign due to the C_3 axis being elongated rather than shortened. For the smallest cluster, $(ZnO)_6$, the $1S_{1/2}$ manifold is further inside from the valence band edge so that the $1P_{3/2}$ level is immediately below the $1S_{3/2}$. Since the splitting between the distinct angular-momentum

Table 6.2: The magnitude of Rashba-induced splitting in valence band states in undoped ZnO quantum dots, both within the $S_{3/2}$ manifold and between the $S_{3/2}$ and $S_{1/2}$ manifolds (in units of eV).

Size	Within $S_{3/2}$	Between $S_{3/2}$ and $S_{1/2}$
6	0.017	0.134
17	0.022	0.115
33	0.008	0.153
84	0.007	0.266

manifolds in the valence band is most important to understanding the band-edge excitonic features, we focus on the magnitude of the splitting in the valence band and tabulate these values in Tab. 6.2. The splitting within the $1S_{3/2}$ manifold is the difference between "light" and "heavy" holes. Although there is no clear trend in the data, the ZnO results suggest the magnitude of shape anisotropy and the strength of the crystal field strongly influence the Rashba effect within the $S_{3/2}$ manifold.

6.4.2 Rashba Effects on Effective Mass

$\mathbf{k} \cdot \mathbf{p}$ theory and the effective mass model have been useful for describing the energetics and spin-orbit coupling of nanocrystals that are more bulk-like [203, 218]. The effective masses of the electrons and holes can be calculated from the *ab initio* band structure by fitting them to an appropriate model. In the case of nanocrystals that are confined in all directions, the particle in a sphere model has been used [197, 199]. In this model the energy levels depend on quantum numbers n and l and are given by

$$E_{n,l} = \frac{\beta_{n,l}^2 \hbar^2}{2m_e^* R^2} \tag{6.3}$$

where R is the radius of the nanocrystal, m_e^* is the effective mass, and $\beta_{n,l}$ is the nth zero of the lth spherical Bessel function. The first four levels, $1S$, $1P$, $1D$, and $2S$, were used to fit

Table 6.3: The calculated effective masses of electrons and holes, Bohr radii, and binding energies E_b for ZnO quantum dots.

	Without spin-orbit				With spin-orbit			
Molecule	m_h^*	m_e^*	Bohr radius	E_b (eV)	m_h^*	m_e^*	Bohr radius	E_b (eV)
$(ZnO)_6$	5.972	3.814	3.65	0.877	5.932	3.814	3.66	0.874
$(ZnO)_{18}$	4.597	1.878	6.37	0.502	4.589	1.877	6.38	0.502
$(ZnO)_{33}$	3.396	1.286	9.11	0.351	3.372	1.285	9.13	0.350
$(ZnO)_{84}$	1.631	0.813	15.66	0.204	1.621	0.813	15.70	0.204

the effective masses for both the valence band maximum and conduction band minimum.

The effective masses are also related to the size of the exciton. Assuming a dielectric constant $\epsilon = 8.5$ for ZnO [219], the Bohr radius r_B for the exciton can be estimated as [220]

$$r_B = \epsilon \left(\frac{1}{m_h^*} + \frac{1}{m_e^*} \right) \tag{6.4}$$

Additionally, the exciton binding energies E_b can be estimated from the model and are given by

$$E_b = \frac{e^2}{\epsilon r_B} = \frac{m^*}{\epsilon^2} \tag{6.5}$$

where e is the electron charge (1 in atomic units) and m^* the effective reduced mass.

The estimated values for the ZnO nanocrystals are given in Tab. 6.3. As a broad trend, the effective mass of the both the hole and electron sharply decrease with increasing nanocrystal size. The spin-orbit interaction has a larger effect on the valence band than conduction band, consistent with previous studies that show the effective field due to spin-orbit coupling is different for electrons and holes [202]. These data also suggest that the spin-orbit interaction lowers the average effective mass for the hole states. As expected from the decreased effective mass of the holes, the spin-orbit interaction slightly increases the size of exciton.

6.4.3 Optical Transitions and Exciton Splitting

Quantum confinement and the Rashba effect are also manifested in the linear absorption spectrum. While the quantum confinement effect is known to blue-shift the first bright excitation with decreasing nanocrystal size, it also affects spin-orbit coupling and causes a mixing of the excitonic levels.[217, 221] Rashba effect and crystalline anisotropy split the first exciton, denoted as $1S_{3/2}1S_e$, into sublevels that are sensitive to the quantum confinement. Spin-orbit coupling associated with the $1S_{3/2} \rightarrow 1S_e$ excitation gives rise to two manifolds of the $1S_{3/2}1S_e$ excitons, $J = 2, 1$ with 5- and 3-fold degeneracy, respectively. Crystalline anisotropy further splits states that have different magnetic quantum numbers, *e.g.* $M_J = \pm 2, \pm 1, 0$ for the $J = 2$ manifold and $M_J = \pm 1, 0$ for the $J = 1$ manifold. States that are split from the $J = 2$ (or $J = 1$) manifold are denoted as "L" (or "U") for "Lower" and "Upper" energy groups.

The computed exciton fine structure for the $(ZnO)_{33}$ quantum dot is assigned as given in Tab. 6.4. According to the selection rule in $\mathbf{k} \cdot \mathbf{p}$ theory for bulk materials [204], only the $\pm 1^U$, $\pm 1^L$, and 0^U sublevels are optically allowed transitions, and $\pm 2^L$ and 0^L sublevels are forbidden. The computed results for quantum dots suggest that optical transition selection rules for period bulk system are also maintained in finite, quantum confined structures. The strongest allowed excitonic transition is to the $\pm 1^U$ states that are above 6 lower-lying forbidden or weakly allowed transitions.

The ordering of $1S_{3/2}1S_e$ sublevels strongly depends on the relative strength of crystalline anisotropy and Rashba effect. In quantum confined systems, strong crystalline anisotropy can lead to large splittings. Of particular note for the $(ZnO)_{33}$ quantum dot, the 0^U level is split enough from the "Upper" group that it overlaps with the states from the lower manifold.

For the smaller $(ZnO)_{17}$ nanocrystal (Tab. 6.5), the higher degree of anisotropy leads to a much stronger crystal field relative to the strength of spin-orbit coupling. As a result, the 0^U level actually drops below the 0^L sublevel, so that the lowest-energy exciton is now optically active. In the smallest $(ZnO)_6$ crystal, the magnitude of crystal field anisotropy is

Table 6.4: The exciton fine structure for $(ZnO)_{33}$ quantum dots.

Sublevel	Excitation energy (eV)	Oscillator Strength
0^L	3.677	0.0000
0^U	3.677	0.0001
$\pm 1^L$	3.681	0.0003
$\pm 2^L$	3.686	0.0000
$\pm 1^U$	3.738	0.0384

Table 6.5: The exciton fine structure for $(ZnO)_{17}$ quantum dots.

Sublevel	Excitation energy (eV)	Oscillator Strength
0^U	4.938	0.0007
0^L	4.941	0.0000
$\pm 1^L$	4.951	0.0003
$\pm 2^L$	4.962	0.0000
$\pm 1^U$	5.191	0.1484

lower again, so that the 0^L dark exciton is the lowest energy, as given in Tab. 6.6.

These results are shown graphically in Fig. 6.6. The oscillator strength is almost completely localized in the $\pm 1^U$ transitions, with lowered transition strength in the other optically active modes. This agrees with other work in the literature, which shows the oscillator strength of the $\pm 1^L$ transitions decaying to zero for small nanocrystal radius and being redistributed into the $\pm 1^U$ manifold [222].

In Tab. 6.7, the splittings within and between the different angular-momentum manifolds are given. While the splitting between sublevels with different M_J projections in the lower manifold Δ_L has a strong dependence on the crystal field, the splitting in the upper manifold

Table 6.6: The exciton fine structure for $(ZnO)_6$ quantum dots.

Sublevel	Excitation energy (eV)	Oscillator Strength
0^L	6.116	0.0000
0^U	6.117	0.0001
$\pm 1^L$	6.124	0.0001
$\pm 2^L$	6.133	0.0000
$\pm 1^U$	6.464	0.1057

Table 6.7: Computed fine structure splittings in ZnO quantum dots (in eV). Δ_L is the splitting in the lower manifold, Δ_U is the splitting in the upper manifold, and Δ_{U-L} is the splitting between the mean energy of the two manifolds.

Nanocrystal	Δ_L	Δ_U	Δ_{U-L}
$(ZnO)_6$	0.008	0.347	0.1662
$(ZnO)_{17}$	0.010	0.253	0.1132
$(ZnO)_{33}$	0.005	0.061	0.0262

Δ_U and between the mean energies of the two manifolds Δ_{U-L} has a strong dependence on the nanocrystal size. One reason for this difference in exciton manifolds is that the heavy holes with $M_J = \pm 3/2$ feel both "short"- and "long"-range exchange, while the light holes with $M_J = \pm 1/2$ only feel "short"-range exchange [204]. This difference is enhanced as the nanocrystals are more confined.

In Fig. 6.7 the computed absorption spectra are plotted, both with and without the inclusion of spin-orbit coupling. All peaks are broadened with a Lorenztian lineshape with a FWHM of 0.005 eV. Analysis of the transition amplitudes shows that the band-edge excitons are indeed well-described by a hole in the $1S_{3/2}$ manifold and an electron in the $1S_e$ level,

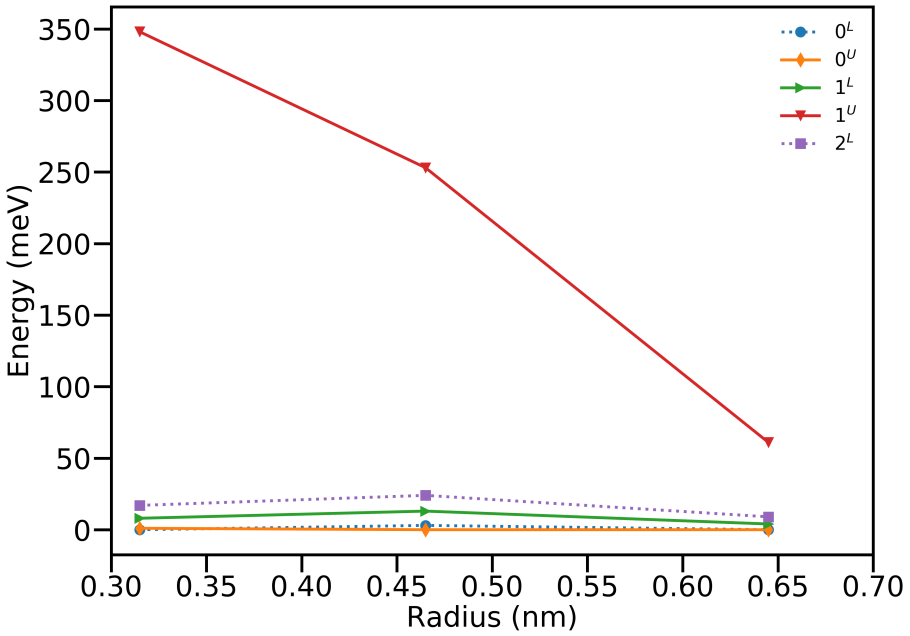

Figure 6.6: The exciton fine structure levels for ZnO quantum dots. The lowest energy state is set to zero.

though this analysis also shows some mixing with deeper valence band states than those depicted in the diagram given in Fig. 6.4. In the case of the $(ZnO)_{17}$ cluster, the transition amplitudes and resulting NTO eigenvalues given in Tab. 6.8 show about 4% contribution from lower-lying bands, however the simple picture of a single-particle excitation from the $1S_{3/2}$ levels in the valence band is still largely true, with nearly 96% recovered in the dominant NTOs. The NTOs for the first bright excited state are plotted in Fig. 6.8. Transition from O $2p$ orbitals goes into an s-like superorbital delocalized over the entire cluster, consistent with the previous model.

6.5 Conclusions

In this work, we have performed *ab initio* electronic structure calculations that incorporate relativistic effects to demonstrate the effect of quantum confinement on spin-orbit coupling

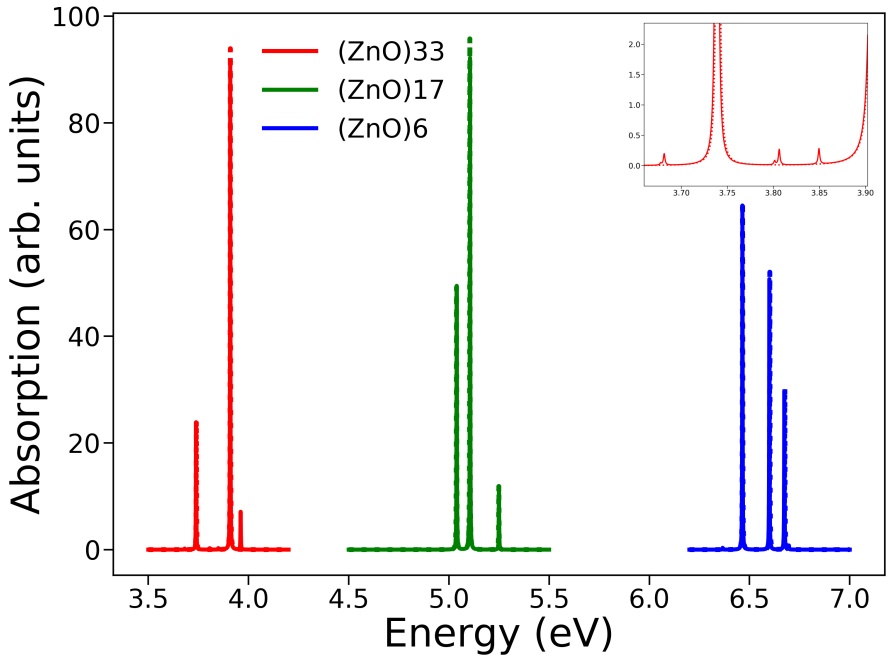

Figure 6.7: The optical absorption spectra of ZnO quantum dots calculated by TDDFT. The dashed lines indicate spin-orbit free calculations, while the solid traces include spin-orbit coupling. The inset shows a zoom-in on the $(ZnO)_{33}$ features, where dark states gain intensity under spin-orbit coupling by singlet-triplet mixing.

that affects the band-edge excitonic manifold in ZnO quantum dots. This allows for the study of the Rashba effect in small, highly quantum-confined systems where the band model used in $\mathbf{k} \cdot \mathbf{p}$ theory can break down. In particular, we have found that the "Upper" and "Lower" exciton manifolds can mix and overlap in small ZnO nanocrystals, where already small spin-orbit coupling is further reduced by symmetry-lowering crystal field effects. The cluster models used here can easily be adapted to explore the role of surface and ligand modifications, dopants, and other defects on the ground state electronic structure and fine structure of the excitonic manifold.

Table 6.8: MO transition amplitudes for the first bright excited state in undoped $(ZnO)_{17}$.

MOs	Amplitude (%)
HOMO-17 $\rightarrow$ LUMO+1	1.99
HOMO-16 $\rightarrow$ LUMO	1.99
HOMO-1 $\rightarrow$ LUMO	18.82
HOMO-1 $\rightarrow$ LUMO+1	25.92
HOMO $\rightarrow$ LUMO	25.92
HOMO $\rightarrow$ LUMO+1	18.92
NTO 1:	$\lambda = 0.481$
NTO 2:	$\lambda = 0.481$

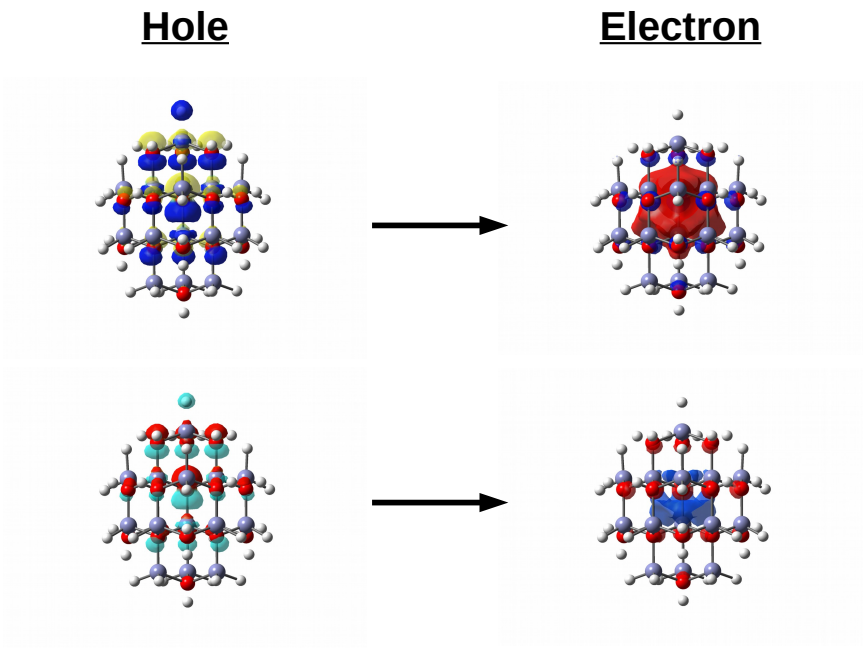

Figure 6.8: The NTOs of the first bright excited state in $(ZnO)_{17}$. There are two sets of orbitals (top and bottom), corresponding to the α and β spins.

BIBLIOGRAPHY

[1] A. T. Wen and A. P. Hitchcock. Inner-Shell Spectroscopy of $(\eta^5\text{-}C_5H_5)_2TiCl_2$, $(\eta^5\text{-}C_5H_5)TiCl_3$, and $TiCl_4$. *Can. J. Chem.*, 71(10):1632–1644, Oct. 1993.

[2] J. Bozek, K. Tan, G. Bancroft, and J. Tse. High Resolution Gas Phase Photoabsorption Spectra of $SiCl_4$ and $Si(CH3)_4$ at the Silicon L Edges: Characterization and Assignment of Resonances. *Chem. Phys. Lett.*, 138(1):33–42, 1987.

[3] G. Fronzoni, M. Stener, P. Decleva, M. de Simone, M. Coreno, P. Franceschi, C. Furlani, and K. C. Prince. X-ray Absorption Spectroscopy of $VOCl_3$, CrO_2Cl_2, and MnO_3Cl: An Experimental and Theoretical Study. *J. Phys. Chem. A*, 113(12):2914–2925, 2009.

[4] E. C. Wasinger, F. M. De Groot, B. Hedman, K. O. Hodgson, and E. I. Solomon. L-edge X-ray Absorption Spectroscopy of Non-Heme Iron Sites: Experimental Determination of Differential Orbital Covalency. *J. Am. Chem. Soc.*, 125(42):12894–12906, 2003.

[5] M. J. Frisch, G. W. Trucks, H. B. Schlegel, G. E. Scuseria, M. A. Robb, J. R. Cheeseman, G. Scalmani, V. Barone, G. A. Petersson, H. Nakatsuji, X. Li, M. Caricato, A. V. Marenich, J. Bloino, B. G. Janesko, R. Gomperts, B. Mennucci, H. P. Hratchian, J. V. Ortiz, A. F. Izmaylov, J. L. Sonnenberg, D. Williams-Young, F. Ding, F. Lipparini, F. Egidi, J. Goings, B. Peng, A. Petrone, T. Henderson, D. Ranasinghe, V. G. Zakrzewski, J. Gao, N. Rega, G. Zheng, W. Liang, M. Hada, M. Ehara, K. Toyota, R. Fukuda, J. Hasegawa, M. Ishida, T. Nakajima, Y. Honda, O. Kitao, H. Nakai, T. Vreven, K. Throssell, J. A. Montgomery, Jr., J. E. Peralta, F. Ogliaro, M. J. Bearpark, J. J. Heyd, E. N. Brothers, K. N. Kudin, V. N. Staroverov, T. A. Keith, R. Kobayashi, J. Normand, K. Raghavachari, A. P. Rendell, J. C. Burant, S. S. Iyengar, J. Tomasi, M. Cossi, J. M. Millam, M. Klene, C. Adamo, R. Cammi, J. W.

Ochterski, R. L. Martin, K. Morokuma, O. Farkas, J. B. Foresman, and D. J. Fox. Gaussian Development Version Revision I.11+.

[6] D. B. Williams-Young, A. Petrone, S. Sun, T. F. Stetina, P. Lestrange, C. E. Hoyer, D. R. Nascimento, L. Koulias, A. Wildman, J. Kasper, J. J. Goings, F. Ding, A. E. DePrince III, E. F. Valeev, and X. Li. The Chronus Quantum Software Package. *WIREs Comput. Mol. Sci.*, 10(2):e1436, 2020.

[7] A. Szabo and N. S. Ostlund. *Modern Quantum Chemistry: Introduction to Advanced Electronic Structure Theory*. Dover Publications, Mineola, N.Y., 1996.

[8] P. Hohenberg and W. Kohn. Inhomogeneous Electron Gas. *Phys. Rev.*, 136:B864–B871, 1964.

[9] K. G. Dyall and K. Faegri Jr. *Introduction to Relativistic Quantum Chemistry*. Oxford University Press, 2007.

[10] M. Reiher and A. Wolf. *Relativistic Quantum Chemistry*. Wiley-VCH, 2015.

[11] P. Pyykkö. Relativistic Effects in Chemistry: More Common Than You Thought. *Annu. Rev. Phys. Chem.*, 63:45–64, 2012.

[12] W. Kutzlenigg and W. Liu. Quasirelativistic Theory Equivalent to Fully Relativistic Theory. *J. Chem. Phys.*, 123:241102, 2005.

[13] W. Liu and D. Peng. Infinite-Order Quasirelativistic Density Functional Method Based on the Exact Matrix Quasirelativistic Theory. *J. Chem. Phys.*, 125:044102, 2006.

[14] M. Ilias and T. Saue. An Infinite-Order Relativistic Hamiltonian by a Simple One-Step Transformation. *J. Chem. Phys.*, 126:064102, 2007.

[15] W. Liu and D. Peng. Exact Two-Component Hamiltonians Revisited. *J. Chem. Phys.*, 131(3):031104, 2009.

[16] D. Peng, W. Liu, Y. Xiao, and L. Cheng. Making Four- and Two-Component Relativistic Density Functional Methods Fully Equivalent Based on the Idea of From Atoms to Molecule. *J. Chem. Phys.*, 127:104106, 2007.

[17] D. Peng, N. Middendorf, F. Weigend, and M. Reiher. An Efficient Implementation of Two-Component Relativistic Exact-Decoupling Methods for Large Molecules. *J. Chem. Phys.*, 138:184105, 2013.

[18] W. Liu. Ideas of Relativistic Quantum Chemistry. *Mol. Phys.*, 108:1679–1706, 2010.

[19] T. Saue. Relativistic Hamiltonians for Chemistry: A Primer. *ChemPhysChem*, 12:3077–3094, 2011.

[20] W. Liu. Advances in Relativistic Molecular Quantum Mechanics. *Phys. Rep.*, 537:59–89, 2014.

[21] W. Liu. The Big Picture of Relativistic Molecular Quantum Mechanics. *Natl. Sci. Rev.*, 3(2):204–221, 2016.

[22] K. G. Dyall. Interfacing Relativistic and Nonrelativistic Methods. I. Normalized Elimination of the Small Component in the Modified Dirac Equation. *J. Chem. Phys.*, 106(23):9618–9626, 1997.

[23] K. G. Dyall. Interfacing Relativistic and Nonrelativistic Methods. II. Investigation of a Low-Order Approximation. *J. Chem. Phys.*, 109:4201–4208, 1998.

[24] K. G. Dyall and T. Enevoldsen. Interfacing Relativistic and Nonrelativistic Methods. III. Atomic 4-Spinor Expansions and Integral Approximations. *J. Chem. Phys.*, 111:10000–10007, 1999.

[25] K. G. Dyall. Interfacing Relativistic and Nonrelativistic Methods. II. One- and Two-Electron Scalar Approximations. *J. Chem. Phys.*, 115:9136–9143, 2001.

[26] M. Filatov and D. Cremer. A New Quasi-Relativistic Approach for Density Functional Theory Based on the Normalized Elimination of the Small Component. *Chem. Phys. Lett.*, 351:259–266, 2002.

[27] M. Douglas and N. M. Kroll. Quantum Electrodynamical Corrections to the Fine Structure of Helium. *Ann. Phys.*, 82:89–155, 1974.

[28] B. A. Hess. Applicability of the No-Pair Equation with Free-Particle Projection Operators to Atomic and Molecular Structure Calculations. *Phys. Rev. A*, 32:756–763, 1985.

[29] B. A. Hess. Relativistic Electronic-Structure Calculations Employing a Two-Component No-Pair Formalism with External-Field Projection Operators. *Phys. Rev. A*, 33:3742–3748, 1986.

[30] R. Samzow, B. A. Hess, and G. Jansen. The Two-Electron Terms of the Nopair Hamiltonian. *J. Chem. Phys.*, 96:1227–1231, 1992.

[31] E. van Lenthe, E. J. Baerends, and J. G. Snijders. Relativistic Regular Two-Component Hamiltonians. *J. Chem. Phys.*, 99:4597–4610, 1993.

[32] E. van Lenthe, E. J. Baerends, and J. G. Snijders. Relativistic Total Energy Using Regular Approximations. *J. Chem. Phys.*, 101:9783–9792, 1994.

[33] C. van Wüllen. Molecular Density Functional Calculations in the Regular Relativistic Approximation: Method, Application to Coinage Metal Diatomics, Hydrides, Fluorides and Chlorides, and Comparison with First-Order Relativistic Calculations. *J. Chem. Phys.*, 109:392–399, 1998.

[34] J. Gao, W. Zou, W. Liu, Y. Xiao, D. Peng, B. Song, and C. Liu. Time-Dependent Four-Component Relativistic Density-Functional Theory for Excitation Energies. II. The Exchange-Correlation Kernel. *J. Chem. Phys.*, 123:054102, 2005.

[35] R. Bast, H. J. A. Jensen, and T. Saue. Relativistic Adiabatic Time-Dependent Density Functional Theory Using Hybrid Functionals and Noncollinear Spin Magnetization. *Int. J. Quant. Chem.*, 109:2091–2112, 2009.

[36] F. Wang, T. Ziegler, E. van Lenthe, S. van Gisbergen, and E. J. Baerends. The Calculation of Excitation Energies Based on the Relativistic Two-Component Zeroth-Order Regular Approximation and Time-Dependent Density-Functional with Full Use of Symmetry. *J. Chem. Phys.*, 122(20):204103, 2005.

[37] M. Kühn and F. Weigend. Implementation of Two-Component Time-Dependent Density Functional Theory in TURBOMOLE. *J. Chem. Theory Comput.*, 9(12):5341–5348, 2013.

[38] A. Nakata, T. Tsuneda, and K. Hirao. Spin-Orbit Relativistic Long-Range Corrected Time-Dependent Density Functional Theory for Investigating Spin-Forbidden Transitions in Photochemical Reactions. *J. Chem. Phys.*, 135(22):224106, 2011.

[39] F. Egidi, J. J. Goings, M. J. Frisch, and X. Li. Direct Atomic-Orbital-Based Relativistic Two-Component Linear Response Method for Calculating Excited-State Fine Structures. *J. Chem. Theory Comput.*, 12(8):3711–3718, 2016.

[40] J. Gao, , W. Liu, B. Song, and C. Liu. Time-Dependent Four-Component Relativistic Density Functional Theory for Excitation Energies. *J. Chem. Phys.*, 121:6658–6666, 2004.

[41] D. Peng, W. Zou, and W. Liu. Time-Dependent Quasirelativistic Density-Functional Theory Based on the Zeroth-Order Regular Approximation. *J. Chem. Phys.*, 123:144101, 2005.

[42] W. Xu, J. Ma, D. Pen, W. Zou, W. Liu, and V. Staemmler. Excited States of ReO_4^-: A Comprehensive Time-Dependent Relativistic Density Functional Theory Study. *Chem. Phys.*, 356:219–228, 2009.

[43] W. Xu, Y. Zhang, and W. Liu. Time-Dependent Relativistic Density Functional Study of Yb and YbO. *Sci. China Ser. B Chem.*, 52:1945–1953, 2009.

[44] Y. Zhang, W. Xu, Q. Sun, W. Zou, and W. Liu. Excited States of OsO_4: A Comprehensive Time-Dependent Relativistic Density Functional Theory Study. *J. Comput. Chem.*, 31:532–551, 2010.

[45] Z. Li, B. Suo, Y. Zhang, Y. Xiao, and W. Liu. Combining Spin-Adapted Open-Shell TD-DFT with Spin–Orbit Coupling. *Mol. Phys.*, 111(24):3741–3755, 2013.

[46] X. Li, S. M. Smith, A. N. Markevitch, D. A. Romanov, R. J. Levis, and H. B. Schlegel. A Time-Dependent Hartree-Fock Approach for Studying the Electronic Optical Response of Molecules in Intense Fields. *Phys. Chem. Chem. Phys.*, 7:233–239, 2005.

[47] K. Lopata and N. Govind. Modeling Fast Electron Dynamics With Real-Time Time-Dependent Density Functional Theory: Application to Small Molecules and Chromophores. *J. Chem. Theory Comput.*, 7(5):1344–1355, 2011.

[48] F. Ding, J. J. Goings, M. J. Frisch, and X. Li. Ab Initio Non-Relativistic Spin Dynamics. *J. Chem. Phys.*, 141(21):214111, 2014.

[49] M. Repisky, L. Konecny, M. Kadek, S. Komorovsky, O. L. Malkin, V. G. Malkin, and K. Ruud. Excitation Energies from Real-Time Propagation of the Four-Component Dirac–Kohn–Sham Equation. *J. Chem. Theory Comput.*, 11(3):980–991, 2015.

[50] F. Ding, J. J. Goings, H. Liu, D. B. Lingerfelt, and X. Li. Ab Initio Two-Component Ehrenfest Dynamics. *J. Chem. Phys.*, 143:114105, 2015.

[51] J. C. Boettger. Approximate Two-Electron Spin-Orbit Coupling Term For Density-Functional-Theory DFT Calculations Using The Douglas-Kroll-Hess Transformation. *Phys. Rev. B*, 62:7809–7815, 2000.

[52] F. Wang and W. Liu. Comparison of Different Polarization Schemes in Open-Shell Relativistic Density Functional Calculations. *J. Chin. Chem. Soc. Taip.*, 50:597–606, 2003.

[53] C. van Wüllen. Spin Densities in Two-Component Relativistic Density Functional Calculations: Noncollinear Versus Collinear Approach. *J. Comput. Chem.*, 23(8):779–785, 2002.

[54] J. E. Peralta, G. E. Scuseria, and M. J. Frisch. Noncollinear Magnetism in Density Functional Calculations. *Phys. Rev. B*, 75:125119, 2007.

[55] G. Scalmani and M. J. Frisch. A New Approach to Noncollinear Spin Density Functional Theory Beyond the Local Density Approximation. *J. Chem. Theory Comput.*, 8:2193, 2012.

[56] I. W. Bulik, G. Scalmani, M. J. Frisch, and G. E. Scuseria. Noncollinear Density Functional Theory Having Proper Invariance and Local Torque Properties. *Phys. Rev. B*, 87:035117, 2013.

[57] K. Capelle, G. Vignale, and B. Györffy. Spin Currents and Spin Dynamics in Time-Dependent Density Functional Theory. *Phys. Rev. Lett.*, 87:206403, 2001.

[58] C. M. Isborn, X. Li, and J. C. Tully. Time-Dependent Density Functional Theory Ehrenfest Dynamics: Collisions Between Atomic Oxygen and Graphite Clusters. *J. Chem. Phys.*, 126:134307, 2007.

[59] W. Liang, C. T. Chapman, and X. Li. Efficient First-Principles Electronic Dynamics. *J. Chem. Phys.*, 134(18):184102, 2011.

[60] F. Ding, W. Liang, C. T. Chapman, C. M. Isborn, and X. Li. On the Gauge Invariance of Nonperturbative Electronic Dynamics Using the Time-Dependent Hartree-Fock and Time-Dependent Kohn-Sham. *J. Chem. Phys.*, 135(16):164101, 2011.

[61] A. Wolf and M. Reiher. Exact Decoupling of the Dirac Hamiltonian. III. Molecular Properties. *J. Chem. Phys.*, 121:064102, 2004.

[62] J. C. Slater. A Simplification of the Hartree–Fock Method. *Phys. Rev.*, 81(3):385, 1951.

[63] S. Vosko, L. Wilk, and M. Nusair. Accurate Spin-Dependent Electron Liquid Correlation Energies for Local Spin Density Calculations: A Critical Analysis. *Can. J. Phys.*, 58(8):1200–1211, 1980.

[64] T. Noro, M. Sekiya, and T. Koga. Segmented Contracted Basis Sets for Atoms H through Xe: Sapporo-(DK)-nZP Sets (n = D, T, Q). *Theor. Chem. Acc.*, 131:1124, 2012.

[65] A. Bruner, D. LaMaster, and K. Lopata. Accelerated Broadband Spectra using Transition Dipole Decomposition and Padé Approximants. *J. Chem. Theory Comput.*, 12(8):3741–3750, 2016.

[66] J. Sansonetti and W. Martin. Handbook of Basic Atomic Spectroscopic Data. *J. Phys. Chem. Ref. Data*, 34(4):1559–2259, 2005.

[67] K. P. Huber and G. Herzberg. *Constants of Diatomic Molecules*. Van Nostrand Reinhold, New York, 1979.

[68] W. Gu, H. Wang, and K. Wang. Nickel L-edge and K-edge X-ray Absorption Spectroscopy of Non-Innocent Ni$[S_2C_2(CF_3)_2]_2^n$ Series (N = -2, -1, 0): Direct Probe of Nickel Fractional Oxidation State Changes. *Dalton Trans.*, 43(17):6406–6413, 2014.

[69] S. Hulbert, B. Bunker, F. Brown, and P. Pianetta. Copper $L_{2,3}$ Near-Edge Structure in Cu_2O. *Phys. Rev. B*, 30(4):2120, 1984.

[70] E. Kleymenov, J. A. van Bokhoven, C. David, P. Glatzel, M. Janousch, R. Alonso-Mori, M. Studer, M. Willimann, A. Bergamaschi, B. Henrich, and M. Nachtegaal. Five-

Element Johann-Type X-ray Emission Spectrometer with a Single-Photon-Counting Pixel Detector. *Rev. Sci. Instrum.*, 82(6):065107, 2011.

[71] I. Llorens, E. Lahera, W. Delnet, O. Proux, A. Braillard, J.-L. Hazemann, A. Prat, D. Testemale, Q. Dermigny, F. Gélébart, M. Morand, A. Shukla, N. Bardou, O. Ulrich, S. Arnaud, J.-F. Berar, N. Boudet, B. Caillot, P. Chaurand, J. Rose, E. Doelsch, P. Martin, and P. Solari. High Energy Resolution Five-Crystal Spectrometer for High Quality Fluorescence and Absorption Measurements on an X-ray Absorption Spectroscopy Beamline. *Rev. Sci. Instrum.*, 83(6):063104, 2012.

[72] M. Kavčič, M. Budnar, A. Mühleisen, F. Gasser, M. Žitnik, K. Bučar, and R. Bohinc. Design and Performance of a Versatile Curved-Crystal Spectrometer for High-Resolution Spectroscopy in the Tender X-ray Range. *Rev. Sci. Instrum.*, 83(3):033113, 2012.

[73] G. Seidler, D. Mortensen, A. Remesnik, J. Pacold, N. Ball, N. Barry, M. Styczinski, and O. Hoidn. A Laboratory-Based Hard X-ray Monochromator for High-Resolution X-ray Emission Spectroscopy and X-ray Absorption Near Edge Structure Measurements. *Rev. Sci. Instrum.*, 85(11):113906, 2014.

[74] D. R. Mortensen, G. T. Seidler, A. S. Ditter, and P. Glatzel. Benchtop Nonresonant X-ray Emission Spectroscopy: Coming Soon to Laboratories and XAS Beamlines Near You. In *J. Phys. Conf. Ser.*, volume 712, page 012036, 2016.

[75] G. Fronzoni, R. De Francesco, and M. Stener. Time Dependent Density Functional Theory of X-ray Absorption Spectroscopy of Alkaline-Earth Oxides. *J. Phys. Chem. B*, 109(20):10332–10340, 2005.

[76] S. DeBeer George, T. Petrenko, and F. Neese. Time-Dependent Density Functional Calculations of Ligand K-edge X-ray Absorption Spectra. *Inorg. Chim. Acta*, 361(4):965–972, 2008.

[77] N. A. Besley and F. A. Asmuruf. Time-Dependent Density Functional Theory Calculations of the Spectroscopy of Core Electrons. *Phys. Chem. Chem. Phys.*, 12(38):12024–12039, 2010.

[78] P. J. Lestrange, P. D. Nguyen, and X. Li. Calibration of Energy-Specific TDDFT for Modeling K-Edge XAS Spectra of Light Elements. *J. Chem. Theory Comput.*, 11:2994–2999, 2015.

[79] B. Peng, P. J. Lestrange, J. J. Goings, M. Caricato, and X. Li. Energy-Specific Equation-of-Motion Coupled-Cluster Methods for High-Energy Excited States: Application to K-Edge X-Ray Absorption Spectroscopy. *J. Chem. Theory Comput.*, 11(9):4146–4153, 2015.

[80] J. Stöhr. *NEXAFS Spectroscopy*. Springer-Verlag, 2003.

[81] S. Bernadotte, A. J. Atkins, and C. R. Jacob. Origin-Independent Calculation of Quadrupole Intensities in X-ray Spectroscopy. *J. Chem. Phys.*, 137(20):204106, 2012.

[82] N. H. List, J. Kauczor, T. Saue, H. J. A. Jensen, and P. Norman. Beyond the Electric-dipole Approximation: A Formulation and Implementation of Molecular Response Theory for the Description of Absorption of Electromagnetic Field Radiation. *J. Chem. Phys.*, 142(24):244111, 2015.

[83] P. J. Lestrange, F. Egidi, and X. Li. The Consequences of Improperly Describing Oscillator Strengths Beyond the Electric Dipole Approximation. *J. Chem. Phys.*, 143:234103, 2015.

[84] L. K. Sørensen, M. Guo, R. Lindh, and M. Lundberg. Applications to Metal K Pre-edges of Transition Metal Dimers Illustrate the Approximate Origin Independence for the Intensities in the Length Representation. *Mol. Phys.*, pages 1–16, 2016.

[85] M. Stener, G. Fronzoni, and M. de Simone. Time Dependent Density Functional Theory of Core Electrons Excitations. *Chem. Phys. Lett.*, 373(1-2):115–123, 2003.

[86] K. Ray, S. DeBeer George, E. I. Solomon, K. Wieghardt, and F. Neese. Description of the Ground-State Covalencies of the Bis (dithiolato) Transition-Metal Complexes from X-ray Absorption Spectroscopy and Time-Dependent Density-Functional Calculations. *Chem. Eur. J.*, 13(10):2783–2797, 2007.

[87] W. Liang, S. A. Fischer, M. J. Frisch, and X. Li. Energy-Specific Linear Response TDHF/TDDFT for Calculating High-Energy Excited States. *J. Chem. Theory Comput.*, 7(11):3540–3547, 2011.

[88] K. Lopata, B. E. Van Kuiken, M. Khalil, and N. Govind. Linear-Response and Real-Time Time-Dependent Density Functional Theory Studies of Core-Level Near-Edge X-Ray Absorption. *J. Chem. Theory Comput.*, 8(9):3284–3292, 2012.

[89] R. Van Beeumen, D. B. Williams-Young, J. M. Kasper, C. Yang, E. G. Ng, and X. Li. Model Order Reduction Algorithm for Estimating the Absorption Spectrum. *J. Chem. Theory Comput.*, 13(10):4950–4961, 2017.

[90] R. G. Fernando, M. C. Balhoff, and K. Lopata. X-ray Absorption in Insulators with Non-Hermitian Real-Time Time-Dependent Density Functional Theory. *J. Chem. Theory Comput.*, 11(2):646–654, 2015.

[91] J. Wenzel, M. Wormit, and A. Dreuw. Calculating Core-Level Excitations and X-ray Absorption Spectra of Medium-Sized Closed-Shell Molecules with the Algebraic-Diagrammatic Construction Scheme for the Polarization Propagator. *J. Comput. Chem.*, 35(26):1900–1915, 2014.

[92] J. Wenzel, M. Wormit, and A. Dreuw. Calculating X-ray Absorption Spectra of Open-Shell Molecules With the Unrestricted Algebraic-Diagrammatic Construction Scheme for the Polarization Propagator. *J. Chem. Theory Comput.*, 10(10):4583–4598, 2014.

[93] J. Wenzel, A. Holzer, M. Wormit, and A. Dreuw. Analysis and Comparison of CVS-

ADC Approaches up to Third Order for the Calculation of Core-Excited States. *J. Chem. Phys.*, 142(21):214104, 2015.

[94] S. Coriani, O. Christiansen, T. Fransson, and P. Norman. Coupled-Cluster Response Theory for Near-Edge X-ray-Absorption Fine Structure of Atoms and Molecules. *Phys. Rev. A*, 85(2):022507, 2012.

[95] T. Fransson, S. Coriani, O. Christiansen, and P. Norman. Carbon X-ray Absorption Spectra of Fluoroethenes and Acetone: A Study at the Coupled Cluster, Density Functional, and Static-Exchange Levels of Theory. *J. Chem. Phys.*, 138(12):124311, 2013.

[96] I. Josefsson, K. Kunnus, S. Schreck, A. Föhlisch, F. de Groot, P. Wernet, and M. Odelius. Ab Initio Calculations of X-ray Spectra: Atomic Multiplet and Molecular Orbital Effects in a Multiconfigurational SCF Approach to the L-edge Spectra of Transition Metal Complexes. *J. Phys. Chem. Lett.*, 3(23):3565–3570, 2012.

[97] R. V. Pinjari, M. G. Delcey, M. Guo, M. Odelius, and M. Lundberg. Restricted Active Space Calculations of L-edge X-ray Absorption Spectra: From Molecular Orbitals to Multiplet States. *J. Chem. Phys.*, 141(12):124116, 2014.

[98] M. Roemelt and F. Neese. Excited States of Large Open-Shell Molecules: An Efficient, General, and Spin-Adapted Approach Based on a Restricted Open-Shell Ground State Wave Function. *J. Phys. Chem. A*, 117(14):3069–3083, 2013.

[99] M. Roemelt, D. Maganas, S. DeBeer, and F. Neese. A Combined DFT and Restricted Open-Shell Configuration Interaction Method Including Spin-Orbit Coupling: Application to Transition Metal L-edge X-ray Absorption Spectroscopy. *J. Chem. Phys.*, 138(20):204101, 2013.

[100] M. Kadek, L. Konecny, B. Gao, M. Repisky, and K. Ruud. X-ray Absorption Reso-

nances Near $L_{2,3}$-edges from Real-Time Propagation of the Dirac–Kohn–Sham Density Matrix. *Phys. Chem. Chem. Phys.*, 17(35):22566–22570, 2015.

[101] J. J. Goings, J. M. Kasper, F. Egidi, S. Sun, and X. Li. Real Time Propagation of the Exact Two Component Time-Dependent Density Functional Theory. *J. Chem. Phys.*, 145(10):104107, 2016.

[102] L. Konecny, M. Kadek, S. Komorovsky, O. L. Malkina, K. Ruud, and M. Repisky. Acceleration of Relativistic Electron Dynamics by Means of X2C Transformation: Application to the Calculation of Nonlinear Optical Properties. *J. Chem. Theory Comput.*, 12(12):5823–5833, 2016.

[103] G. Fronzoni, M. Stener, P. Decleva, F. Wang, T. Ziegler, E. Van Lenthe, and E. Baerends. Spin–Orbit Relativistic Time Dependent Density Functional Theory Calculations for the Description of Core Electron Excitations: $TiCl_4$ Case Study. *Chem. Phys. Lett.*, 416(1-3):56–63, 2005.

[104] D. Williams-Young, F. Egidi, and X. Li. Relativistic Two-Component Particle-Particle Tamm-Dancoff Approximation. *J. Chem. Theory Comput.*, 12(11):5379–5384, 2016.

[105] F. Egidi, S. Sun, J. J. Goings, G. Scalmani, M. J. Frisch, and X. Li. Two-Component Non-Collinear Time-Dependent Spin Density Functional Theory for Excited State Calculations. *J. Chem. Theory Comput.*, 13(6):2591–2603, 2017.

[106] J. Anton, B. Fricke, and E. Engel. Noncollinear and Collinear Relativistic Density-functional Program for Electric and Magnetic Properties of Molecules. *Phys. Rev. A*, 69:012505, 2004.

[107] F. Wang and T. Ziegler. Time-Dependent Density Functional Theory Based on a Noncollinear Formulation of the Exchange-Correlation Potential. *J. Chem. Phys.*, 121:12191–12196, 2004.

[108] P. Salek, T. Helgaker, and T. Saue. Linear Response at the 4-Component Relativistic Density-Functional Level: Application to the Frequency-Dependent Dipole Polarizability of Hg, AuH and PtH_2. *Chem. Phys.*, 311:187–201, 2005.

[109] M. Casarin, P. Finetti, A. Vittadini, F. Wang, and T. Ziegler. Spin-Orbit Relativistic Time-Dependent Density Functional Calculations of the Metal and Ligand Pre-Edge XAS Intensities of Organotitanium Complexes: $TiCl_4$, Ti(η^5-C_5H_5)Cl_3, and Ti(η^5-C_5H_5)$_2Cl_2$. *J. Chem. Phys.*, 111:5270, 2007.

[110] A. Devarajan, A. Gaenko, and J. Autschbach. Two-Component Relativistic Density Functional Method for Computing Nonsingular Complex Linear Response of Molecules Based on the Zeroth Order Regular Approximation. *J. Chem. Phys.*, 130:194102, 2009.

[111] F. Eich and E. Gross. Transverse Spin-Gradient Functional for Noncollinear Spin-Density-Functional Theory. *Phys. Rev. Lett.*, 111(15):156401, 2013.

[112] F. Eich, S. Pittalis, and G. Vignale. Transverse and Longitudinal Gradients of the Spin Magnetization in Spin-Density-Functional Theory. *Phys. Rev. B*, 88(24):245102, 2013.

[113] J. J. Goings, F. Egidi, and X. Li. Current Development of Non-Collinear Electronic Structure Theory. *Int. J. Quant. Chem.*, page e25398, 2017.

[114] J. J. Goings, P. J. Lestrange, and X. Li. Real-Time Time-Dependent Electronic Structure Theory. *WIREs Comput. Mol. Sci.*, page DOI:10.1002/wcms.1341, 2017.

[115] S. Tussupbayev, N. Govind, K. Lopata, and C. J. Cramer. Comparison of Real-Time and Linear-Response Time-Dependent Density Functional Theories for Molecular Chromophores Ranging from Sparse to High Densities of States. *J. Chem. Theory Comput.*, 11(3):1102–1109, 2015.

[116] A. D. Becke. Density Functional Thermochemistry. III. The Role of Exact Exchange. *J. Chem. Phys.*, 98:5648–5652, 1993.

[117] P. J. Stephens, F. J. Devlin, C. F. Chabalowski, and M. J. Frisch. Ab Initio Calculation of Vibrational Absorption and Circular Dichroism Spectra Using Density Functional Force Fields. *J. Phys. Chem.*, 98(45):11623–11627, 1994.

[118] T. H. Dunning. Gaussian Basis Sets for Use in Correlated Molecular Calculations. I. The Atoms Boron Through Neon and Hydrogen. *J. Chem. Phys.*, 90(2):1007–1023, 1989.

[119] D. E. Woon and T. H. Dunning, Jr. Gaussian Basis Sets for Use in Correlated Molecular Calculations. III. The Atoms Aluminum Through Argon. *J. Chem. Phys.*, 98(2):1358–1371, 1993.

[120] N. B. Balabanov and K. A. Peterson. Systematically Convergent Basis Sets for Transition Metals. I. All-Electron Correlation Consistent Basis Sets for the 3d Elements Sc-Zn. *J. Chem. Phys.*, 123:064107, 2005.

[121] N. B. Balabanov and K. A. Peterson. Basis Set Limit Electronic Excitation Energies, Ionization Potentials, and Electron Affinities for the 3d Transition Metal Atoms: Coupled Cluster and Multireference Methods. *J. Chem. Phys.*, 125(7):074110, 2006.

[122] A. D. Becke. A New Mixing of Hartree–Fock and Local Density functional Theories. *J. Chem. Phys.*, 98(2):1372–1377, 1993.

[123] C. Adamo and V. Barone. Toward Reliable Density Functional Methods Without Adjustable Parameters: The PBE0 Model. *J. Chem. Phys.*, 110(13):6158–6170, 1999.

[124] J. P. Perdew, K. Burke, and M. Ernzerhof. Generalized Gradient Approximation Made Simple. *Phys. Rev. Lett.*, 77:3865–3868, 1996.

[125] F. Weigend and R. Ahlrichs. Balanced Basis Sets of Split Valence, Triple Zeta Valence and Quadruple Zeta Valence Quality for H to Rn: Design and Assessment of Accuracy. *Phys. Chem. Chem. Phys.*, 7(18):3297–3305, 2005.

[126] D. Rappoport and F. Furche. Property-Optimized Gaussian Basis Sets for Molecular Response Calculations. *J. Chem. Phys.*, 133(13):134105, 2010.

[127] D. Feller. The Role of Databases in Support of Computational Chemistry Calculations. *J. Comput. Chem.*, 17(13):1571–1586, 1996.

[128] K. L. Schuchardt, B. T. Didier, T. Elsethagen, L. Sun, V. Gurumoorthi, J. Chase, J. Li, and T. L. Windus. Basis Set Exchange: A Community Database for Computational Sciences. *J. Chem. Inf. Model.*, 47(3):1045–1052, 2007.

[129] D. B. Lingerfelt, S. A. Fischer, J. W. May, and X. Li. Dynamical Investigations of Inhomogenous Vibrational Broadening in Diluted Magnetic Semiconductor Nanocrystals. *J. Phys. Chem. C*, 118:3266–3273, 2014.

[130] D. B. Lingerfelt, D. B. Williams-Young, A. Petrone, and X. Li. Direct Ab Initio (Meta-)Surface-Hopping Dynamics. *J. Chem. Theory Comput.*, 12:935–945, 2016.

[131] J.-W. Song, M. A. Watson, A. Nakata, and K. Hirao. Core-Excitation Energy Calculations With a Long-Range Corrected Hybrid Exchange-Correlation Functional Including a Short-Range Gaussian Attenuation (LCgau-BOP). *J. Chem. Phys.*, 129(18):184113, 2008.

[132] R. Leapman and L. Grunes. Anomalous L_3/L_2 White-Line Ratios in the $3d$ Transition Metals. *Phys. Rev. Lett.*, 45(5):397, 1980.

[133] B. Thole and G. van der Laan. Branching Ratio in X-ray Absorption Spectroscopy. *Phys. Rev. B*, 38(5):3158, 1988.

[134] M. Pederson, A. Liu, T. Baruah, E. Kurmaev, A. Moewes, S. Chiuzbăian, M. Neumann, C. Kmety, K. Stevenson, and D. Ederer. Electronic Structure of the Molecule-Based Magnet $Mn[N(CN)_2]_2$ from Theory and Experiment. *Phys. Rev. B*, 66(1):014446, 2002.

[135] O. Bunău and Y. Joly. Full Potential X-ray Absorption Calculations Using Time Dependent Density Functional Theory. *J. Phys.–Condens. Mat.*, 24(21):215502, 2012.

[136] H. Ikeno, F. M. F. d. Groot, and I. Tanaka. *Ab-initio* CI Calculations for 3*d* Transition Metal $L_{2,3}$ X-ray Absorption Spectra of $TiCl_4$ and $VOCl_3$. *J. Phys. Conf. Ser.*, 190:012005, 2009.

[137] G. Capano, T. J. Penfold, N. A. Besley, C. J. Milne, M. Reinhard, H. Rittmann-Frank, P. Glatzel, R. Abela, U. Rothlisberger, M. Chergui, and I. Tavernelli. The Role of Hartree–Fock Exchange in the Simulation of X-ray Absorption Spectra: A Study of Photoexcited $[Fe(bpy)_3]^{2+}$. *Chem. Phys. Lett.*, 580:179–184, 2013.

[138] E. Vecharynski, C. Yang, and F. Xue. Generalized Preconditioned Locally Harmonic Residual Method for Non-Hermitian Eigenproblems. *SIAM J. Sci. Comp.*, 38(1):A500–A527, 2016.

[139] E. Runge and E. K. U. Gross. Density-Functional Theory for Time-Dependent Systems. *Phys. Rev. Lett.*, 52(12):9971–1000, 1984.

[140] M. E. Casida. Time-Dependent Density-Functional Response Theory for Molecules. In *Recent Advances in Density Functional Methods (Part I)*, pages 155–193. World Scientific, 1995.

[141] M. Petersilka, U. J. Gossmann, and E. K. U. Gross. Excitation Energies From Time-Dependent Density-Functional Theory. *Phys. Rev. Lett.*, 76:1212–1215, 1996.

[142] E. R. Davidson. The Iterative Calculation of a Few of the Lowest Eigenvalues and Corresponding Eigenvectors of Large Real-Symmetric Matrices. *J. Chem. Phys.*, 17(1):87–94, 1975.

[143] H. Weiss, R. Ahlrichs, and M. Häser. A Direct Algorithm for Self-Consistent-Field Linear Response Theory and Application to C_{60}: Excitation Energies, Oscillator Strengths, and Frequency-Dependent Polarizabilities. *J. Chem. Phys.*, 99(2):1262–1270, 1993.

[144] S. Rettrup. An Iterative Method for Calculating Several of the Extreme Eigensolutions of Large Real Non-Symmetric Matrices. *J. Chem. Phys.*, 45(1):100–107, 1982.

[145] S. Coriani, S. Høst, B. Jansík, L. Thøgersen, J. Olsen, P. Jørgensen, S. Reine, F. Pawłowski, T. Helgaker, and P. Sałek. Linear-Scaling Implementation of Molecular Response Theory in Self-Consistent Field Electronic-Structure Theory. *J. Chem. Phys.*, 126(15):154108, 2007.

[146] R. E. Stratmann, G. E. Scuseria, and M. J. Frisch. An Efficient Implementation of Time-Dependent Density-Functional Theory for the Calculation of Excitation Energies of Large Molecules. *J. Chem. Phys.*, 109(19):8218–8224, 1998.

[147] F. Furche. On the Density Matrix Based Approach to Time-Dependent Density Functional Response Theory. *J. Chem. Phys.*, 114:5982–5992, 2001.

[148] A. Dreuw and M. Head-Gordon. Single-Reference Ab Initio Methods for the Calculation of Excited States of Large Molecules. *Chem. Rev.*, 105:4009–4037, 2005.

[149] Y. Zhang, J. D. Biggs, D. Healion, N. Govind, and S. Mukamel. Core and Valence Excitations in Resonant X-ray Spectroscopy Using Restricted Excitation Window Time-dependent Density Functional Theory. *J. Chem. Phys.*, 137(19):194306, 2012.

[150] J. Kauczor, P. Norman, O. Christiansen, and S. Coriani. Communication: A Reduced-Space Algorithm for the Solution of the Complex Linear Response Equations Used in Coupled Cluster Damped Response Theory. *J. Chem. Phys.*, page 211102, 2013.

[151] T. Fahleson, H. Ågren, and P. Norman. A Polarization Propagator for Nonlinear X-ray Spectroscopies. *J. Phys. Chem. Lett.*, 7(11):1991–1995, 2016.

[152] S. Coriani, T. Fransson, O. Christiansen, and P. Norman. Asymmetric-Lanczos-Chain-Driven Implementation of Electronic Resonance Convergent Coupled-Cluster Linear Response Theory. *J. Chem. Theory Comput.*, 8(5):1616–1628, 2012.

[153] M. Linares, S. Stafström, Z. Rinkevicius, H. Ågren, and P. Norman. Complex Polarization Propagator Approach in the Restricted Open-Shell, Self-Consistent Field Approximation: The Near K-Edge X-ray Absorption Fine Structure Spectra of Allyl and Copper Phthalocyanine. *J. Phys. Chem. B*, 115(18):5096–5102, 2010.

[154] U. Ekström, P. Norman, V. Carravetta, and H. Ågren. Polarization Propagator for X-ray Spectra. *Phys. Rev. Lett.*, 97(14):143001, 2006.

[155] T. Fransson, D. Burdakova, and P. Norman. K-and L-edge X-ray Absorption Spectrum Calculations of Closed-Shell Carbon, Silicon, Germanium, and Sulfur Compounds Using Damped Four-Component Density Functional Response Theory. *Phys. Chem. Chem. Phys.*, 18(19):13591–13603, 2016.

[156] J. Brabec, L. Lin, M. Shao, N. Govind, C. Yang, Y. Saad, and E. G. Ng. Efficient Algorithms for Estimating the Absorption Spectrum Within Linear Response TDDFT. *J. Chem. Theory Comput.*, 11(11):5197–5208, 2015.

[157] R. Bauernschmitt and R. Ahlrichs. Treatment of Electronic Excitations Within the Adiabatic Approximation of Time Dependent Density Functional Theory. *Chem. Phys. Lett.*, 256(4-5):454–464, 1996.

[158] D. Zuev, E. Vecharynski, C. Yang, N. Orms, and A. I. Krylov. New Algorithms for Iterative Matrix-Free Eigensolvers in Quantum Chemistry. *J. Comput. Chem.*, 36(5):273–284, 2015.

[159] E. Vecharynski, J. Brabec, M. Shao, N. Govind, and C. Yang. Efficient Block Preconditioned Eigensolvers for Linear Response Time-Dependent Density Functional Theory. *Comp. Phys. Comm.*, 221:42 – 52, 2017.

[160] J. Olsen, H. J. A. Jensen, and P. Jørgensen. Solution of the Large Matrix Equations Which Occur in Response Theory. *J. Chem. Phys.*, 74(2):265–282, 1988.

[161] J. Kauczor, P. Jørgensen, and P. Norman. On the Efficiency of Algorithms for Solving Hartree–Fock and Kohn–Sham Response Equations. *J. Chem. Theory Comput.*, 7(6):1610–1630, 2011.

[162] X. Li and M. J. Frisch. Energy-Represented Direct Inversion in the Iterative Subspace Within a Hybrid Geometry Optimization Method. *J. Chem. Theory Comput.*, 2(3):835–839, 2006.

[163] A. V. Knyazev. Toward the Optimal Preconditioned Eigensolver: Locally Optimal Block Preconditioned Conjugate Gradient Method. *SIAM J. Sci. Comp.*, 23(2):517–541, 2001.

[164] R. Krishnan, J. S. Binkley, R. Seeger, and J. A. Pople. Self-Consistent Molecular Orbital Methods. XX. A Basis Set for Correlated Wave Functions. *J. Chem. Phys.*, 72(1):650–654, 1980.

[165] T. Clark, J. Chandrasekhar, G. W. Spitznagel, and P. V. R. Schleyer. Efficient Diffuse Function-Augmented Basis Sets for Anion Calculations. III. The 3-21+ G Basis Set for First-Row Elements, Li–F. *J. Comput. Chem.*, 4(3):294–301, 1983.

[166] P. Hariharan and J. Pople. The Influence of Polarization Functions on Molecular Orbital Hydrogenation Energies. *Theor. Chem. Acc.*, 28:213–222, 1973.

[167] M. M. Francl, W. J. Pietro, W. J. Hehre, J. S. Binkley, M. S. Gordon, D. J. DeFrees, and J. A. Pople. Self-Consistent Molecular Orbital Methods. XXIII. A Polarization-Type Basis Set for Second-Row Elements. *J. Chem. Phys.*, 77(7):3654–3665, 1982.

[168] A. Petrone, J. J. Goings, and X. Li. Quantum Confinement Effects on Optical Transitions in Nanodiamonds Containing Nitrogen Vacancies. *Phys. Rev. B*, 94:165402, 2016.

[169] W. Liu. *Handbook of Relativistic Quantum Chemistry*. Springer-Verlag Berlin Heidelberg, 2017.

[170] M. Reiher and A. Wolf. Exact Decoupling of the Dirac Hamiltonian. I. General Theory. *J. Chem. Phys.*, 121(5):2037–2047, 2004.

[171] M. Reiher and A. Wolf. Exact Decoupling of the Dirac Hamiltonian. II. The Generalized Douglas-Kroll-Hess Transformation Up to Arbitrary Order. *J. Chem. Phys.*, 121:10945, 2004.

[172] J. E. Peralta and G. E. Scuseria. Relativistic All-Electron Two-Component Self-Consistent Density Functional Calculations Including One-Electron Scalar and Spin-Orbit Effects. *J. Chem. Phys.*, 120:5875, 2004.

[173] M. Filatov, W. Zou, and D. Cremer. Spin-Orbit Coupling Calculations with the Two-Component Normalized Elimination of the Small Component Method. *J. Chem. Phys.*, 139:014106, 2013.

[174] D.-e. Jiang, M. Kühn, Q. Tang, and F. Weigend. Superatomic Orbitals Under Spin–Orbit Coupling. *J. Phys. Chem. Lett.*, 5(19):3286–3289, 2014.

[175] J. J. Goings, F. Ding, E. R. Davidson, and X. Li. Approximate Singly Excited States from a Two-Component Hartree Fock Reference. *J. Chem. Phys.*, 143:144106, 2015.

[176] W. Liu and Y. Xiao. Relativistic Time-Dependent Density Functional Theories. *Chem. Soc. Rev.*, 47:4481–4509, 2018.

[177] R. L. Martin. Natural Transition Orbitals. *J. Chem. Phys.*, 118(11):4775–4777, 2003.

[178] L. M. Thompson, H. Harb, and H. P. Hratchian. Natural Ionization Orbitals for Interpreting Electron Detachment Processes. *J. Chem. Phys.*, 144(20):204117, 2016.

[179] K. Krause and W. Klopper. Description of Spin-Orbit Coupling in Excited States with Two-Component Methods Based on Approximate Coupled-Cluster Theory. *J. Chem. Phys.*, 142(10):104109, 2015.

[180] C. Holzer and W. Klopper. Ionized, Electron-Attached, and Excited States of Molecular Systems with Spin-Orbit Coupling: Two-Component GW and Bethe-Salpeter Implementations. *J. Chem. Phys.*, 150(20):204116, 2019.

[181] J. M. Kasper, D. B. Williams-Young, E. Vecharynski, C. Yang, and X. Li. A Well-Tempered Hybrid Method for Solving Challenging Time-Dependent Density Functional Theory (TDDFT) Systems. *J. Chem. Theory Comput.*, 14(4):2034–2041, 2018.

[182] A. Amos and G. Hall. Single Determinant Wave Functions. *Proc. R. Soc. London, Ser. A*, 263(1315):483–493, 1961.

[183] A. Petrone, D. B. Williams-Young, S. Sun, T. F. Stetina, and X. Li. An Efficient Implementation of Two-Component Relativistic Density Functional Theory with Torque-Free Auxiliary Variables. *Euro. Phys. J. B*, 91(7):169, 2018.

[184] T. F. Stetina, J. M. Kasper, and X. Li. Modeling $L_{2,3}$-Edge X-ray Absorption Spectroscopy with Linear Response Exact Two-Component Relativistic Time-Dependent Density Functional Theory. *J. Chem. Phys.*, 150:234103, 2019.

[185] D. W. Small, E. J. Sundstrom, and M. Head-Gordon. Restricted Hartree Fock using Complex-Valued Orbitals: A Long-Known but Neglected Tool in Electronic Structure Theory. *J. Chem. Phys.*, 142(2):024104, 2015.

[186] R. Al-Saadon, T. Shiozaki, and G. Knizia. Visualizing Complex-Valued Molecular Orbitals. *J. Phys. Chem. A*, 123(14):3223–3228, 2019.

[187] D. A. Pantazis, X.-Y. Chen, C. R. Landis, and F. Neese. All-Electron Scalar Relativistic Basis Sets for Third-Row Transition Metal Rtoms. *J. Chem. Theory Comput.*, 4(6):908–919, 2008.

[188] B. P. Pritchard, D. Altarawy, B. Didier, T. D. Gibson, and T. L. Windus. New Basis Set Exchange: An Open, Up-to-Date Resource for the Molecular Sciences Community. *J. Chem. Inf. Model.*, 59(11):4814–4820, 2019.

[189] E. B. Saloman. Wavelengths, Energy Level Classifications, and Energy Levels for the Spectrum of Neutral Mercury. *J. Phys. Chem. Ref. Data*, 35(4):1519–1548, 2006.

[190] J. M. Kasper, P. J. Lestrange, T. F. Stetina, and X. Li. Modeling $L_{2,3}$-Edge X-ray Absorption Spectroscopy with Real-Time Exact Two-Component Relativistic Time-Dependent Density Functional Theory. *J. Chem. Theory Comput.*, 14(4):1998–2006, 2018.

[191] P. Stephens, F. Devlin, C. Chabalowski, and M. Frisch. Ab Initio Calculation of Vibrational Absorption and Circular Dichroism Spectra Using SCF, MP2, and Density Functional Theory Force Fields. *J. Phys. Chem.*, 98:11623, 1994.

[192] R. Beaulac, S. T. Ochsenbein, and D. R. Gamelin. Colloidal Transition-Metal-Doped Quantum Dots. In *Nanocrystal Quantum Dots*, pages 397–454. CRC Press, 2017.

[193] G. Armelles, A. Cebollada, A. García-Martín, and M. U. González. Magnetoplasmonics: Combining Magnetic and Plasmonic Functionalities. *Adv. Opt. Mater.*, 1(1):10–35, 2013.

[194] M. A. Becker, R. Vaxenburg, G. Nedelcu, P. C. Sercel, A. Shabaev, M. J. Mehl, J. G. Michopoulos, S. G. Lambrakos, N. Bernstein, J. L. Lyons, T. Stöferle, R. F. Marht, M. V. Kovalenko, D. J. Norris, G. Rainó, and A. L. Efros. Bright Triplet Excitons in Caesium Lead Halide Perovskites. *Nature*, 553(7687):189, 2018.

[195] L.-W. Wang and J. Li. First-Principles Thousand-Atom Quantum Dot Calculations. *Phys. Rev. B*, 69(15):153302, 2004.

[196] E. Badaeva, J. W. May, J. Ma, D. R. Gamelin, and X. Li. Characterization of Excited-State Magnetic Exchange in Mn^{2+}-Doped ZnO Quantum Dots Using Time-Dependent Density Functional Theory. *J. Phys. Chem. C*, 115(43):20986–20991, 2011.

[197] J. J. Goings, A. M. Schimpf, J. W. May, R. W. Johns, D. R. Gamelin, and X. Li. Theoretical Characterization of Conduction-Band Electrons in Photodoped and Aluminum-Doped Zinc Oxide (AZO) Quantum Dots. *J. Phys. Chem. C*, 118(46):26584–26590, 2014.

[198] H. D. Nelson, X. Li, and D. R. Gamelin. Computational Studies of the Electronic Structures of Copper-Doped CdSe Nanocrystals: Oxidation States, Jahn–Teller Distortions, Vibronic Bandshapes, and Singlet–Triplet Splittings. *J. Phys. Chem. C*, 120(10):5714–5723, 2016.

[199] H. Liu, C. K. Brozek, S. Sun, D. B. Lingerfelt, D. R. Gamelin, and X. Li. A Hybrid Quantum-Classical Model of Electrostatics in Multiply Charged Quantum Dots. *J. Phys. Chem. C*, 121(46):26086–26095, 2017.

[200] M. Walter, J. Akola, O. Lopez-Acevedo, P. D. Jadzinsky, G. Calero, C. J. Ackerson, R. L. Whetten, H. Grönbeck, and H. Häkkinen. A Unified View of Ligand-protected Gold Clusters as Superatom Complexes. *Proc. Natl. Acad. Sci. U.S.A.*, 105(27):9157–9162, 2008.

[201] J. Akola, M. Walter, R. L. Whetten, H. Häkkinen, and H. Grönbeck. On the Structure of Thiolate-Protected Au_{25}. *J. Am. Chem. Soc.*, 130(12):3756–3757, 2008.

[202] K. Nash, P. Calcott, L. Canham, and R. Needs. Spin-Orbit Interaction, Triplet Lifetime, and Fine-Structure Splitting of Excitons in Highly Porous Silicon. *Phys. Rev. B*, 51(24):17698, 1995.

[203] J. Fu and M. Wu. Spin-Orbit Coupling in Bulk ZnO and GaN. *J. Appl. Phys.*, 104(9):093712, 2008.

[204] P. C. Sercel and A. L. Efros. Band-Edge Exciton in CdSe and Other II–VI and III–V Compound Semiconductor Nanocrystals- Revisited. *Nano Lett.*, 18(7):4061–4068, 2018.

[205] A. Manchon, H. C. Koo, J. Nitta, S. Frolov, and R. Duine. New Perspectives for Rashba Spin-Orbit Coupling. *Nat. Mater.*, 14(9):871, 2015.

[206] F. S. Ham. Effect of Linear Jahn-Teller Coupling on Paramagnetic Resonance in a E_2 State. *Phys. Rev.*, 166(2):307, 1968.

[207] L. E. Brus. A Simple Model for the Ionization Potential, Electron Affinity, and Aqueous Redox Potentials of Small Semiconductor Crystallites. *J. Chem. Phys.*, 79(11):5566–5571, 1983.

[208] L. E. Brus. Electron Electron and Elctron-Hole Interactions in Small Semiconductor Crystallites - the Size Dependence of the Lowest Excited Electronic States. *J. Chem. Phys.*, 80(9):4403–4409, 1984.

[209] G.-H. Chen and M. Raikh. Exchange-Induced Enhancement of Spin-Orbit Coupling in Two-Dimensional Electronic Systems. *Phys. Rev. B*, 60(7):4826, 1999.

[210] R. Li, Z.-H. Liu, Y. Wu, and C. Liu. The Impacts of the Quantum-Dot Confining Potential on the Spin-Orbit Effect. *SIAM Rev.*, 8(1):7400, 2018.

[211] Z. Li, Y. Xiao, and W. Liu. On the Spin Separation of Algebraic Two-Component Relativistic Hamiltonians. *J. Chem. Phys.*, 137:154114, 2012.

[212] E. Badaeva, Y. Feng, D. R. Gamelin, and X. Li. Investigation of Pure and Co^{2+}-Doped ZnO Quantum Dot Electronic Structures Using the Density Functional Theory: Choosing the Right Functional. *New J. Phys.*, 10:055013, 2008.

[213] E. Badaeva, C. M. Isborn, Y. Feng, S. T. Ochsenbein, D. R. Gamelin, and X. Li. Theoretical Characterization of Electronic Transitions in Co^{2+}- and Mn^{2+}-Doped ZnO Nanocrystals. *J. Phys. Chem. C*, 113(20):8710–8717, 2009.

[214] Y. Feng, E. Badaeva, D. R. Gamelin, and X. Li. Excited-State Double Exchange in

Manganese-Doped ZnO Quantum Dots: A Time-Dependent Density-Functional Study. *J. Phys. Chem. Lett.*, 1(13):1927–1931, 2010.

[215] J. W. May, J. Ma, E. Badaeva, and X. Li. Effect of Excited-State Structural Relaxation on Midgap Excitations in Co^{2+}-Doped ZnO Quantum Dots. *J. Phys. Chem. C*, 118(24):13152–13156, 2014.

[216] S. A. Fischer, D. B. Lingerfelt, J. W. May, and X. Li. Non-Adiabatic Molecular Dynamics Investigation of Photoionization State Formation and Lifetime in Mn^{2+}-Doped ZnO Quantum Dots. *Phys. Chem. Chem. Phys.*, 16:17507–17514, 2014.

[217] F. Kyrychenko and J. Kossut. Diluted Magnetic Semiconductor Quantum Dots: An Extreme Sensitivity of the Hole Zeeman Splitting on the Aspect Ratio of the Confining Potential. *Phys. Rev. B*, 70(20):205317, 2004.

[218] J.-W. Wang and S.-S. Li. Excitonic Bright-to-Dark Transition Induced by Spin-Orbit Coupling. *Appl. Phys. Lett.*, 92(1):012106, 2008.

[219] N. Ashkenov, B. Mbenkum, C. Bundesmann, V. Riede, M. Lorenz, D. Spemann, E. Kaidashev, A. Kasic, M. Schubert, M. Grundmann, G. Wagner, H. Neumann, V. Darakchieva, H. Arwin, and B. Monemar. Infrared Dielectric Functions and Phonon Modes of High-Quality ZnO Films. *J. Appl. Phys.*, 93(1):126–133, 2003.

[220] J. I. Pankove. *Optical Processes in Semiconductors*. Dover, 1975.

[221] L. Lew Yan Voon, R. Melnik, B. Lassen, and M. Willatzen. Influence of Aspect Ratio on the Lowest States of Quantum Rods. *Nano Lett.*, 4(2):289–292, 2004.

[222] M. Kuno, J.-K. Lee, B. O. Dabbousi, F. V. Mikulec, and M. G. Bawendi. The Band Edge Luminescence of Surface Modified CdSe Nanocrystallites: Probing the Luminescing State. *J. Chem. Phys.*, 106(23):9869–9882, 1997.

Appendix A

RELATIVITY AND THE DIRAC EQUATION

Both quantum mechanics and the theory of special relativity were developed in the early twentieth century. However, the Schrödinger equation, the fundamental equation of what is now known as non-relativistic quantum mechanics, did not obey special relativity. The need to reconcile these two topics of physics led to the development of relativistic quantum mechanics and quantum field theory. For the purposes of this work the focus will be on the Dirac equation, which is the relativistic analogue of the Schrödinger equation for electrons. What follows is a derivation of the four-component to two-component transformation of the Dirac quation and the exact two-component (X2C) method.

A.1 Dirac Equation

Our point of departure is the four-component Dirac equation for a free-electron:

$$i\hbar\frac{\partial}{\partial t}\Psi = \left[c\vec{\alpha}\cdot\vec{p} + \beta mc^2\right]\Psi = \hat{h}^D\Psi \tag{A.1}$$

where the matrices $\vec{\alpha}$ and β are defined as:

$$\alpha_{w=x,y,z} = \begin{pmatrix} 0 & \sigma_w \\ -\sigma_w & 0 \end{pmatrix} \tag{A.2}$$

and

$$\beta = \begin{pmatrix} 1 & 0 \\ 0 & -1 \end{pmatrix} \tag{A.3}$$

The Pauli spin matrices are given as

$$\sigma_x = \begin{pmatrix} 0 & 1 \\ 1 & 0 \end{pmatrix}; \sigma_y = \begin{pmatrix} 0 & -i \\ i & 0 \end{pmatrix}; \sigma_z = \begin{pmatrix} 1 & 0 \\ 0 & -1 \end{pmatrix} \tag{A.4}$$

Due to the block diagonal structure of $\vec{\alpha}$ and β it is customary to split Ψ into "large" and "small" components denoted ψ^L and ψ^S, respectively.

$$\left[\begin{pmatrix} 0 & c\vec{\sigma}\cdot\vec{p} \\ c\vec{\sigma}\cdot\vec{p} & 0 \end{pmatrix} + \begin{pmatrix} mc^2 & 0 \\ 0 & -mc^2 \end{pmatrix}\right]\begin{pmatrix} \psi^L \\ \psi^S \end{pmatrix} = E\begin{pmatrix} \psi^L \\ \psi^S \end{pmatrix} \tag{A.5}$$

Additionally we shift the energy scale by subtracting the rest energy of the electron (mc^2) so that our energies will match the non-relativistic Schrödinger equation in the appropriate limit. In the presence of an external potential V that is assumed to be diagonal (such as the nuclear potential) this yields

$$\left[\begin{pmatrix} 0 & c\vec{\sigma}\cdot\vec{p} \\ c\vec{\sigma}\cdot\vec{p} & 0 \end{pmatrix} + \begin{pmatrix} V & 0 \\ 0 & V-2mc^2 \end{pmatrix}\right]\begin{pmatrix} \psi^L \\ \psi^S \end{pmatrix} = E\begin{pmatrix} \psi^L \\ \psi^S \end{pmatrix} \tag{A.6}$$

A.1.1 X-Operator

To reduce the cost of the calculation, a relationship between the small and large components can be established. Our goal here is to fold the effect of the small component into the large component since it is the large component that contributes significantly to electronic solutions. To start, we examine the relation

$$\psi^S = X\psi^L \tag{A.7}$$

where X is an operator to be determined. From the Eq. (A.6) we find that

$$X = \frac{c\vec{\sigma}\cdot\vec{p}}{\epsilon - V + 2mc^2} \tag{A.8}$$

Grouping the term $(\epsilon - V)$, we see that when $(\epsilon - V) \ll 2mc^2$ (the non-relativistic limit when kinetic energy is small compared to rest energy) then the expression simplifies to

$$X \approx \frac{c\vec{\sigma}\cdot\vec{p}}{2mc^2} = \frac{\vec{\sigma}\cdot\vec{p}}{2mc} \tag{A.9}$$

The condition

$$\psi^S = \frac{\vec{\sigma}\cdot\vec{p}}{2mc}\psi^L \tag{A.10}$$

is the well-known *kinetic balance* condition, which ensures that the solutions agree with the non-relativistic limit. In particular,

$$\lim_{c\to\infty} \frac{\vec{\sigma}\cdot\vec{p}}{2mc}\psi^L = 0 = \psi^S \tag{A.11}$$

which is to say that the positronic component is zero outside the framework of special relativity.

A.1.2 Unitary Transformation of the Dirac Hamiltonian

With this in mind, consider the possiblity of block-diagonalizing the four-component Fock matrix f with some unitary transformation $\mathcal{U}$ so that

$$f_{bd} = \mathcal{U} f \mathcal{U}^\dagger = \begin{pmatrix} f_+ & 0 \\ 0 & f_- \end{pmatrix} \tag{A.12}$$

In this case, we also use $\mathcal{U}$ to transform the two-spinor components according to

$$\tilde{\phi} = \mathcal{U}\phi = \begin{pmatrix} \tilde{\psi}^L \\ \tilde{\psi}^S \end{pmatrix} \tag{A.13}$$

As the transformation is unitary, all eigenvalues and eigenstates of the block-diagonalized matrix will match those of the original. In this way we may solve for just the electronic solutions given by the f_+ matrix. Writing the unitary transformation as

$$\mathcal{U} = \begin{pmatrix} \mathcal{U}^{LL} & \mathcal{U}^{LS} \\ \mathcal{U}^{SL} & \mathcal{U}^{SS} \end{pmatrix} \tag{A.14}$$

and using our condition that $\tilde{\psi}^S = 0$ we find that

$$\left[\mathcal{U}^{SL} + \mathcal{U}^{SS} X\right] \psi^L = 0 \tag{A.15}$$

using the 'X' operator from before. Enforcing the unitary condition that $\mathcal{U}\mathcal{U}^\dagger = 1$, the unitary matrix takes the form:

$$(1 + X^\dagger X)^{-1/2} \begin{pmatrix} 1 & X^\dagger \\ -X & 1 \end{pmatrix} \tag{A.16}$$

A.2 Modifed Dirac Equation and X2C

In practical calculations with a basis, we can enforce the kinetic balance condition by requiring $\phi_\mu^S \in \{(\vec{\sigma}\cdot\vec{p})\phi_\nu^L\}$. This restriction can be done via a unitary transformation $\mathcal{U}_{KB}$:

$$\mathcal{U}_{KB} = \begin{pmatrix} 1 & 0 \\ 0 & s \end{pmatrix} \tag{A.17}$$

where

$$s = \frac{(\vec{\sigma}\cdot\vec{p})}{p} \tag{A.18}$$

The kinetic-balanced Fock operator is given by

$$\tilde{f} = \mathcal{U}_{KB} f \mathcal{U}_{KB}^\dagger = \begin{pmatrix} V & c\boldsymbol{p} \\ c\boldsymbol{p} & \frac{(\sigma\cdot\boldsymbol{p})V(\sigma\cdot\boldsymbol{p}))}{\boldsymbol{p}^2} - 2mc^2 \end{pmatrix} \tag{A.19}$$

This form of the Dirac equation is known as the modified Dirac equation. The two-component spinors are formed by approriate linear combinations:

$$\psi_i^L(\boldsymbol{r}) = \sum_\mu c_{i\mu}^L \phi_\mu(\boldsymbol{r}) \psi_i^S(\boldsymbol{r}) = \sum_\mu c_{i\mu}^S \phi_\mu(\boldsymbol{r}) \tag{A.20}$$

and are solved in the matrix equation

$$\begin{pmatrix} \boldsymbol{V} & \boldsymbol{T} \\ \boldsymbol{T} & \frac{1}{4mc^2}\boldsymbol{W} - \boldsymbol{T} \end{pmatrix} \begin{pmatrix} c_+^L & c_-^L \\ c_+^S & c_-^S \end{pmatrix} = \begin{pmatrix} \boldsymbol{S} & 0 \\ 0 & \frac{1}{2mc^2}\boldsymbol{T} \end{pmatrix} \begin{pmatrix} c_+^L & c_-^L \\ c_+^S & c_-^S \end{pmatrix} \begin{pmatrix} \epsilon_+ & 0 \\ 0 & \epsilon_- \end{pmatrix} \tag{A.21}$$

where $\boldsymbol{W} = (\sigma\cdot\boldsymbol{p})V(\sigma\cdot\boldsymbol{p})$ and $\boldsymbol{S}$, $\boldsymbol{T}$, and $\boldsymbol{V}$ are the standard two-component matrices

$$\boldsymbol{S} = \begin{pmatrix} S & 0 \\ 0 & S \end{pmatrix}, \boldsymbol{T} = \begin{pmatrix} T & 0 \\ 0 & T \end{pmatrix}, \boldsymbol{V} = \begin{pmatrix} V & 0 \\ 0 & V \end{pmatrix}, \tag{A.22}$$

Now one can solve for the X operator as $X = c_+^S \cdot (c_+^L)^{-1}$. Although the full potential V including the effects of other electrons would be required to solve Eq. (A.21) for X exactly, the coupling is dominated by the one-electron nuclear attraction potential so that frequently this is ignored. In this case, the transformed Dirac equation is used as the new effective core Hamiltonian, including all single electron interactions. The two-electron interactions are treated the same as in the non-relativistic case.